Deep mantle structure and dynamics: constraints from observations and models

Frédéric Deschamps

Institute of Earth Sciences – Academia Sinica, Taipei

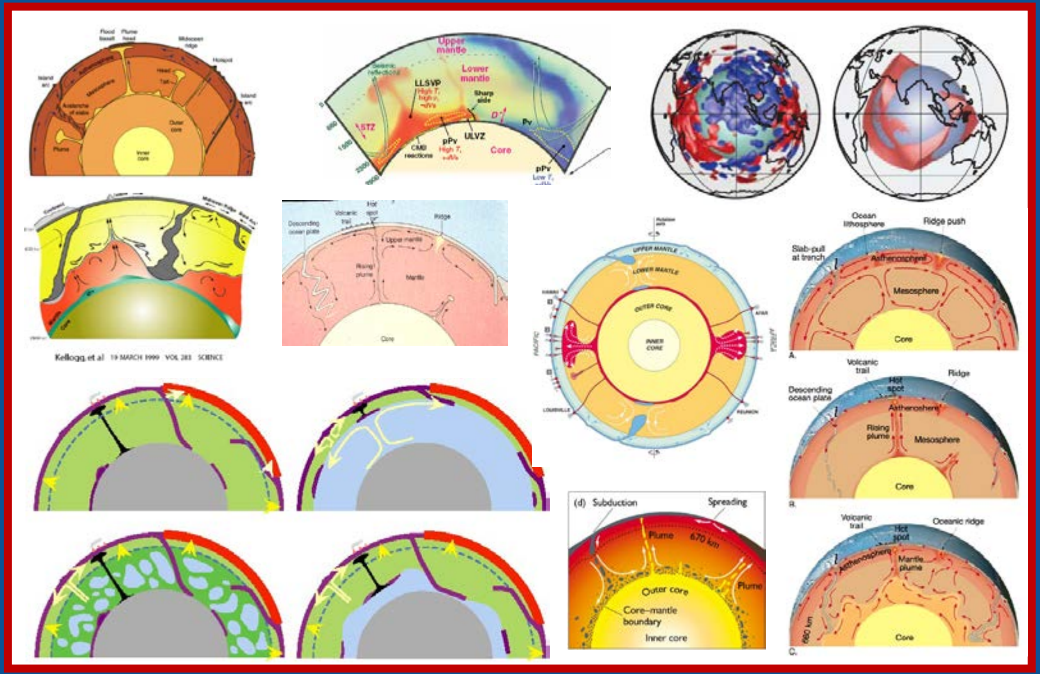

National Central University, November, 30th 2018

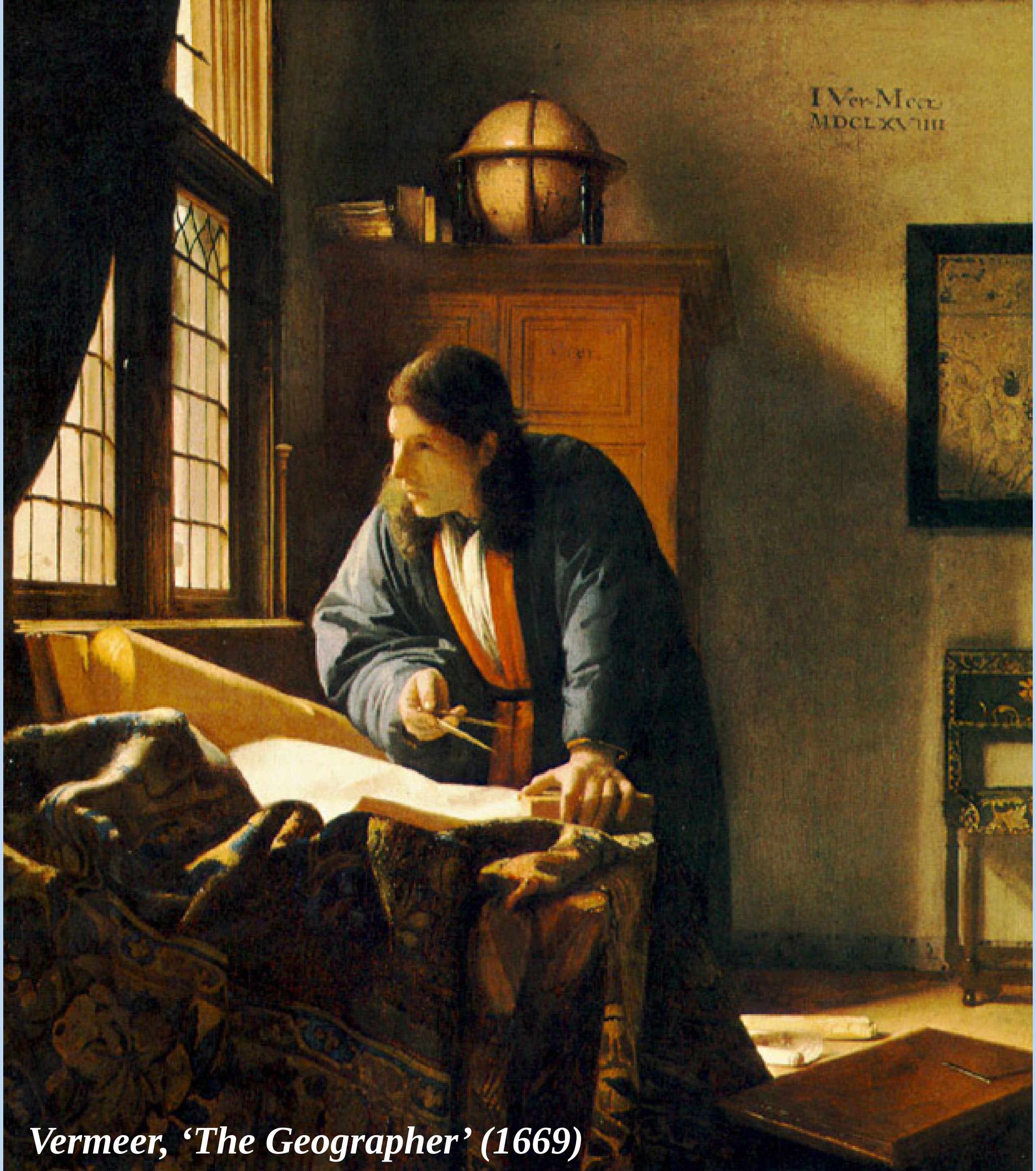

Vermeer, ‘The Geographer’ (1669)

3D maps of Earth's mantle: seismic tomography

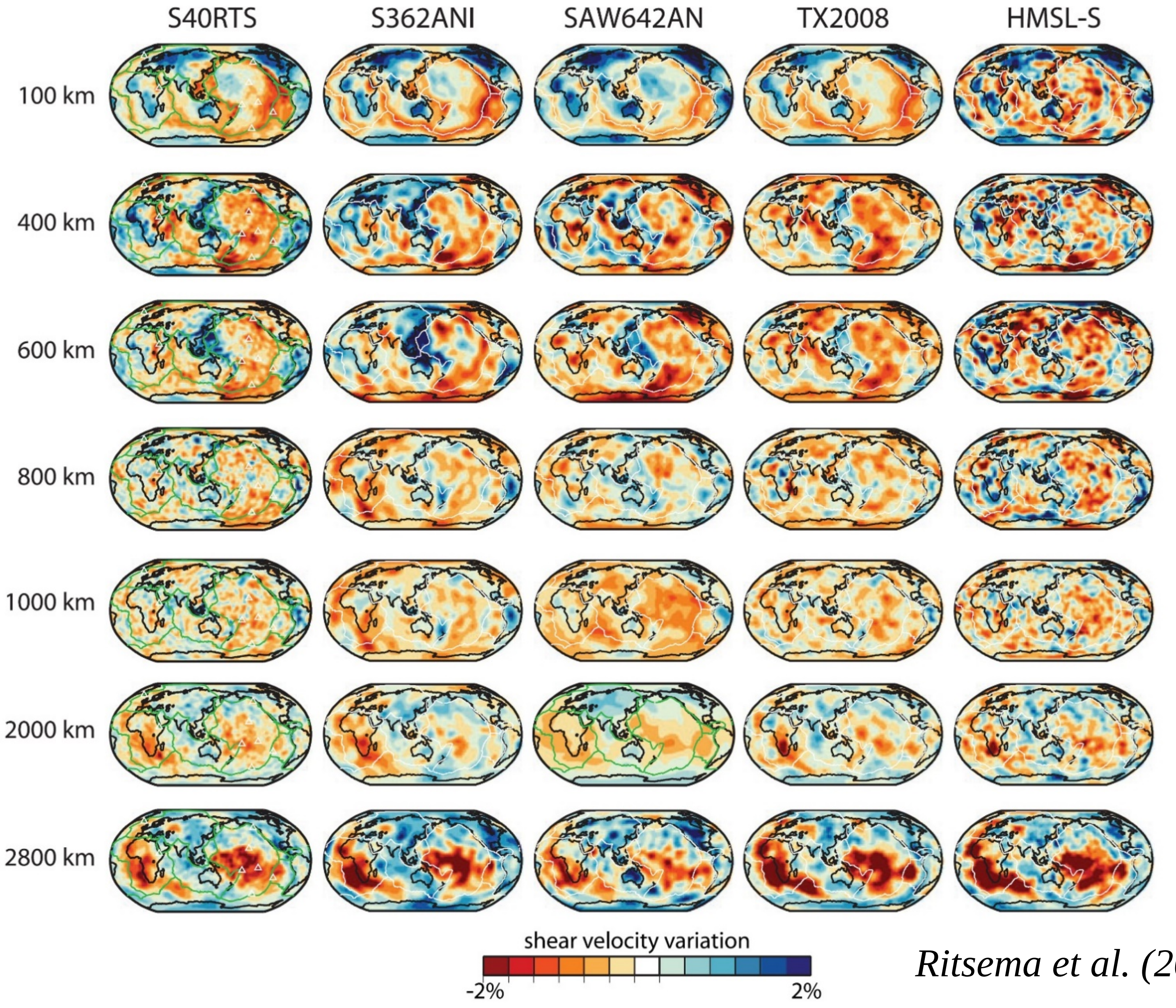

Ritsema et al. (2011)

Large low shear-wave velocity provinces (LLSVPs)

- Regions ~ 5000 km accross with strong decrease (up to 2-3 %) in shear-wave velocity. Extend from CMB up to 500-600 km and more in some models.

- Seen by all global seismic tomography models, with differences in amplitude, and detailed shape.

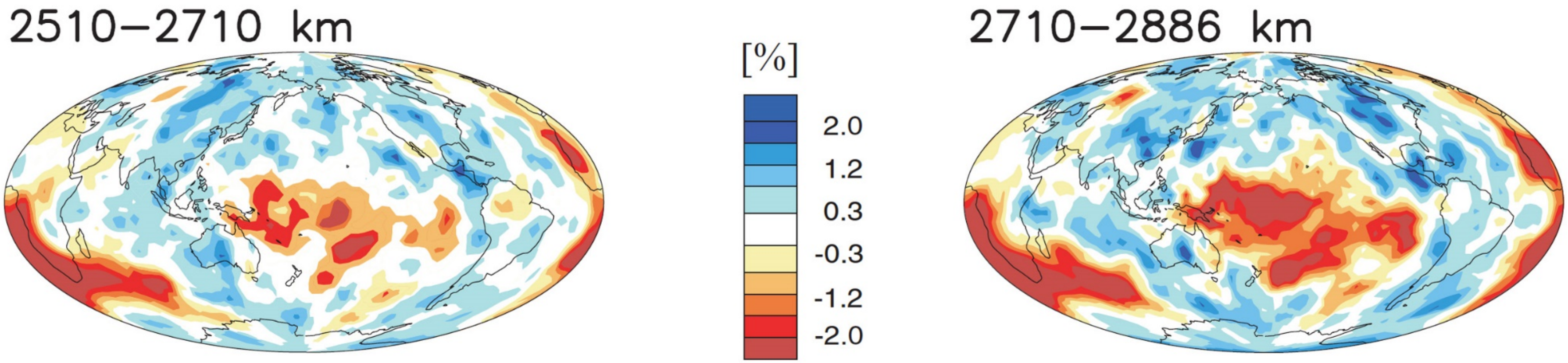

HMSL-S, *Houser et al. (2008)*

- Cluster analysis (Lekić et al., 2009; Garnero et al., 2016) of different tomographic models: LLSVPs are robust features, associated to physical features, not artifact or lack of resolution.

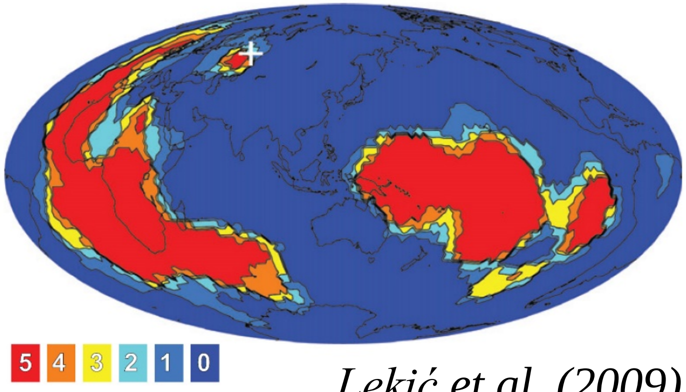

Lekić et al. (2009)

Deep mantle structure: purely thermal or thermo-chemical ?

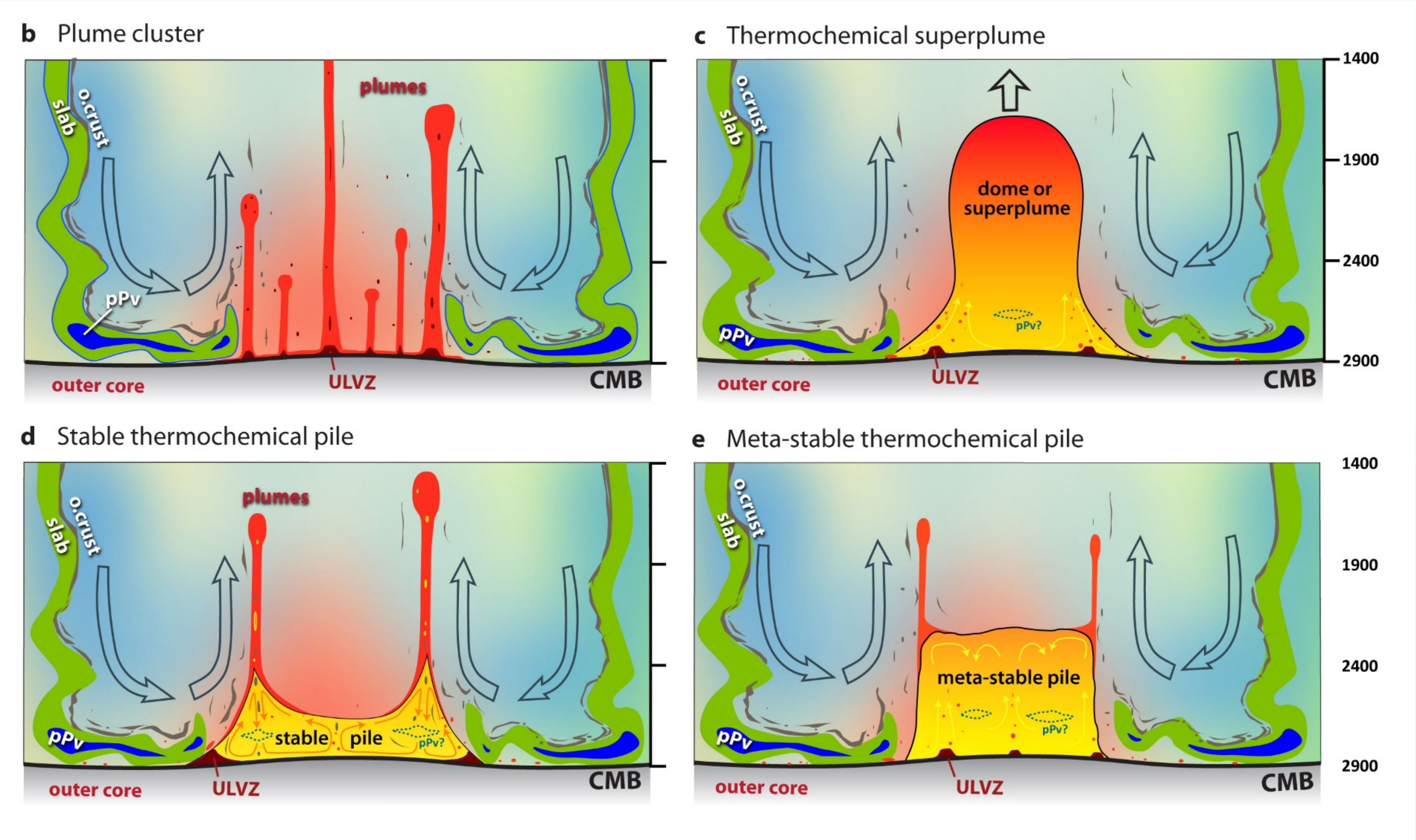

Garnero et al. (2016)

Maintaining thermo-chemical piles

- Key parameter: density contrast between dense and regular materials:

- Low contrast: oscillating domes (e.g., Davaille, 1999).

- Moderate contrast (~ 50-200 kg/m^3): stable and meta-stable piles (e.g., Tackley, 1998; McNamara and Zhong, 2004); induce strong thermal and chemical anomalies at the bottom of the shell.

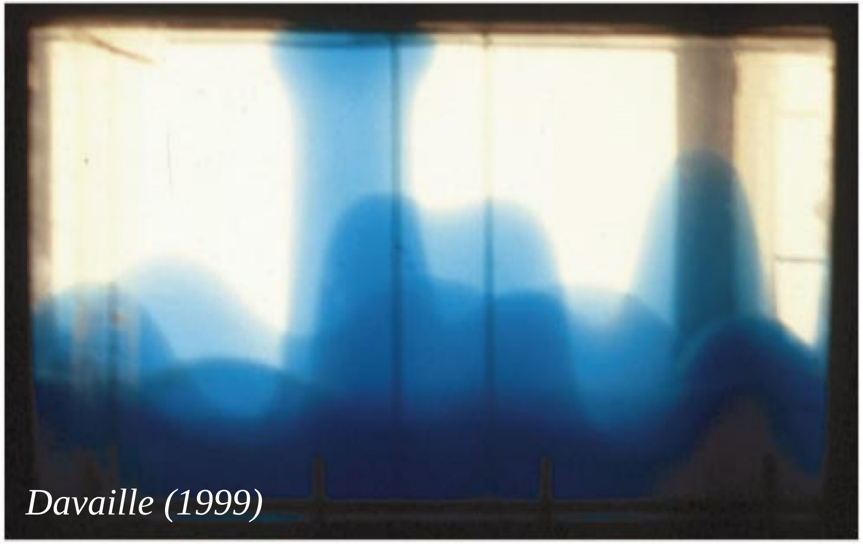

Davaille (1999)

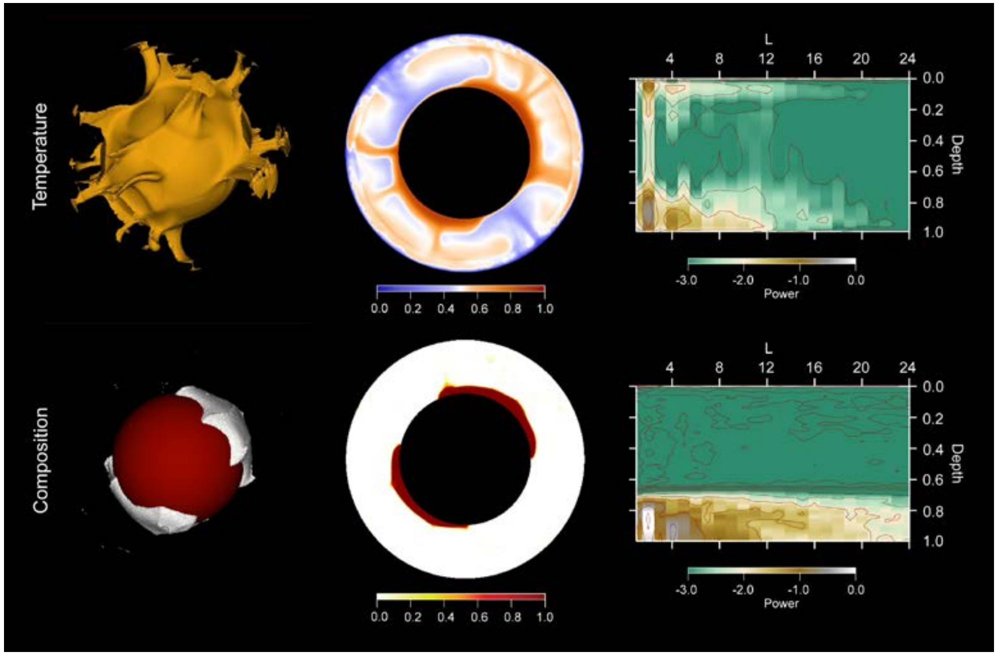

- Other important parameters:

- Bulk modulus: differences in bulk modulus increases buoyancy with depth and leads to meta-stable piles with sharp edges (Tan and Gurnis, 2007).

- Thermal viscosity contrast: large contrast limit thermal erosion (*e.g.*, Deschamps and Tackley, 2008).

From seismic velocities to thermo-chemical structure

- Seismic velocities depend on density and elastic moduli of mantle minerals

$$V_S = \sqrt{G/\rho} \qquad\qquad V_P = \sqrt{\left(K + \tfrac{4}{3}G\right)/\rho}$$

… which in turn depend on temperature, pressure and composition.

- Temperature anomalies: plumes, slabs, TBLs.

- Possible origin for compositional anomalies:
  - Bridgmanite vs ferro-periclase proportions.
  - Iron (FeO) fraction
  - Recycled oceanic crust (MORB) in the deep mantle
  - Topography of phase transition (*e.g.*, post-perovskite)
  - Melt (above CMB) and water (transition zone).

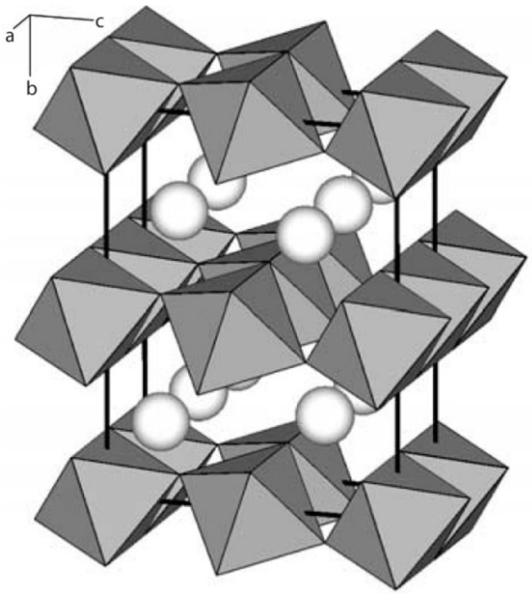

$CaTiO_3$ post-perovskite structure

- Density and thermo-elastic properties of mantle may be determined from data from mineral physics experiments (or calculations), and high-temperature high pressure extrapolations (*e.g.*, Birch-Murnaghan to the 3rd order).

Trade-off between temperature and composition

- Shear-wave velocity decreases with increasing temperature and iron content:

a negative 2% V_S-anomaly may be explain by purely thermal anomaly ~ 800 K, or thermal anomaly ~ 400 K plus enrichment in iron ~ 3%.

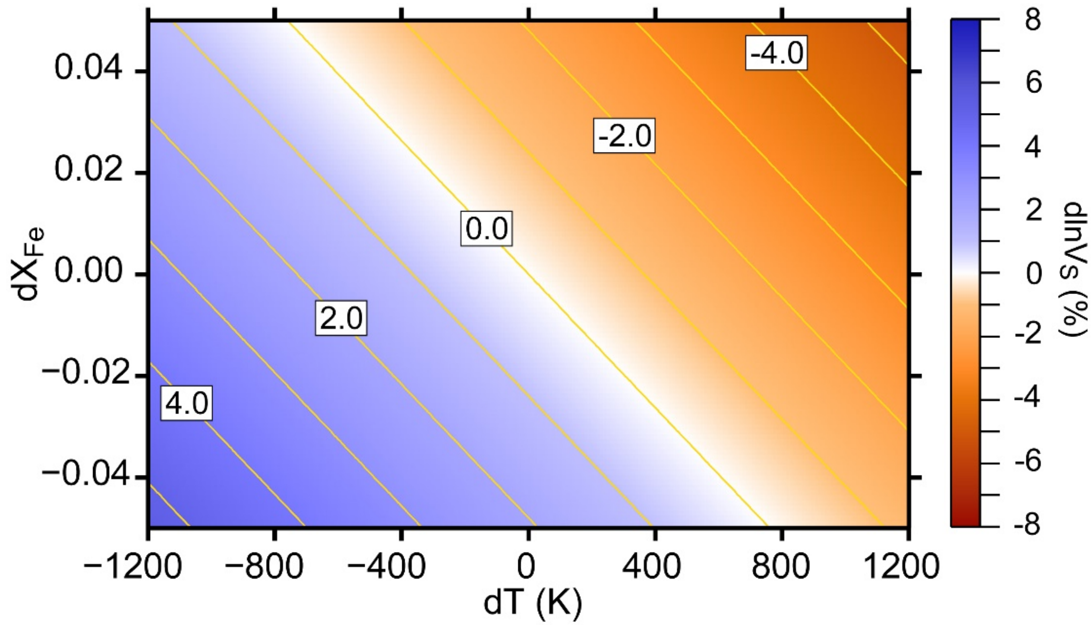

- Other possible compositional effects:

- Post-perovskite: faster than bridgmanite by ~ 2.0-4.0 %.
- MORB: V_S slightly increases with temperature, but depends on exact MORB composition.

- Need other constraints (Bulk-sound or compressional velocities, density).

Seismic sensitivities to temperature and composition

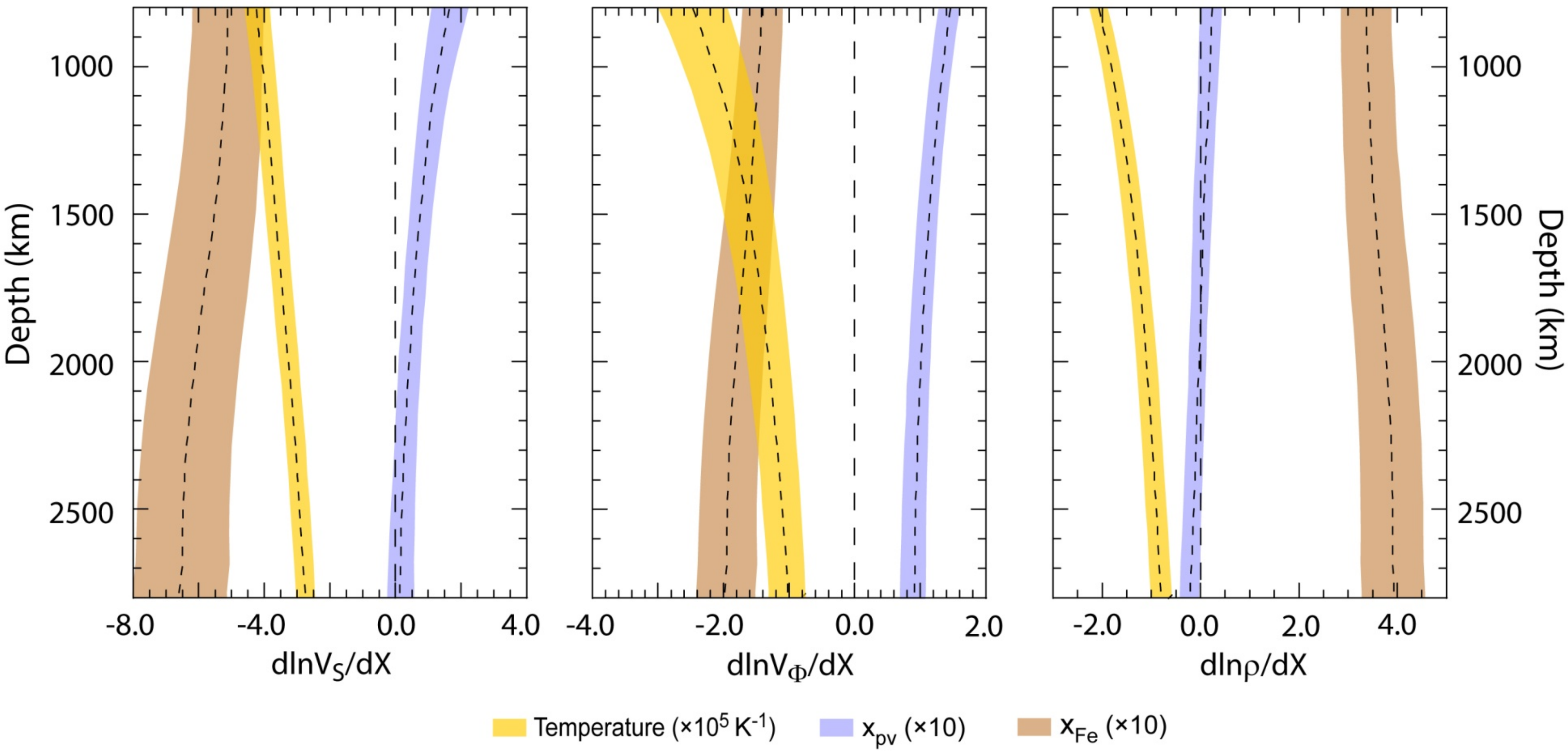

- Shear-wave velocity (V_S) is sensitive to iron and temperature, but not to bridgmanite.
- Bulk-sound velocity (V_Φ) increases with bridgmanite fraction: combined excesses of bridgmanite and iron lead to anti-correlation between V_S and V_Φ anomalies.
- Density increases with Fe fraction and decreases with temperature: positive density anomalies indicate iron excess.

Mantle structure: hints from seismic tomography

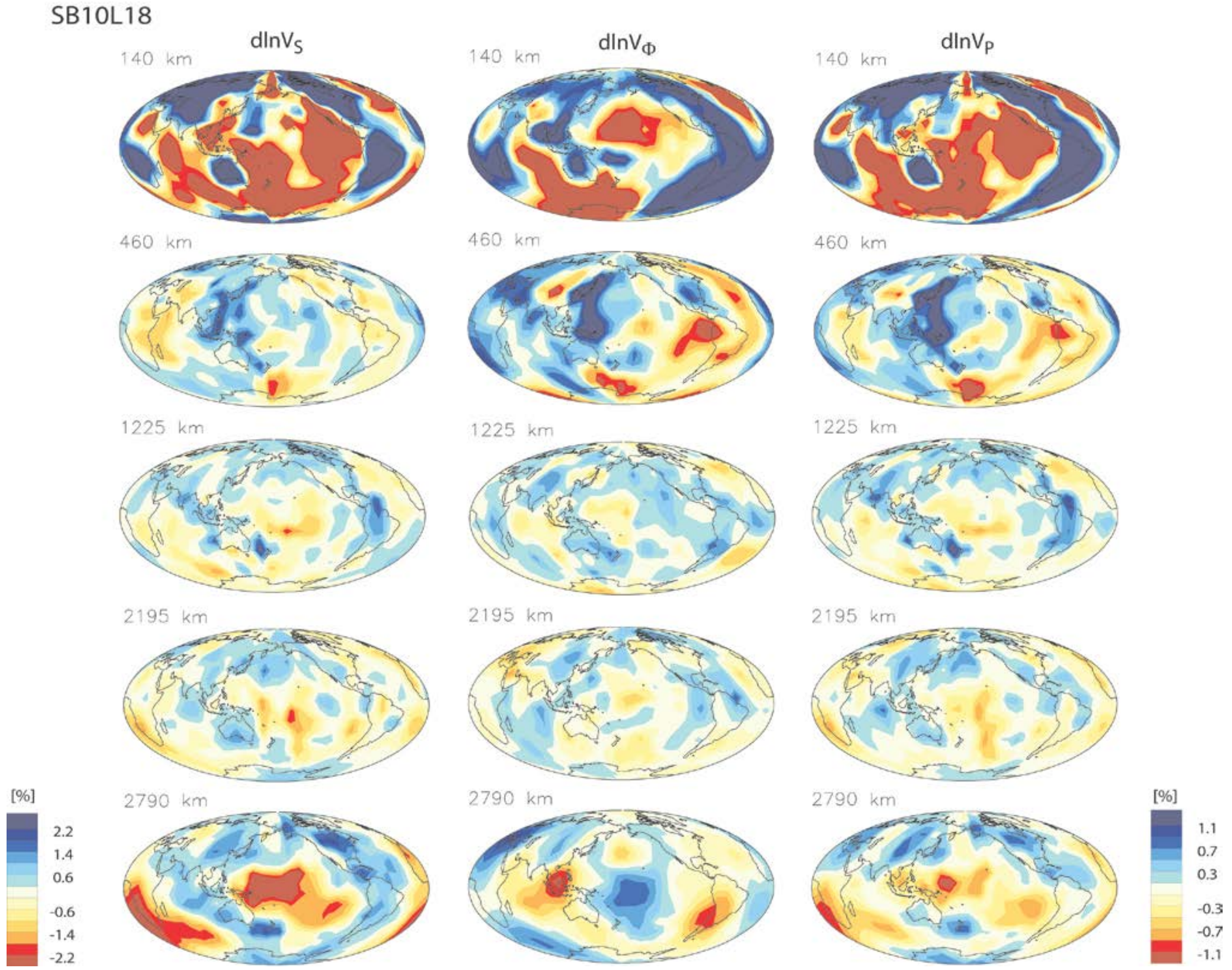

Masters et al. (2000)

V_S-V_Φ anti-correlation: supports thermochemical structure, but still ambiguous (*e.g.*, Schuberth et al, 2012; Davies et al., 2012).

Anti-correlation: purely thermal + post-perovskite

- The anti-correlation between $dlnV_S$ and $dlnV_\Phi$ may be explained with thermal anomalies + lateral variations in the stability field of post-perovskite only (*Davies et al.*, 2012).

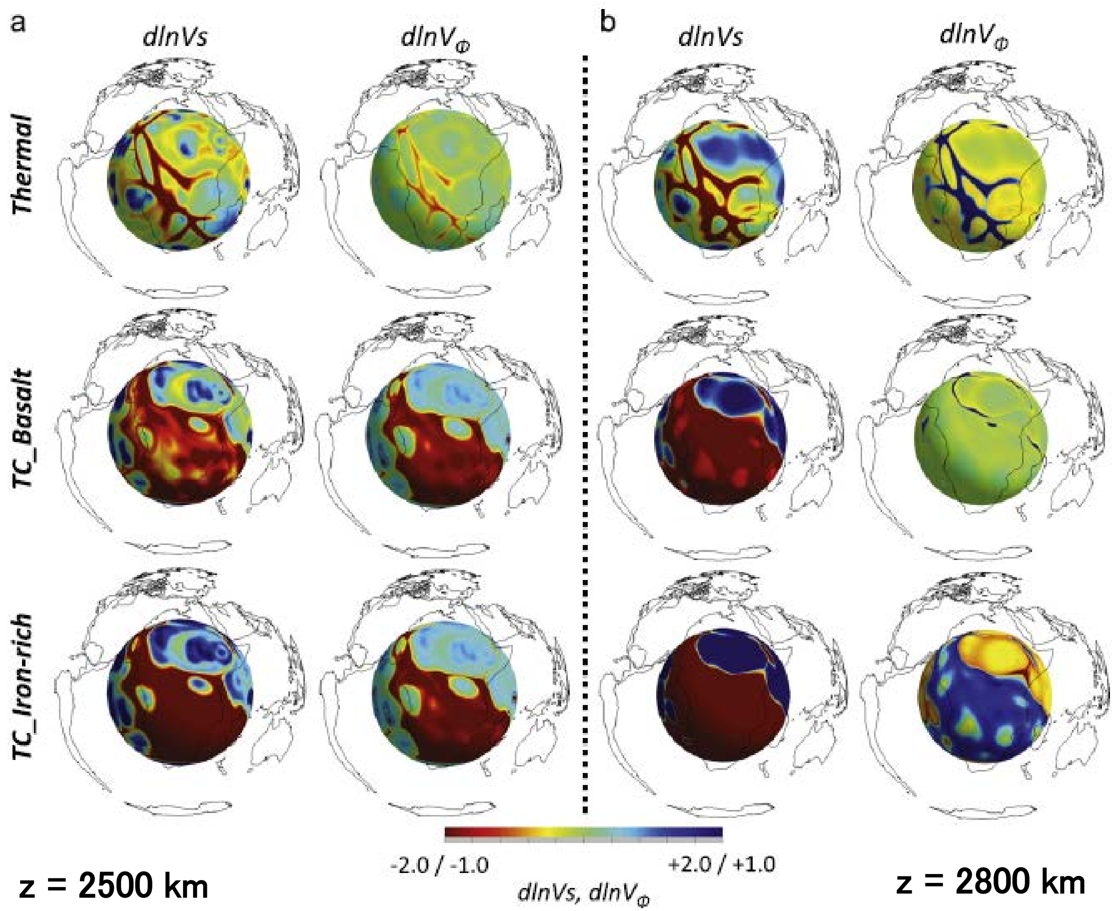

- Anti-correlation is confined in the lowermost 100-200 km, and anomalies from purely thermal models do not reproduce patterns observed in global tomography.

Shear-velocity maps: purely thermal + filtering

Shear and compressional velocities calculated from T and C distributions (+ mineral physics data) (Koelemeijer et al., 2018).

Purely thermal models of convection (plume clusters) can explain tomographic patterns with

- re-paramaterisation, to match tomographic models parameterisations.

- and appropriate filtering, to account for error and bias in tomographic models.

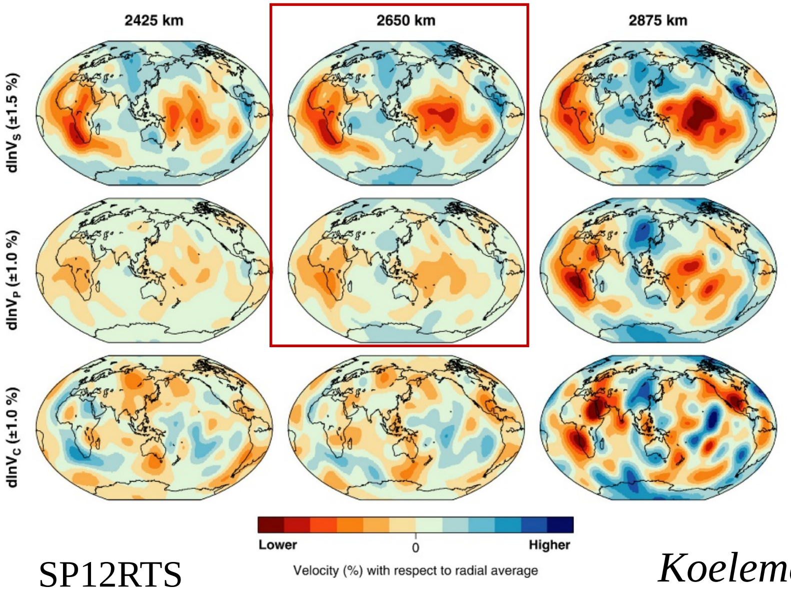

SP12RTS

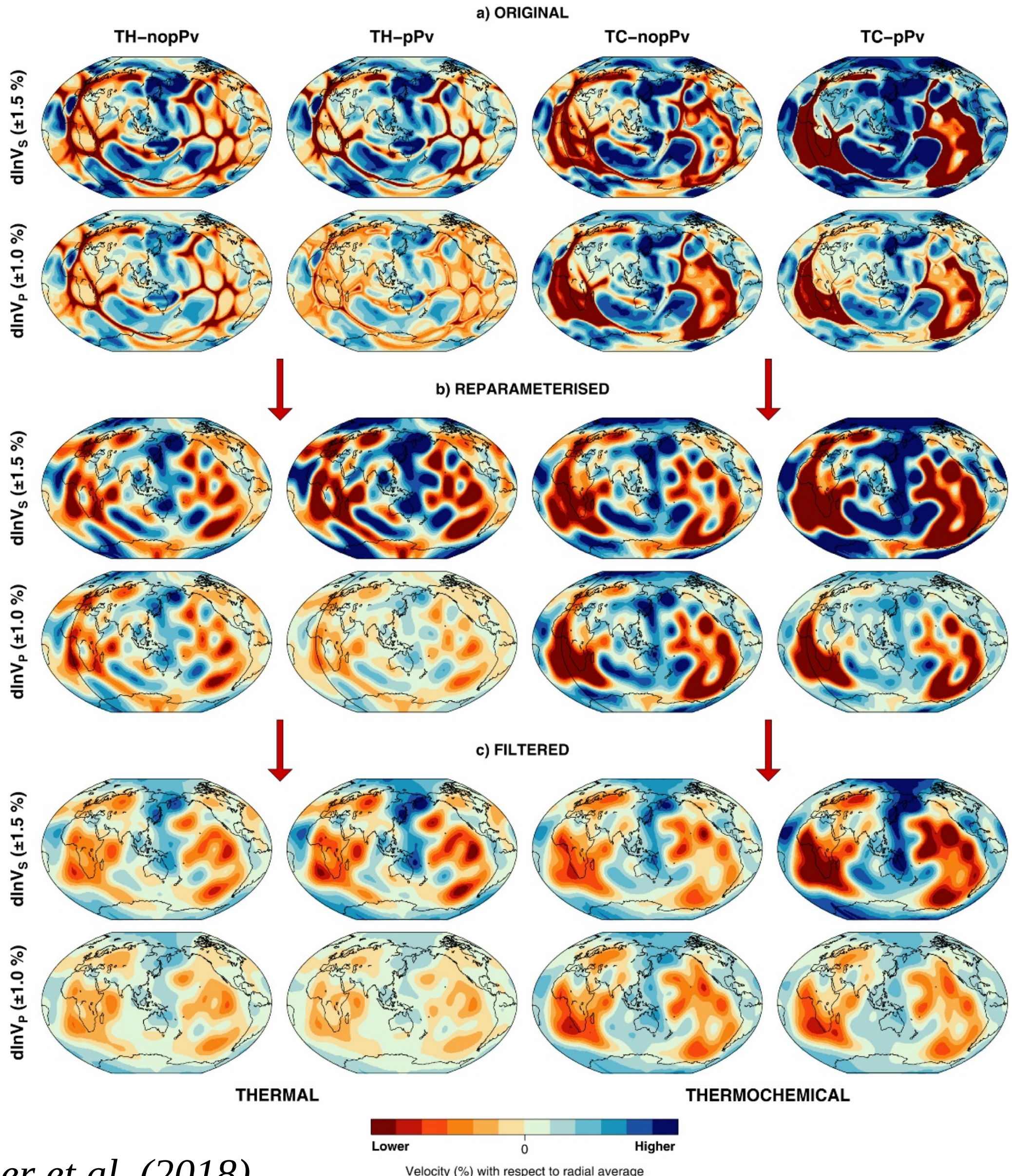

Koelemeijer et al. (2018)

Need additional constraints

- Geochemistry of Ocean Island Basalts (OIB) (*e.g.*, Helium ratio): requires hidden reservoir(s) of undegassed material..

- Normal modes: gives access to density, but still controversial (Ishii and Tromp, 1999; Trampert et al., 2004; Koelemeijer et al., 2017).

- Tidal tomography (Lau et al., 2017).

- Stability of LLSVPs: LIPs locations (Torsvik et al., 2008), polar wander (Dziewonski et al., 2010), mantle flow from plate tectonics reconstruction (Conrad et al., 2013).

- Gravitational coupling between mantle and inner core (MICG) (Chao et al., 2017; Ding and Chao, 2018).

- Dynamic topography at the Core-Mantle boundary (CMB).

- Seismic attenuation: a good proxy for temperature?

- Electrical conductivity inferred from magnetic field variations.

- Thermal conductivity: might influence CMB heat flux and core dynamics.

Probing the Earth with normal modes

- Free oscillations of the Earth: ${}_nS_l^m$ (n is radial number, l s.h. angular degree, and m azimuthal order)

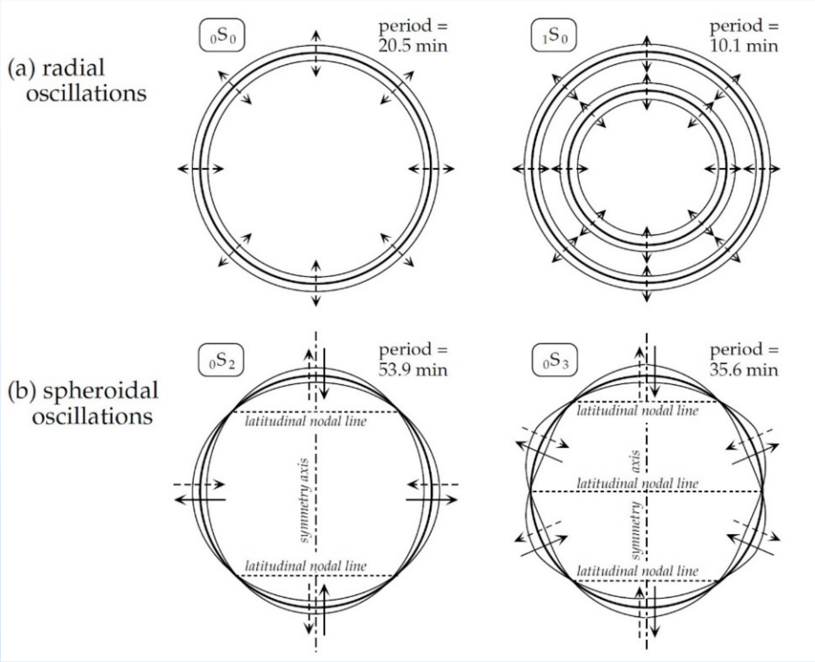

Lowrie, 2nd edition

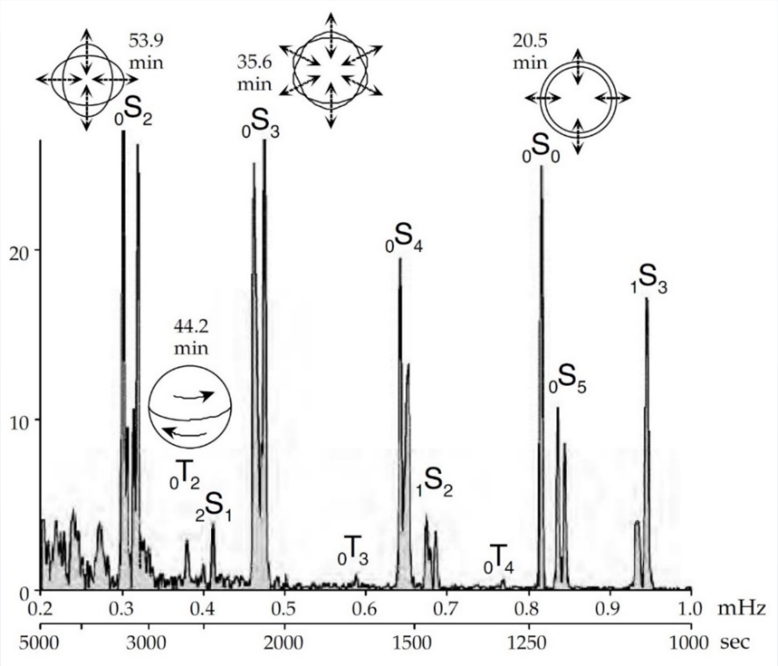

M = 9.0 Sumatra earthquake

- Modes split into different frequencies, depending on structure : ${}_nS_l \rightarrow 2l+1$ singlets appearing at different frequencies.
- Splitting function coefficients, measured from spectra of large earthquakes, give access to seismic velocities and density anomalies.

Normal mode tomography

- Even spherical harmonic degrees up to 4 (Ishii and Tromp, 1999) and 6 (Trampert et al., 2004; Mosca et al. 2012):

  - Shear- and bulk sound velocities anti-correlated.
  - Density and shear velocity de-correlated; ~ 1% density excess in LLSVPs.

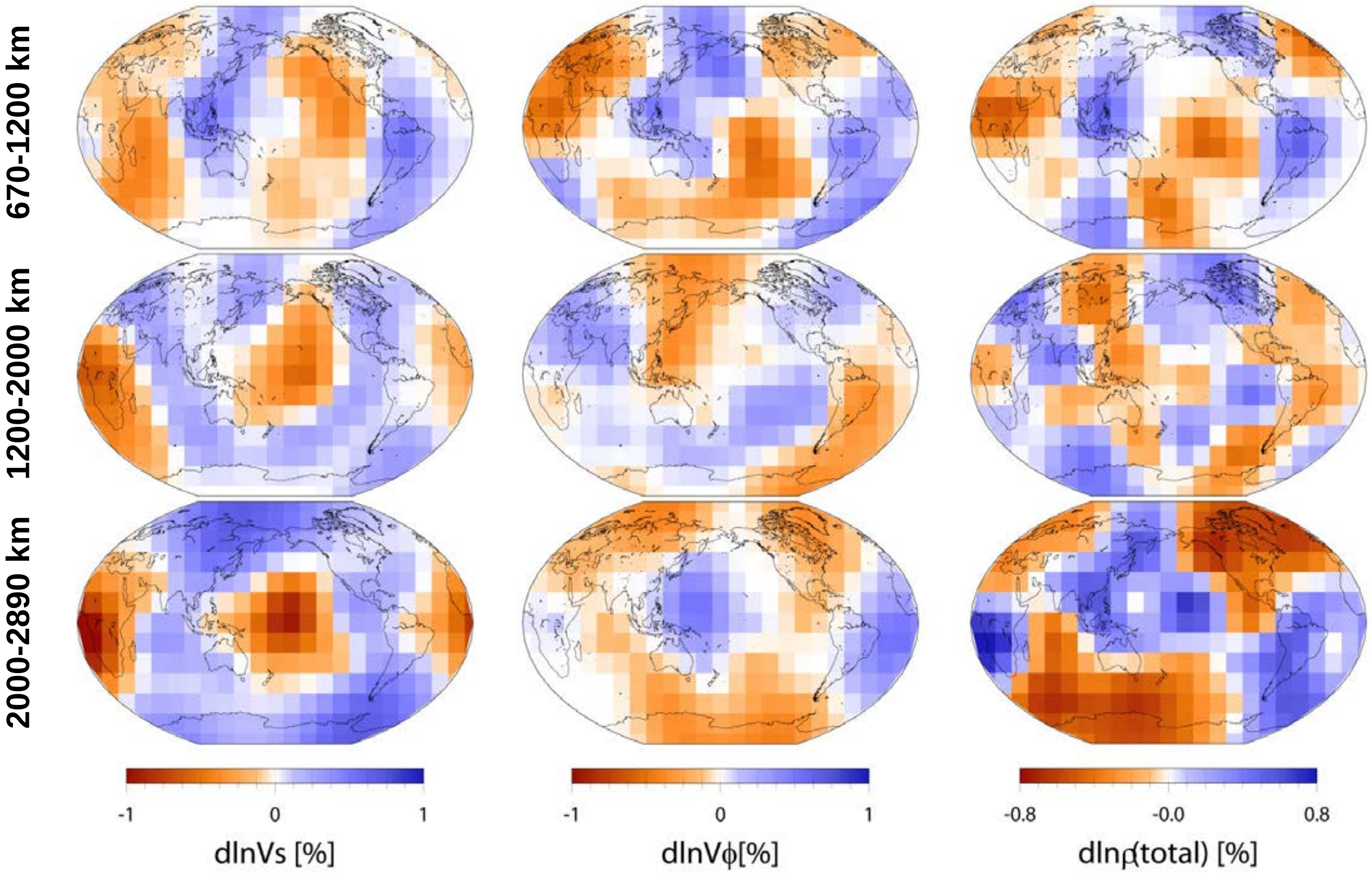

Trampert et al. (2004)

- Moulik and Ekström (2016): use normal modes splitting, body and surface waves to build shear- and compressional velocity and density maps:

- Correlated dlnρ (with $R = d\ln\rho/d\ln V_S$ fixed to 0.3) does not explain ${}_0S_2$ and toroidal modes.
- Unconstrained density provide best fit to these modes
- Density ~ 1% density excess in LLSVPs.

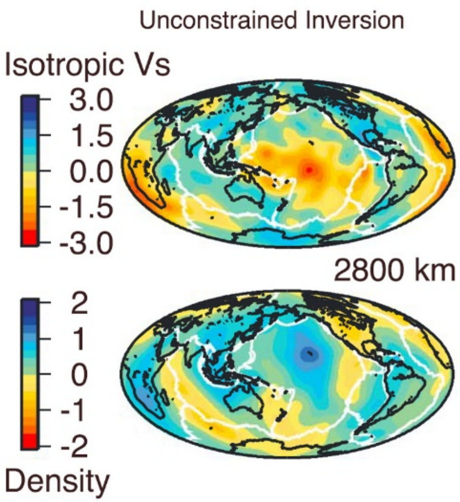

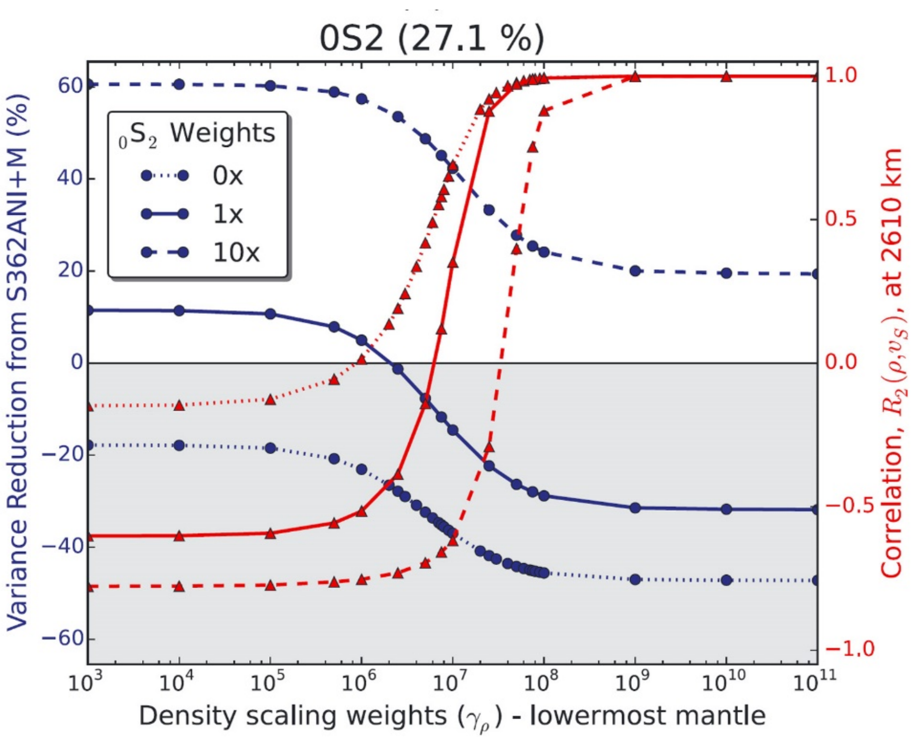

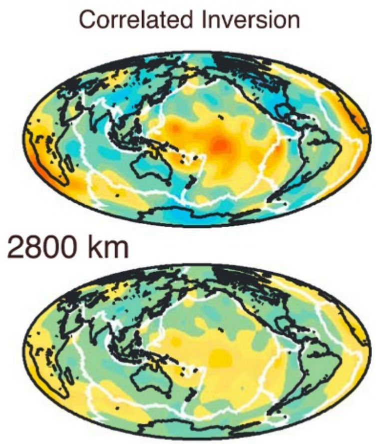

Moulik and Ekström (2016)

Stoneley modes prefer light LLSVP

- Koelemeijer et al. (2017): test possible density models against Stoneley modes splitting measurements (sampling lowermost mantle and upper outer core).

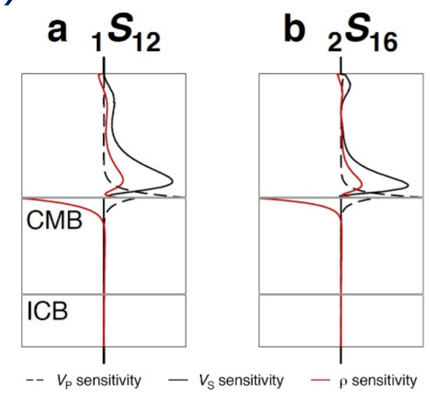

- Stoneley modes are better explained by light LLSVPs:

- Best fit ~ 0.57 for degree 2 models.

- Weaker preference if modes up to degree 8 are accounted for.

- No preference if other modes are added to Stoneley modes.

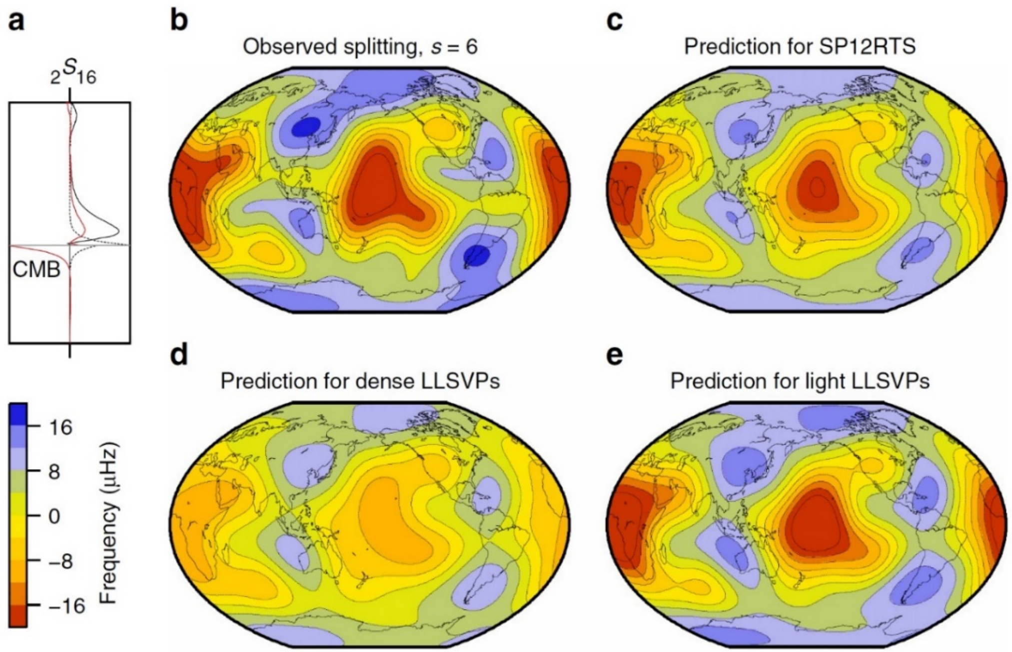

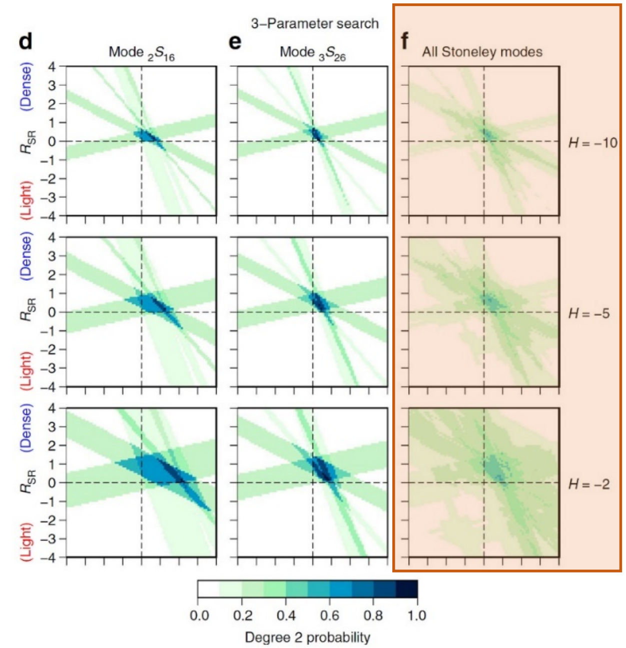

Koelemeijer et al. (2017)

Self-coupling approximation *vs* full coupling

- Modes are interacting with one another, which should be taken into account to calculate structure coefficients.

- Self-coupling: only account for coupling of singlet within a multiplet (*e.g.*, ${}_nS_2$) (off-diagonal blocks of splitting matrix set to zero).

- Narrowband coupling: nearby modes are grouped in clusters.

- Wideband coupling: all modes within a defined band (*e.g.*, up to 3 mHz) are coupled.

- Self-coupling and narrowband coupling simplify calculations, but may introduce bias and error in the inferred density structure (*e.g.*, Al-Attar et al., 2012; Yang and Tromp,2015).

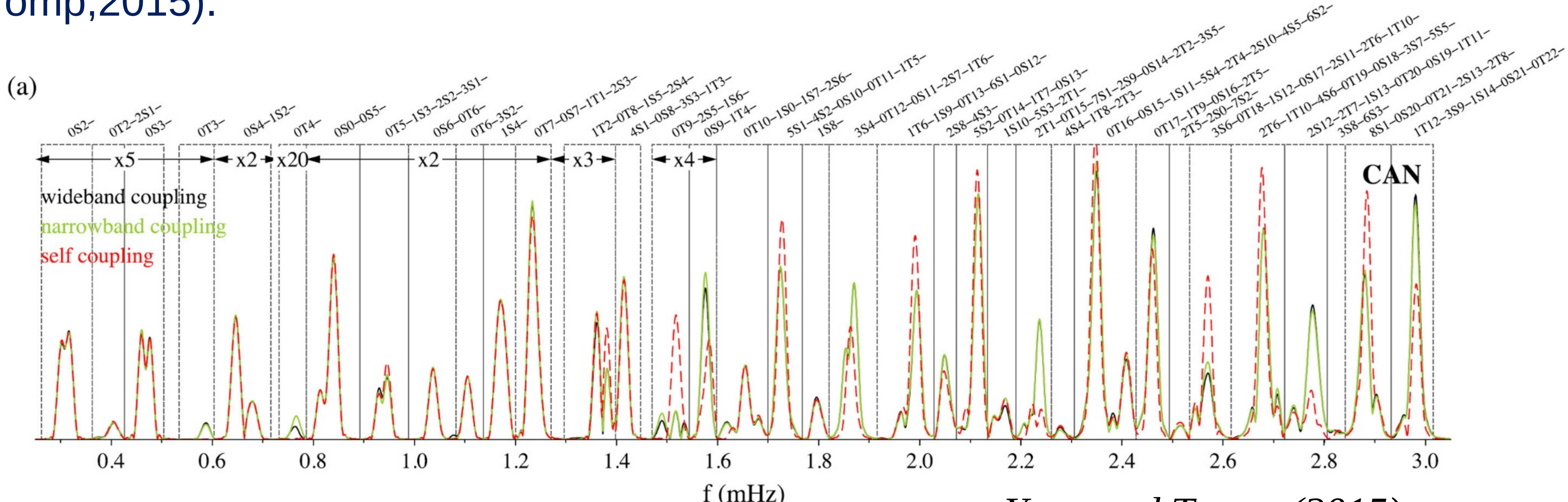

Yang and Tromp (2015)

Core-mantle boundary (CMB) topography

- Can be estimated (although difficultly) from seismic data (reflected phases).
- Dynamically, topography is induced by convective flow. At CMB:
  - Plumes pull the boundary upwards, inducing hills or ridges.
  - Slabs push the boundary, inducing depressions.

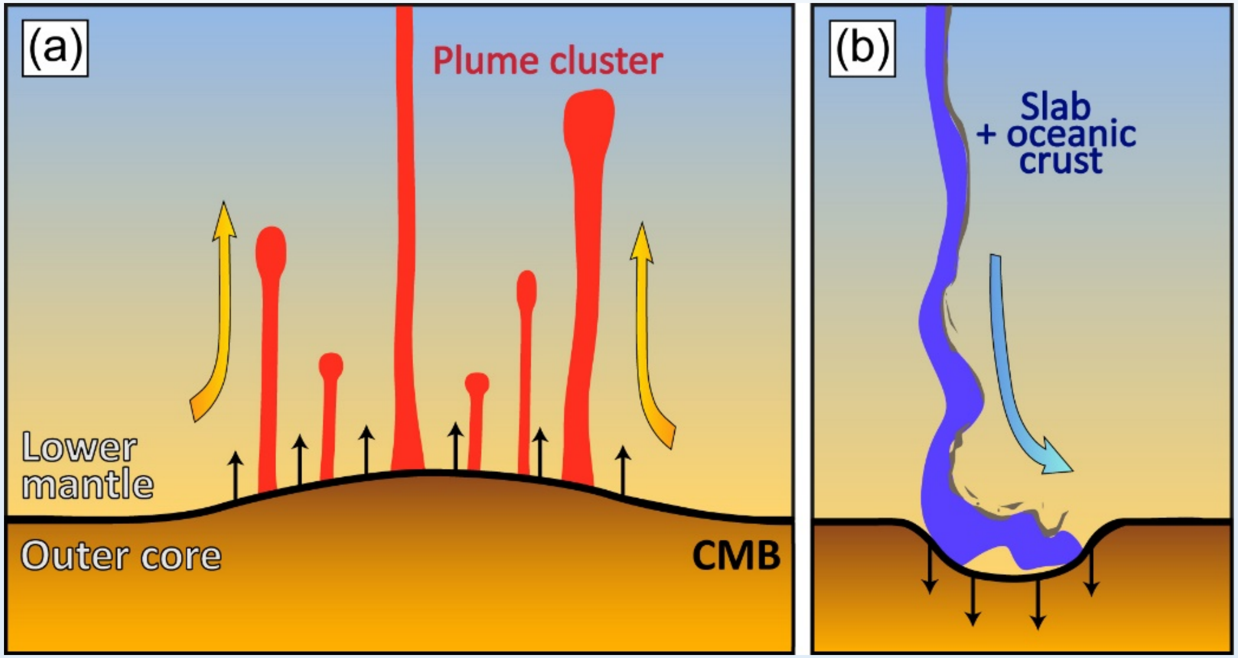

What is the effect of dense piles on CMB topography, and can it be distinguished from purely thermal topography ?

CMB topography: seismic observations

- Underside (PKKP) and upperside (PcP) reflected waves : 95% of topography distributed between -4.0 and +4.0 km (Garcia and Souriau, 2000).

- Normal modes: for spherical harmonic degree *l* = 2, the peak-to-peak amplitude should not exceed 5.0 km (Koelemeijer et al., 2012).

- Global CMB maps:

- Up to spherical harmonic degree *l* = 4.

- Strong discrepancies in amplitude (from 4 to 12 km) and patterns, depending on the model.

- Tanaka (2010): shallow depressions (~2-3 km) beneath Pacific and Africa.

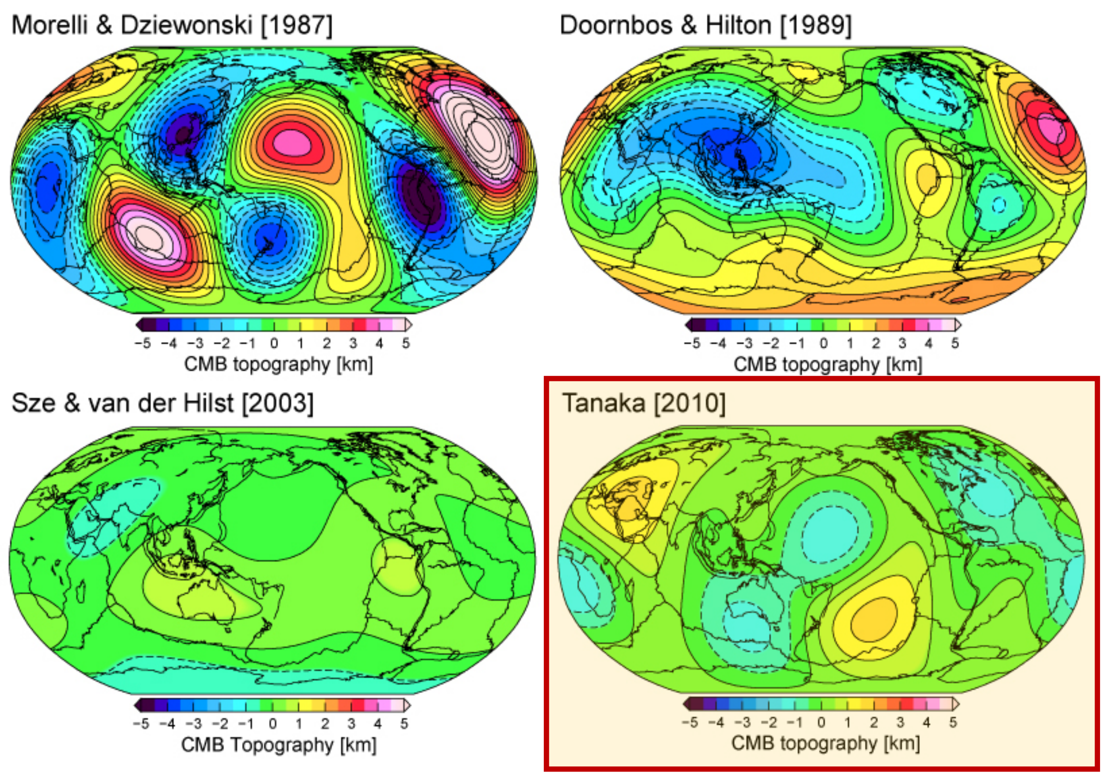

CMB topography from models of convection

- Numerical modeling of convection: solves the conservation equations of mass, momentum, energy, for flow (velocity) and temperature.

- Thermo-chemical convection: add conservation of composition for chemical field (e.g., slabs, or primordial material).

Chemical density contrast controlled by buoyancy ratio:

$$B = \frac{\Delta\rho_C}{\alpha\rho\Delta T_S}$$

- Some complexities:

- Mode of heating: basal and/or internal.

- Compressibility.

- Rheology: viscosity may depend on temperature, depth, and composition + yield stress to avoid stagnant lid at surface.

- Dynamic topography calculated from the normal stress at the CMB, and accounts for self-gravitational effects:

$$h_{\mathrm{CMB}} = \frac{\sigma_{zz} + \Phi_{\mathrm{CMB}}\Delta\rho_{\mathrm{CMB}}}{\Delta\rho_{\mathrm{CMB}}\, g}$$

CMB topography from purely thermal models

- Downwellings (slabs) induce local but deep (up to 10 km) depressions in the CMB.

- Upwellings induce positive CMB topography with amplitude ~ 2-3 km.

- Amplitude of topography decreases with increasing thermal viscosity contrast

Plumes are hotter, thus less viscous, which reduces the normal stress at CMB beneath plumes.

- Presence of post-perovskite : does not substantially modify the topographic pattern.

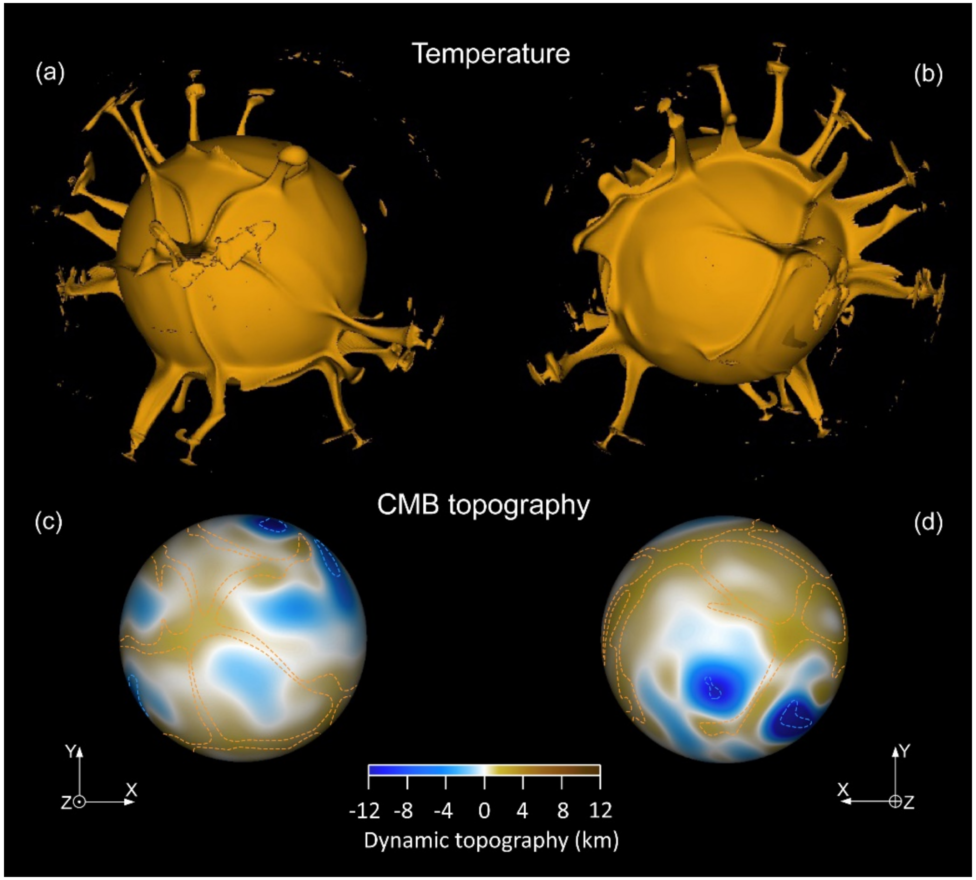

Deschamps et al. (2018)

CMB topography from thermo-chemical models

- Thermo-chemical models with density contrast $\Delta\rho_C$ = 140 kg/m^3.

2 large antipodal reservoirs of dense material are formed, with plumes generated at their tops.

- Reservoirs of dense material induce wide depressions ~1.5 km deep.

- Amplitude of topography:

- Decreases with increasing thermal viscosity contrast

- Increases with chemical viscosity contrast.

- Downwellings induce local, but deep depressions in the CMB.

- Topography is not affected by the presence of post-perovskite.

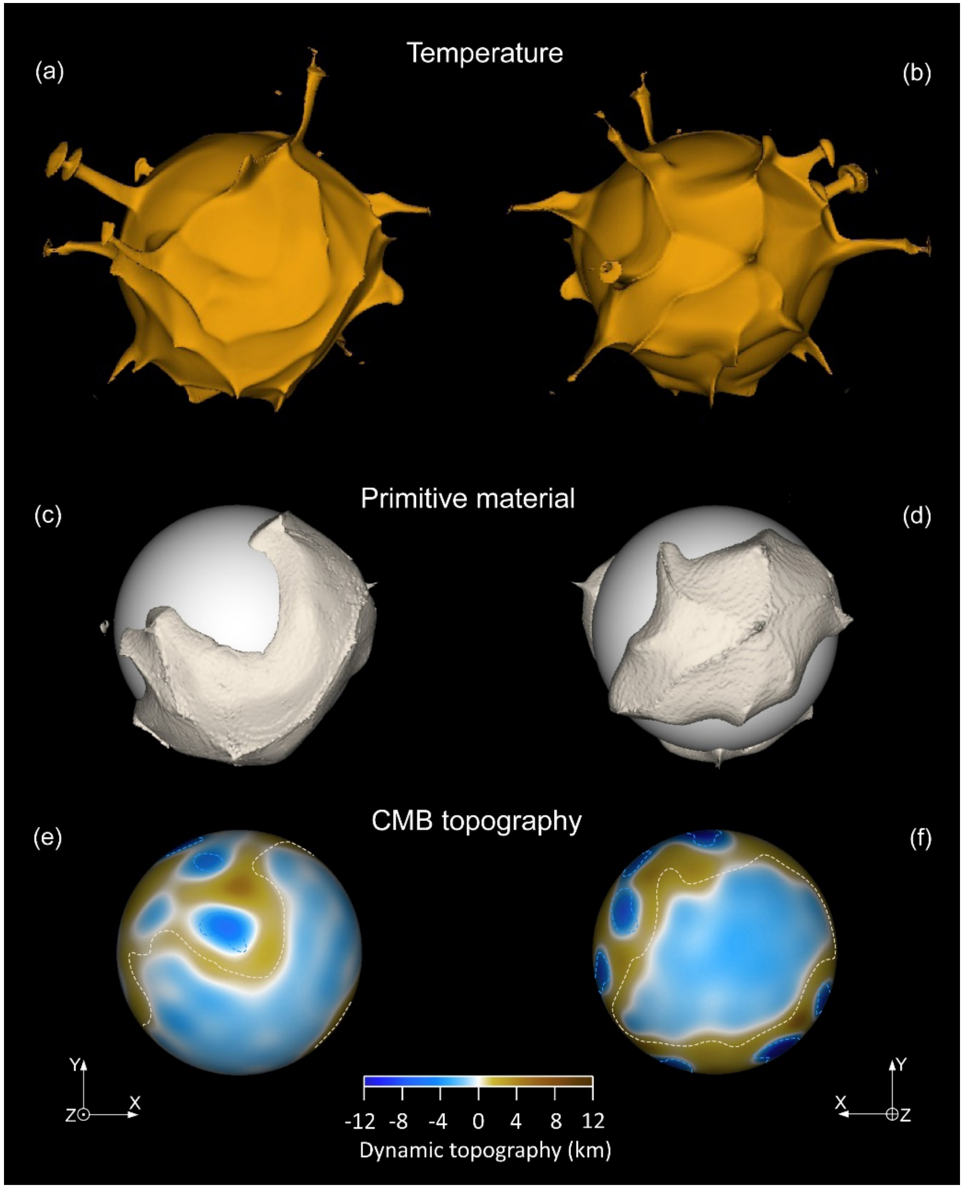

Deschamps et al. (2018)

Comparison with seismic observations

Filter		T1	TC1	TC4	TC7	Observed
l = 2	rms	1.25	0.72	1.12	0.24	
	A	5.10	2.34	4.44	0.91	≤ 5.0 (from normal modes, Koelemeijer et al., 2012)
l = 0-2	rms	1.25	0.72	1.12	0.24	
	A	5.13	2.36	4.45	0.92	
l = 2, 4	rms	1.31	0.87	1.19	0.60	
	A	6.56	3.47	5.38	2.66	5.0 (Tanaka, 2010)
l = 0-4	rms	1.56	1.04	1.58	0.71	
	A	8.51	4.35	7.62	3.49	12.0 (Morelli & Dziewonski, 1987)
						8.0 (Doornbos & Hilton, 1989)
						4.0 (Sze & v.d. Hilst, 2003)
						3.5 (Koper et al., 2003)

- Overall, amplitude of topography from thermo-chemical models with density contrast larger than ~100 kg/m^3 agree with observations better than purely thermal or slightly thermo-chemical models.
- Tanaka (2010) : slight depressions below LLSVPs : consistent with thermo-chemical models.

Long-wavelength topography *vs* tomography

- Compare long-wavelengths (l = 0-4) of CMB topography and shear-wave velocity anomalies ($d\ln V_S$) from convection models.

- Purely thermal (T1) and thermo-chemical models with small density contrast (e.g., TC4 with $\Delta\rho_C$ = 90 kg/m³) :

$d\ln V_S$ and topography are anti-correlated (negative $d\ln V_S$ are associated with positive topography).

- Thermo-chemical models with large density contrast ($\Delta\rho_C$ > 100 kg/m³), e.g., TC1 and TC7 :

$d\ln V_S$ and topography are correlated.

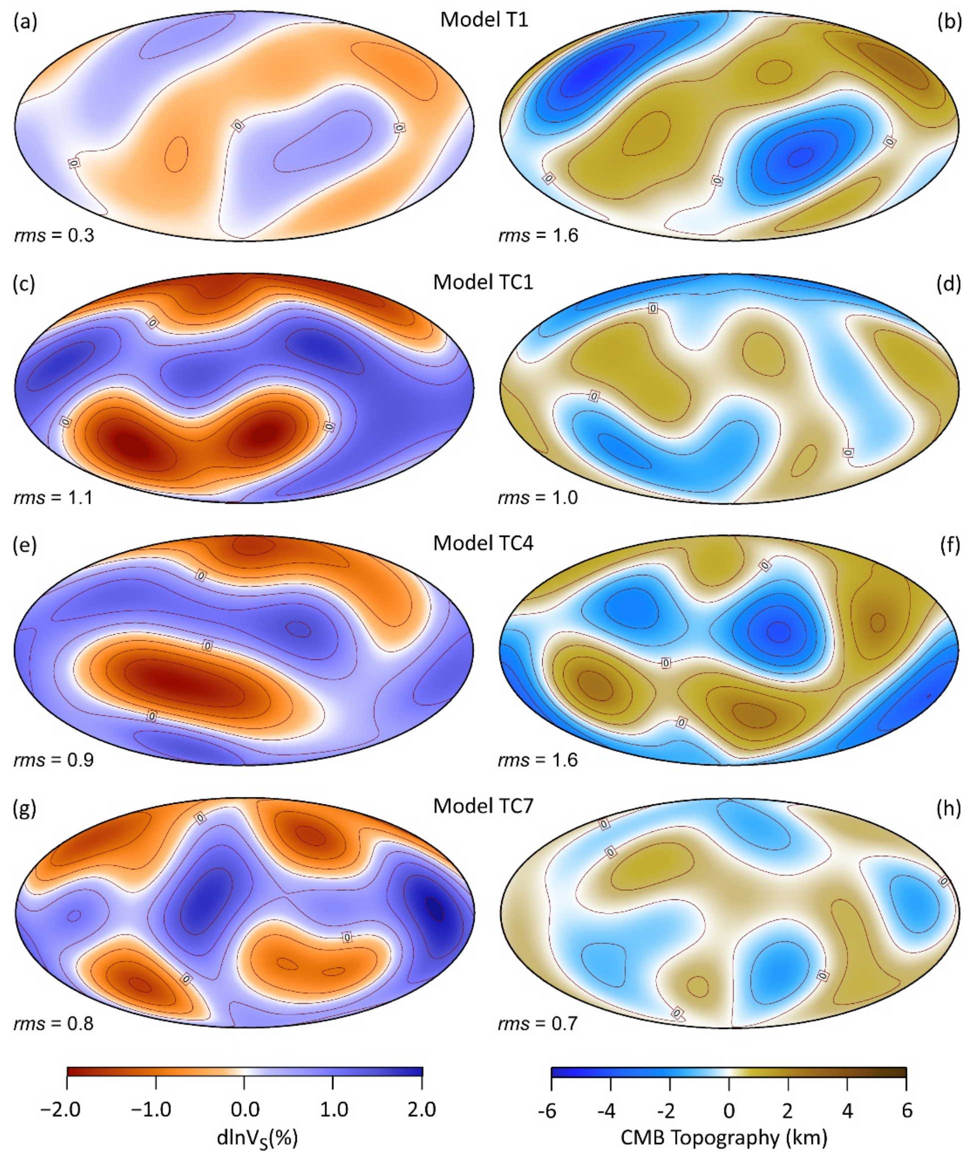

Topographic profiles at CMB

Slopes predicted by models of mantle convection are rather gentle, up to ~ 15 m/km in the case of slabs.

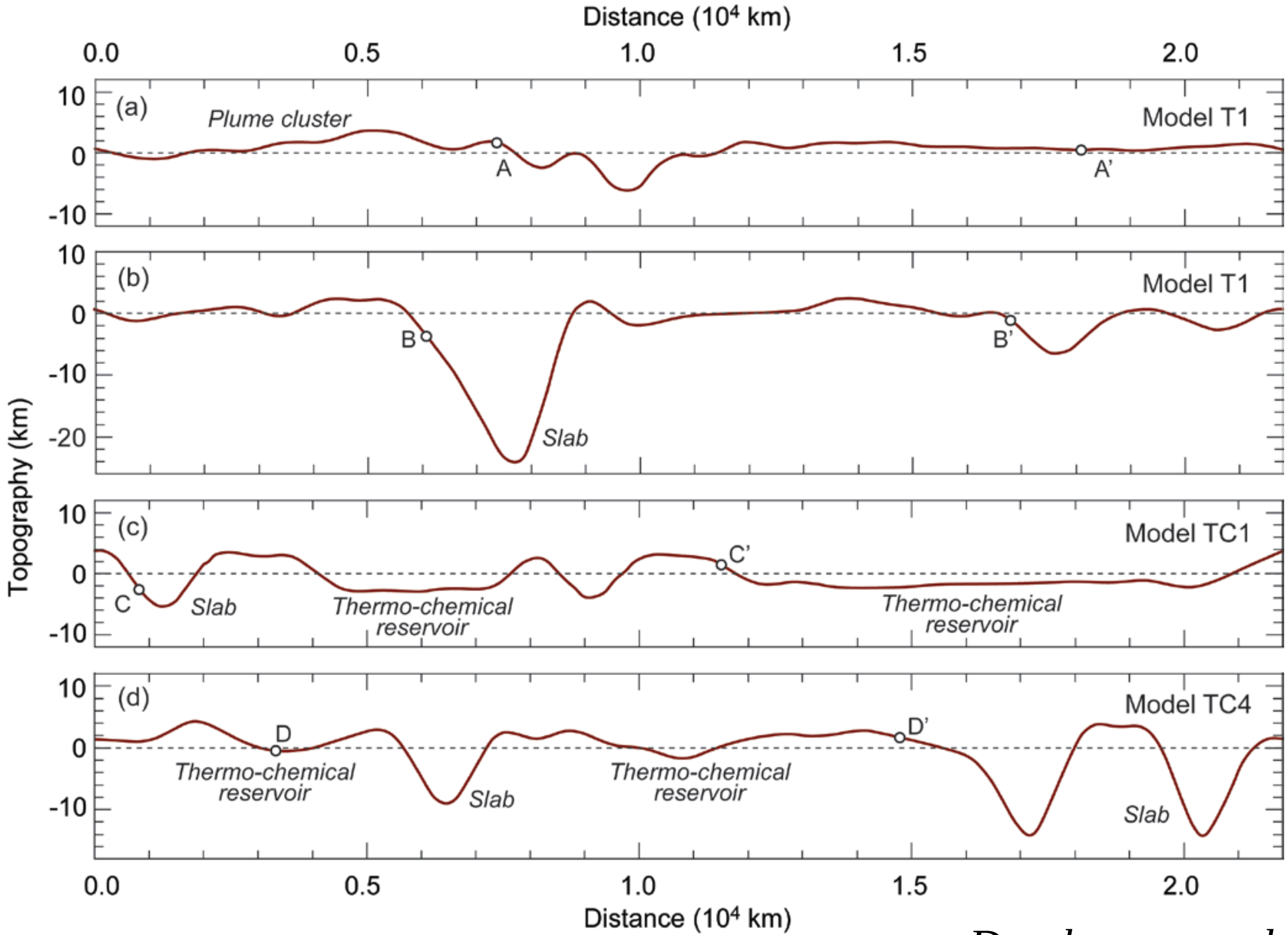

Deschamps et al. (2018)

Is it enough to impact outer core flow?

Seismic attenuation

▸ Even at short timescales, the Earth mantle is not perfectly elastic. This is due to the presence of default in the crystalline structure (dislocation).

Part of the elastic energy is dissipated, seismic waves are attenuated.

▸ Attenuation can be measured with the quality factor, *Q*. Large quality factor means low attenuation and vice-versa.

In the Earth's mantle, Q ~ 50-500.

▸ Attenuation is a thermally activated process. It also depends on seismic wave frequency:

$$Q = Q_0 \omega^{\alpha} \exp(\alpha H/RT)$$

- Q increases with pressure and decreases with temperature (attenuation decreases with pressure and increases with temperature).

- H is activation enthalpy, $H = E_a + pV_a$ with $V_a > 0$.

Q: a good constraint for temperature ?

Frequency band model

- Attenuation is large only within a frequency range and sharply drop outside this band (Anderson and Given, 1982).

- Shape of the frequency band is controlled by the frequency-exponent α, which depends itself on frequency.

- For lower mantle (Lekić et al., 2009):

- $\alpha = 0.3$ for $T < 200$ s

- $\alpha = 0.1$ for $300 < T < 800$ s

- $\alpha < 0$ for $T > 1000$ s

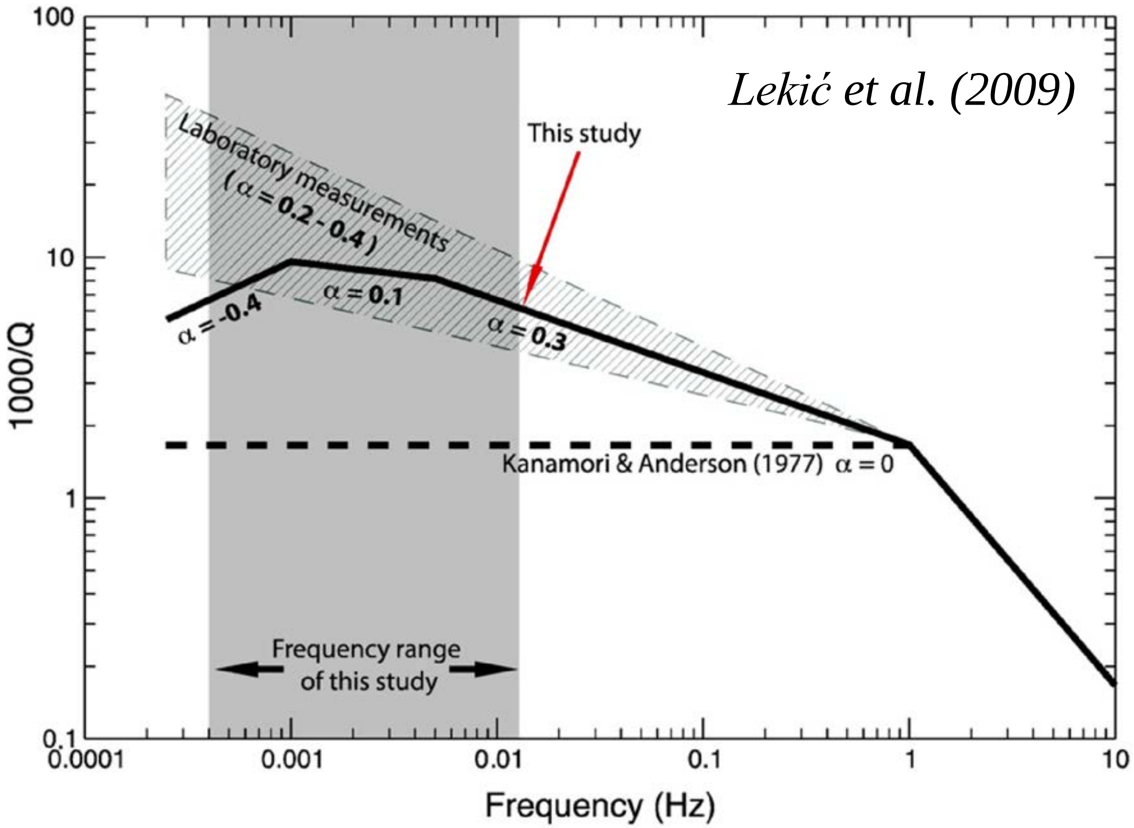

Waveform inversion for models of Q_μ and V_S

Inversion of seismic waveform data for models of Q and dlnV_S in Western Pacific (sampling western tip of LLSVP), and Northern Pacific.

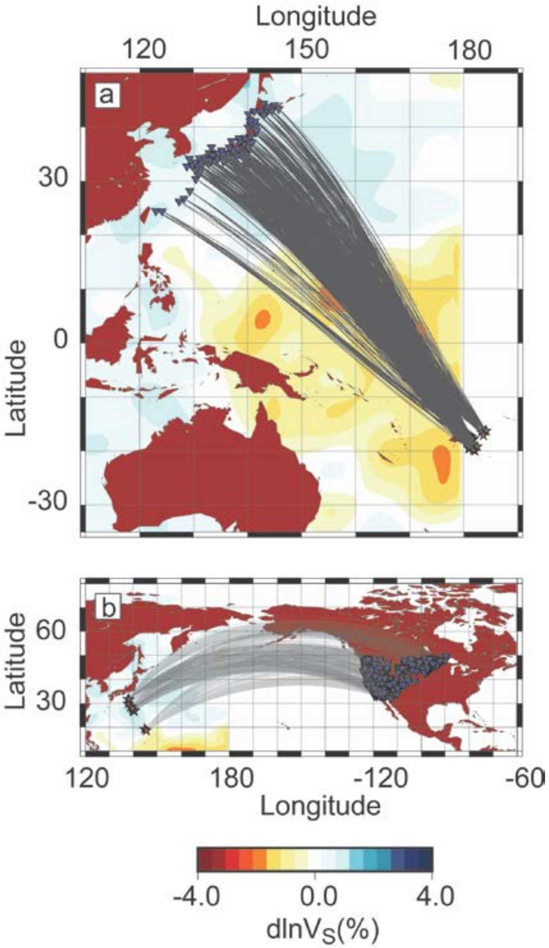

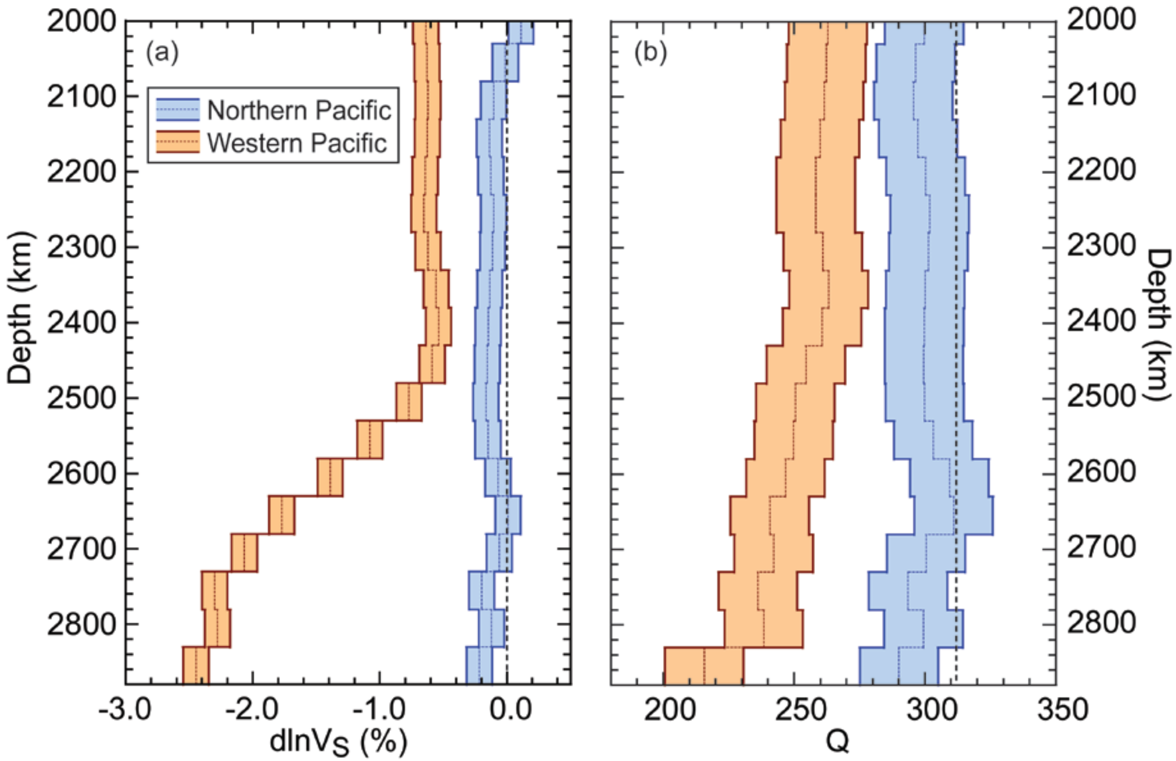

Western Pacific profiles taken from Konishi et al. (2017)

Q , a proxy for temperature ?

- Q-factor depends on temperature and frequency of seismic wave:

$$Q(\omega, T) = Q_0 \omega^{\alpha} \exp\left(\frac{\alpha H}{RT}\right)$$

- Horizontally averaged mantle, $T = T_{\mathrm{ref}}$, $Q = Q_{\mathrm{ref}}$ (*e.g.*, $Q_{\mathrm{PREM}} = 312$):

$$Q_{ref} = Q(\omega, T_{ref}) = Q_0 \omega^{\alpha} \exp\left(\frac{\alpha H}{RT_{ref}}\right)$$

$$dT = T - T_{ref} = -\frac{RT_{ref}{}^2}{\alpha H} \frac{\ln\left(\frac{Q}{Q_{ref}}\right)}{\left[1 + \frac{RT_{ref}}{\alpha H} \ln\left(\frac{Q}{Q_{ref}}\right)\right]}$$

- Parameters T_{ref} (mantle geotherm), α, and H not well known:

- T_{ref} at CMB in the range 3200-4200 K.

- α should be ~ 0.3 for periods ≤ 200 s (Lekić et al., 2009).

- *H* increases with pressure. In lowermost mantle should be in the range 260-900 kJ/mol (Matas and Bukowinski, 2007), but most likely around 300-500 kJ/mol.

Radial models of temperature from Q and V_S

- Calculate temperature anomalies independently from Q and $d\ln V_S$:

$$dT_{VS} = \frac{d\ln V_S - S_{Fe} dx_{Fe} - S_{pPv} dX_{pPv}}{S_T}$$

- dT_Q and dT_{VS} for purely thermal $d\ln V_S$ agree at NP, but disagree at WP.

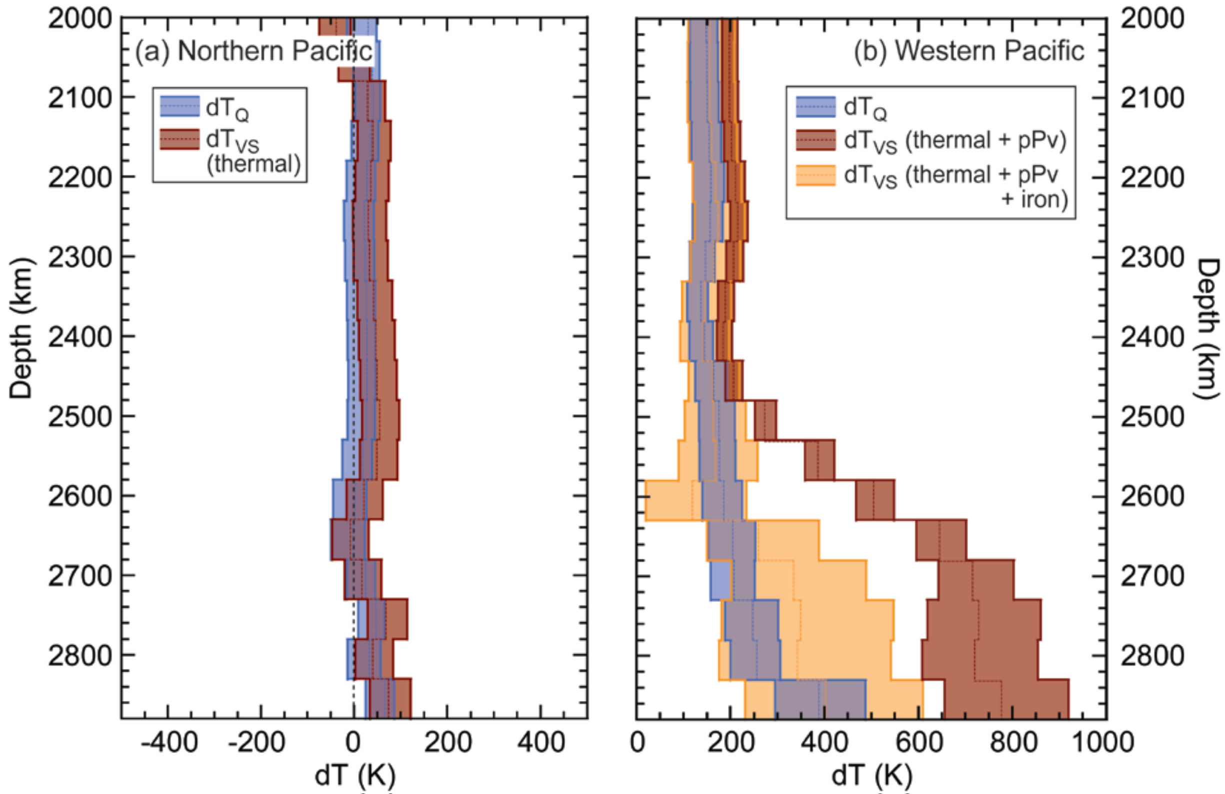

Purely thermal origin explain $d\ln V_S$ at NP, but compositional changes are required at WP.

Radial models of iron from V_S residuals

- Assume temperature anomaly from Q (dT_Q).

- Get iron anomaly from the part of $d\ln V_S$ unexplained by dT_Q and assumed post-perovskite depletion):

$$dx_{Fe} = \frac{d\ln V_S - S_T dT_Q - S_{pPv} dX_{pPv}}{S_{Fe}}$$

S_T, S_{Fe}, S_{pPv} : sensitivities of V_S to temperature, iron and pPv.

- Iron excess in LLSVP (2600 km depth down to CMB) ~ 3-4 %.

- Iron excess at shallower depth around 0.4-0.5 % : entrainment by the Caroline plume ?

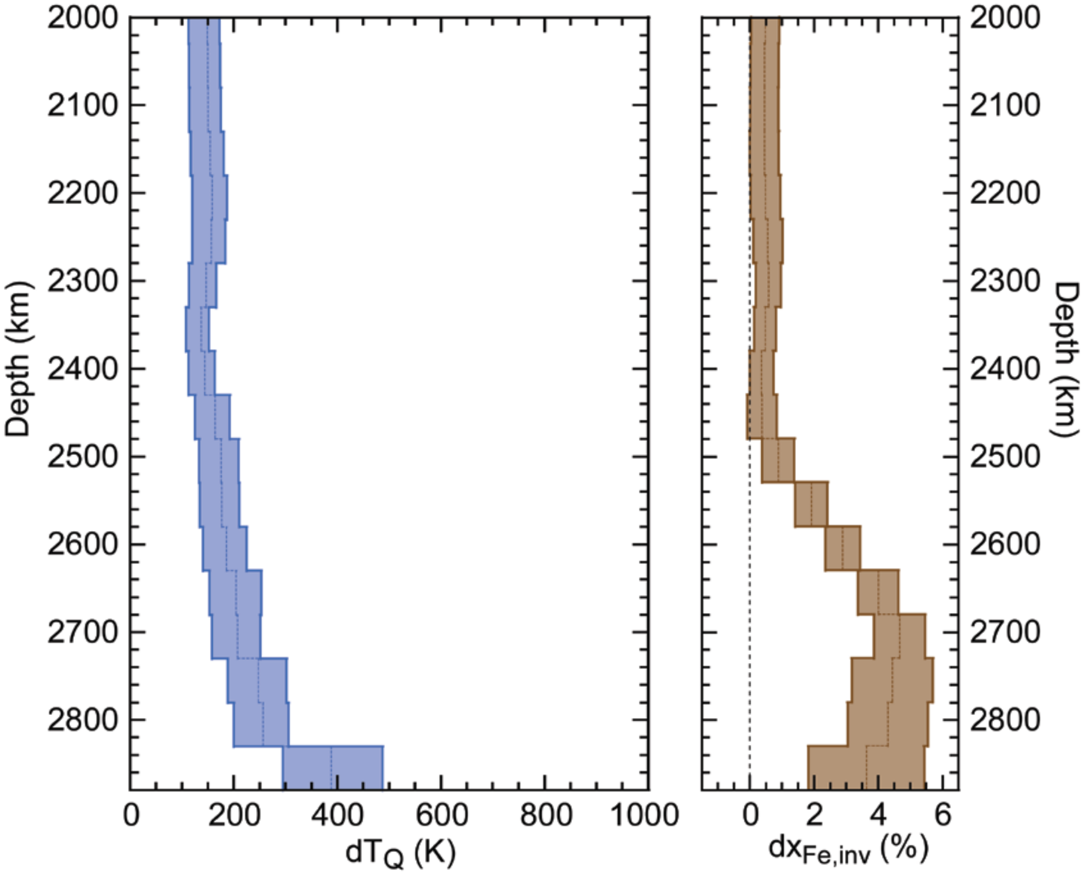

Other hints

- Tidal tomography (Lau et al., 2018).
- Variations in Earth's rotations (Ding and Chao (2018).

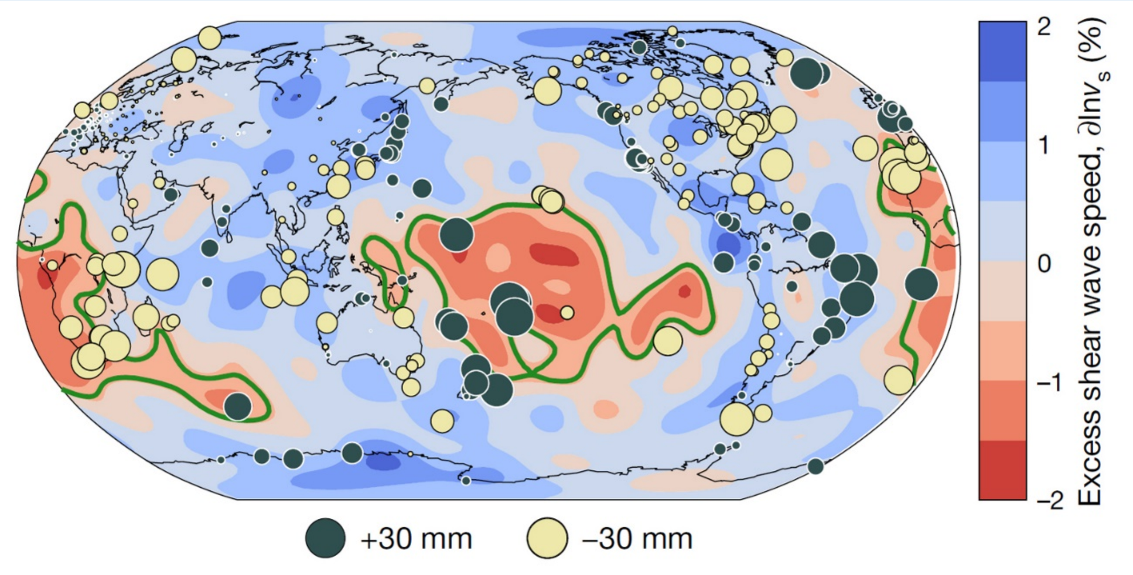

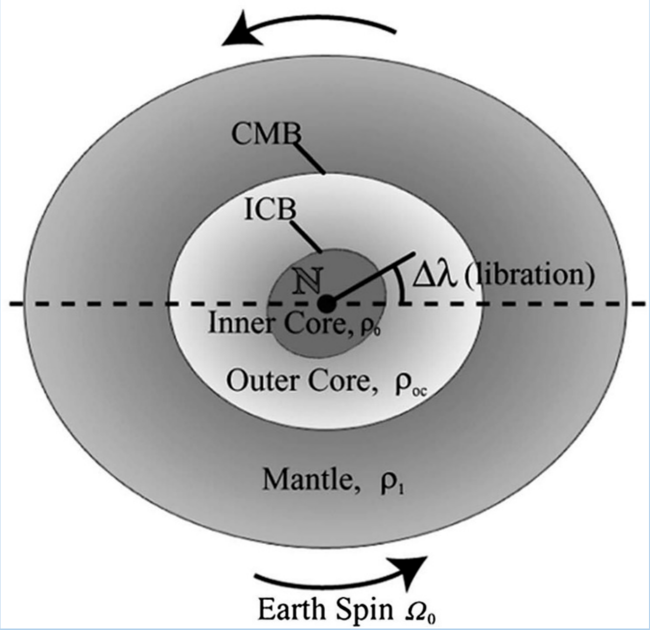

Tidal tomography

- Lau et al. (2017): use seismic normal mode summation to reconstruct solid Earth tides:

- Fit solid tides measurements deduced from GPS data to calculate density.

- Use full mode coupling (no self-coupling approximation).

- Vertical parameterisation: 3 layers in lowermost 1000 km.

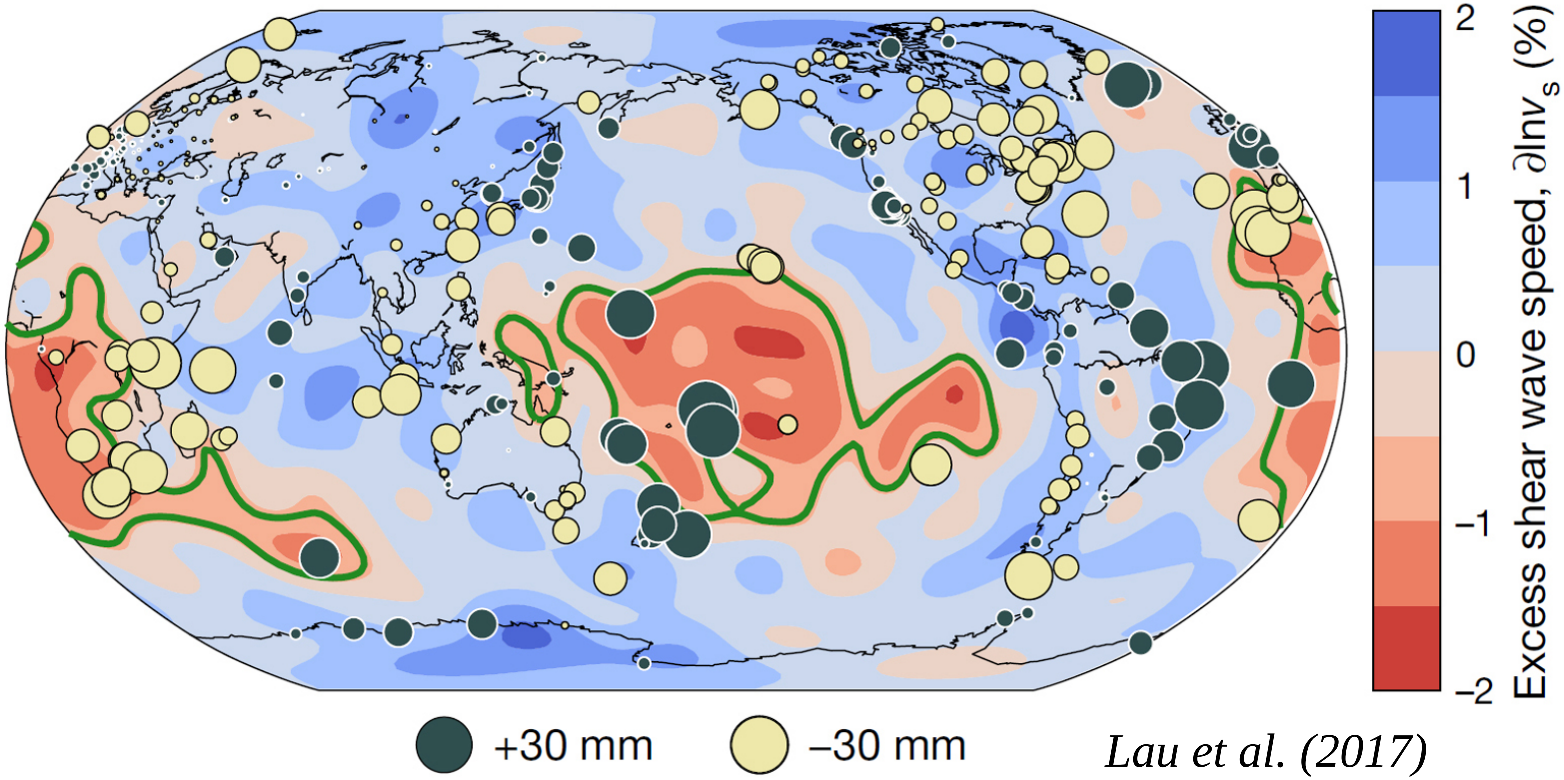

Lau et al. (2017)

Tidal tomography

- Lowermost 350 km layer: excess density ~ 0.5 % in LLSVPs.

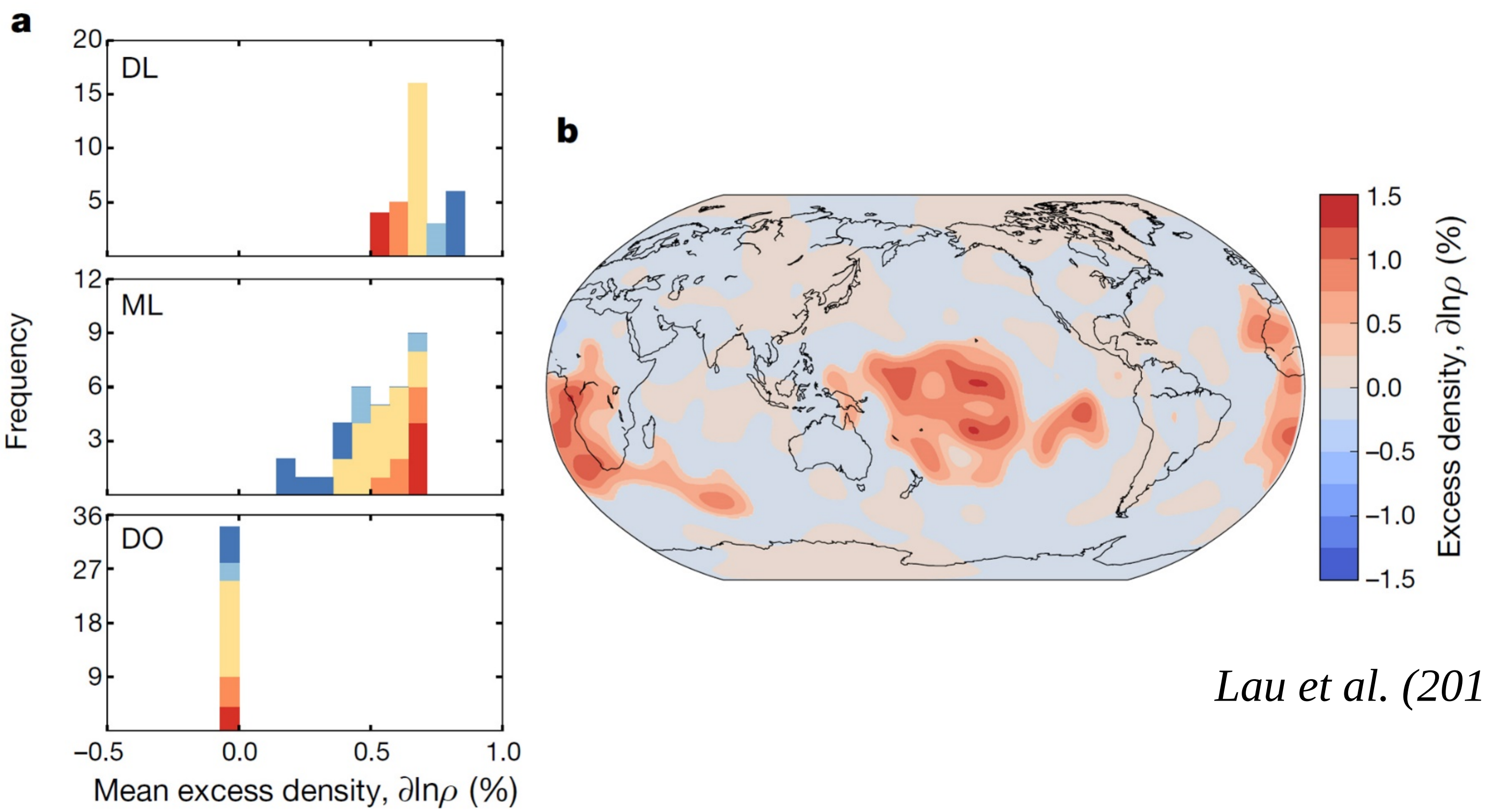

Lau et al. (2017)

- Average value over 350 km: evenly distributed density anomalies throughout the layer, or stronger anomalies concentrated in thinner layers and specific locations (*e.g.*, plumes' feet) ?

Hints from variations in Earth rotation

- 6-year oscillation (SYO) in the length-of-the-day (LOD) with amplitude 0.13 ms.

- Mound and Buffet (2006): related to gravitational coupling between mantle and inner core.

- Chao (2017): torsional libration of the inner core, with coupling constant L = 6.5×10^{19} Nm.

- Ding and Chao (2018): SYO in surface displacement (measured from GPS, ~ 4.3 mm in amplitude), in phase with LOD (strongest displacement synchronized with shortest LOD).

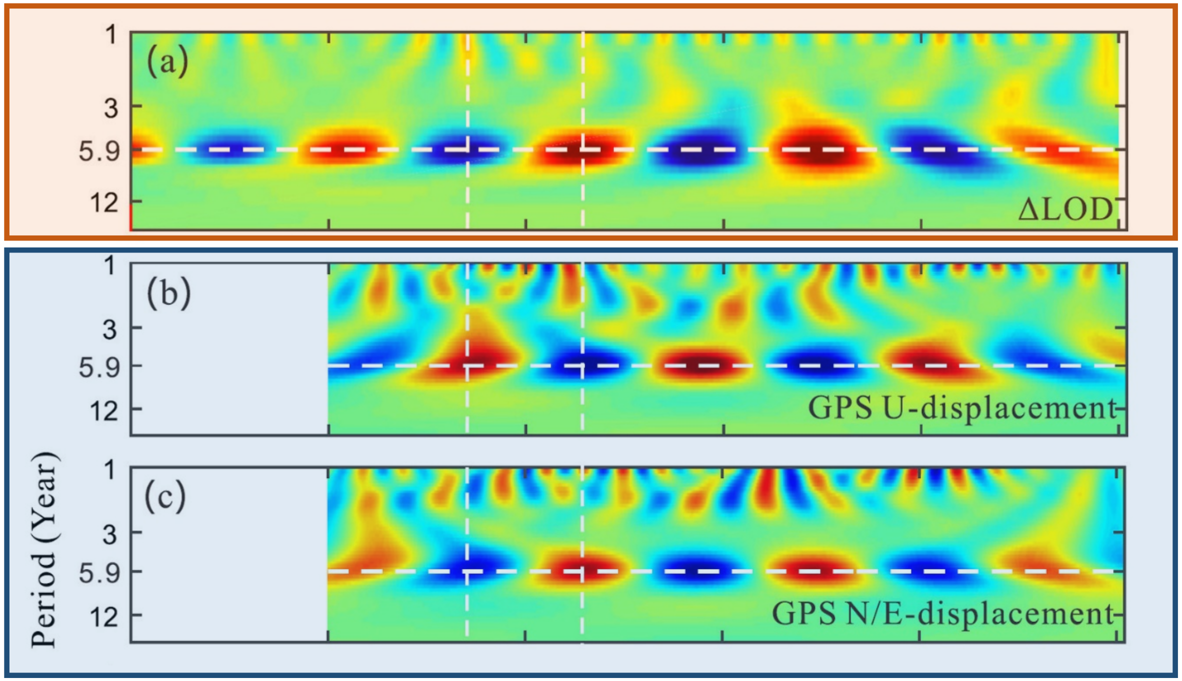

Ding and Chao (2018)

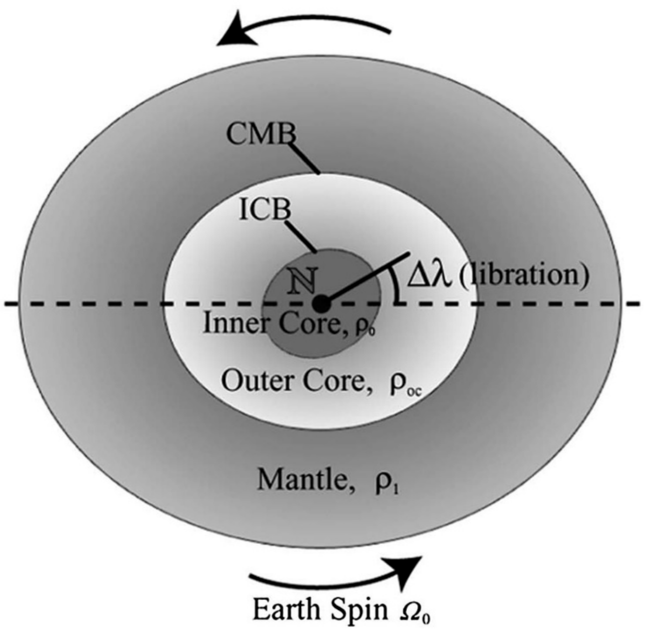

Chao (2017)

Hints from variations in Earth rotation

- A possible scenario (Ding and Chao, 2018):

- Mantle inner-core gravitational (MICG) coupling induces a 6-yr libration of the inner core.

- Transfer of angular momentum to the mantle result in a 6-yr oscillation in LOD.

- Inner-core libration induces pressure wave travelling through the outer core and transmitted to the mantle …

- … resulting in a 6-yr oscillation in the surface displacement.

- Equilibrium MICG coupling alignment coincides with LLSVPs major axis:

- Implies denser than average LLSVPs.

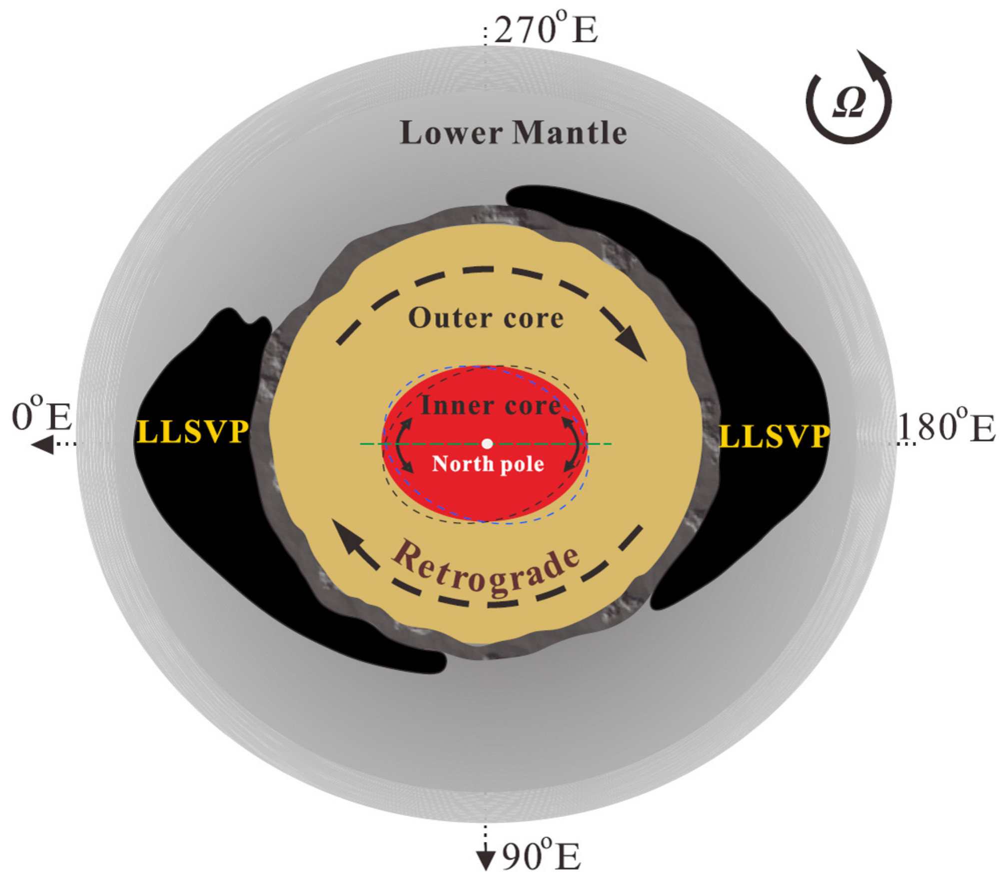

Ding and Chao (2018)

Constraining the mantle lower structure

- **Normal mode tomography:**

- Give constraints on density, but different studies arrive to different results.

- Need to use full mode coupling.

- **Core-Mantle Boundary topography:**

- Correlation between long-wavelength topography and shear-velocity anomalies Provides a potential test to decide lower mantle structure.

- Difficult to measure: trade-off between topography and adjacent velocity structures.

- **Seismic attenuation:**

- Q may be a good proxy for temperature.

- Difficult to estimate with accuracy: focusing/defocussing effects, scattering due to small scale structure.

- **Tidal tomography and Earth rotation (MICG): very promising.**

- **Electrical conductivity:**

- C-responses at long periods may discriminate between thermal and thermo-chemical models.

- Need long period (> 1year) geomagnetic data with high accuracy to build C-responses for lowermost mantle; requires long (decades) datasets.

- Involves mantle and core communities (CMB topography, electrical and thermal conductivities, MICG coupling).

Additional slides

Which structure for the Earth's mantle ?

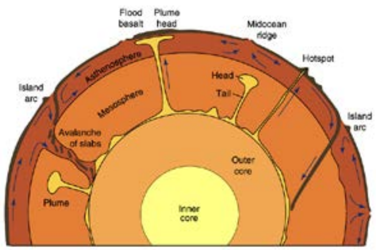

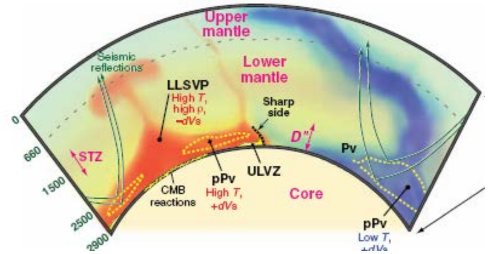

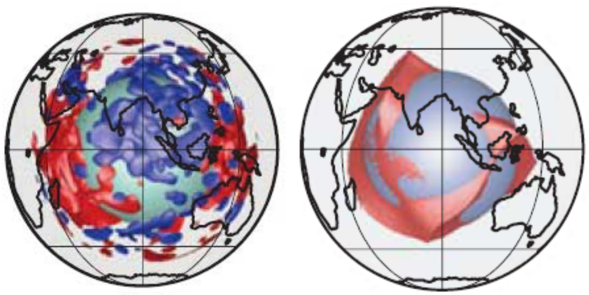

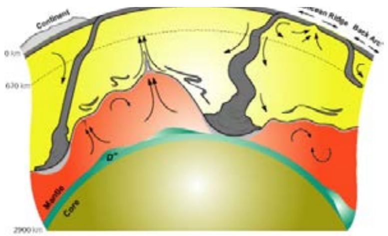

Kellogg, et al 19 MARCH 1999 VOL 283 SCIENCE

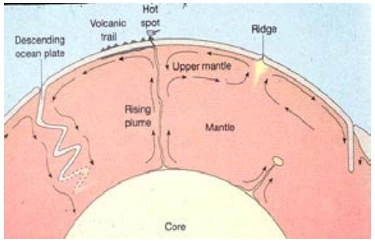

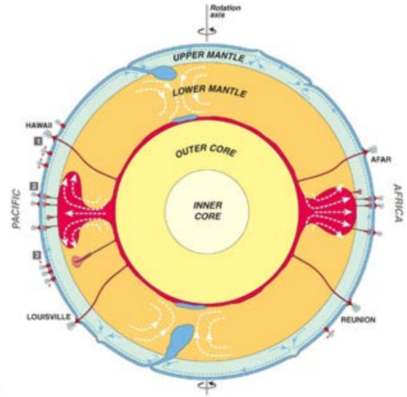

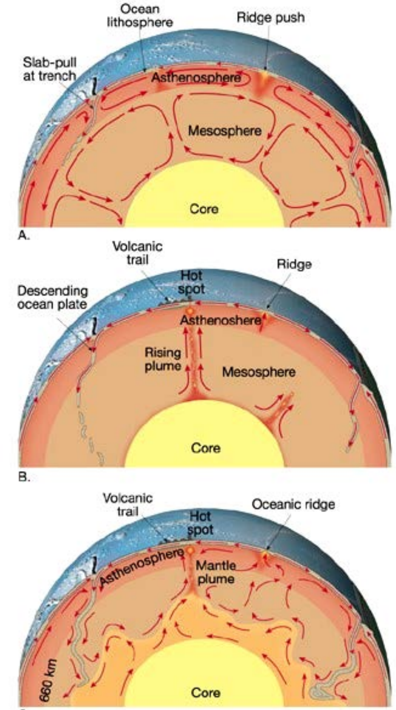

A.

B.

C.

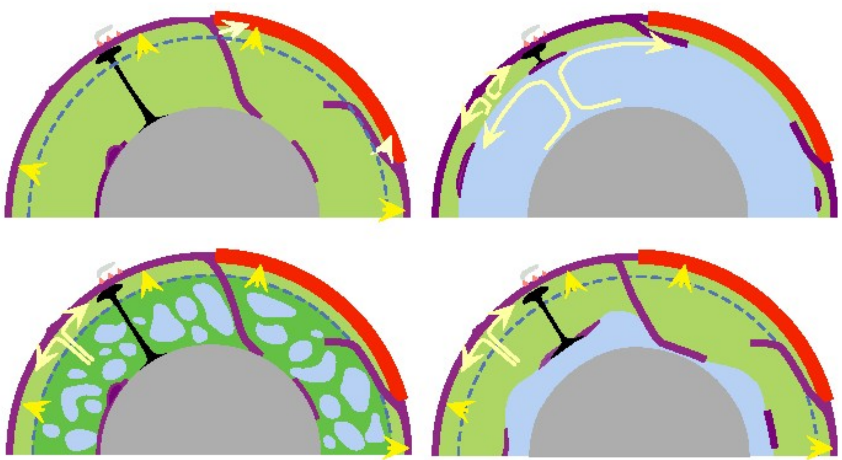

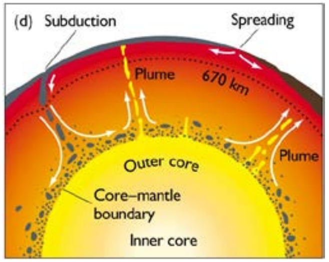

Purely thermal or thermo-chemical ?

Constraining Earth's mantle structure

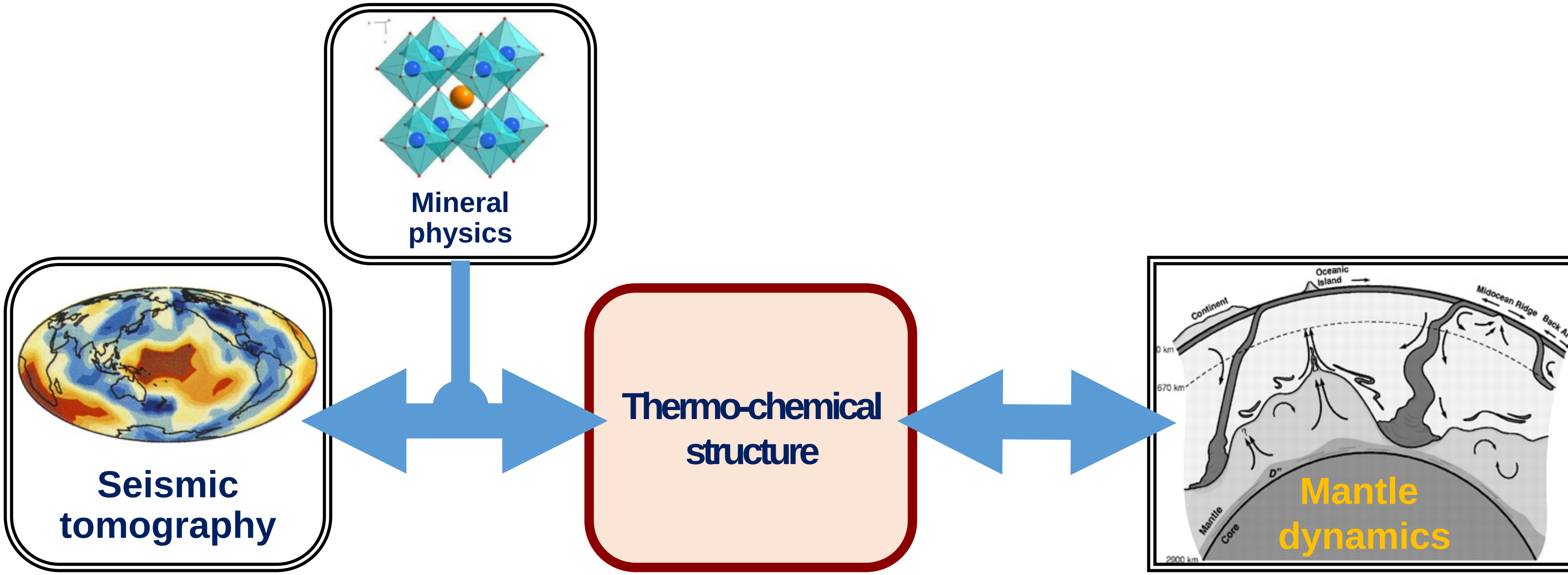

- Seismic tomography: relate seismic waveform to Earth model structure.

Requires input from mineral physics (extrapolation of rock properties at high T and P).

- Isotope geochemistry (*e.g.*, Helium ratio) : evolution of mantle structure/composition.

- Other constraints: Seismic normal modes, solid tides, core-mantle boundary topography, seismic attenuation, … ?

- Mantle dynamics: mantle flow influences thermo-chemical structure, and vice-versa

Maintaining thermo-chemical piles

Models with moderate density contrast and large thermal viscosity contrast maintain large pools of dense material, and induce strong thermal and chemical anomalies at the bottom of the shell.

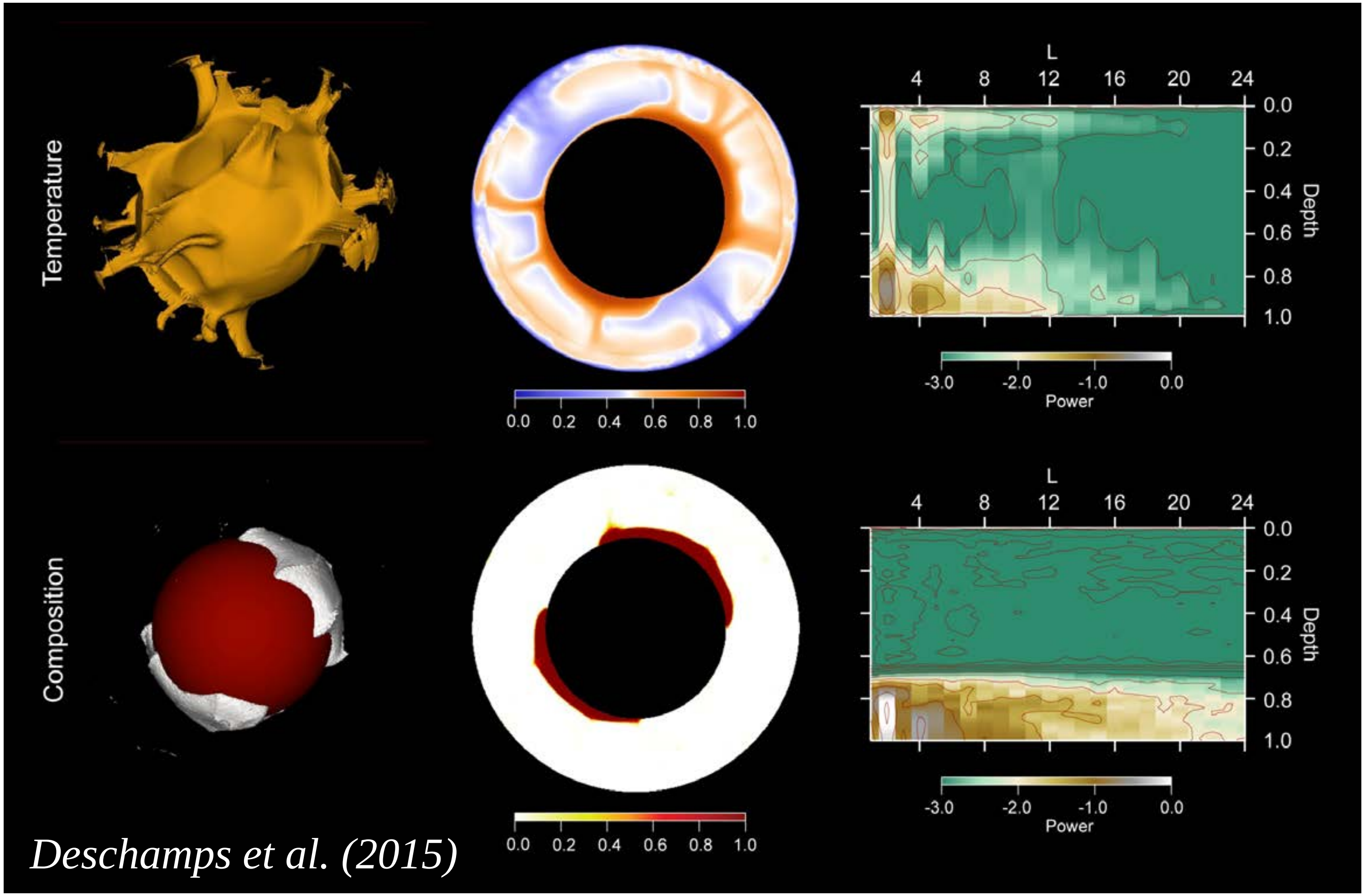

Deschamps et al. (2015)

Lower mantle: sources of chemical heterogeneities

- Two main minerals:

  - Bridgmanite, (Mg,Fe)SiO_3
  - Ferropericlase, (Mg,Fe)O

Pyrolitic (=average) mantle: ~80% pv, with x_{Fe} ~10%.

⇨ *Bridgmanite vs ferropericlase*

⇨ *Volume fraction of iron (FeO).*

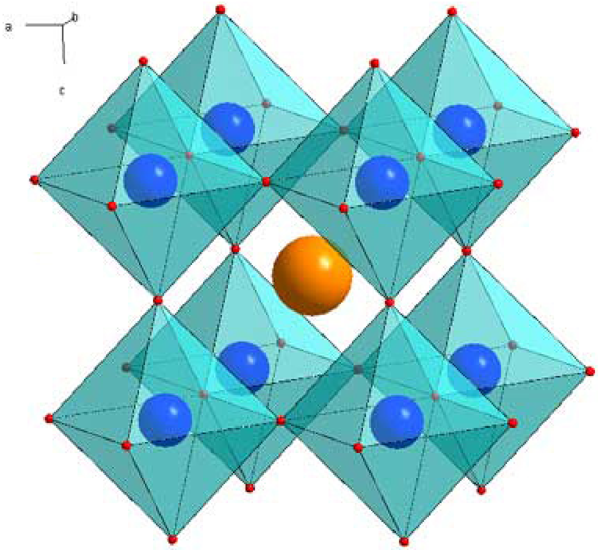

$CaTiO_3$ perovskite structure

- Recycled oceanic crust entrained with slabs.

⇨ *Volume fraction of MORBs*

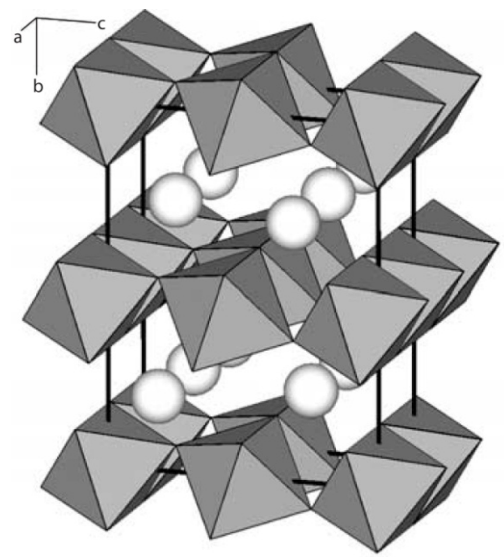

$CaTiO_3$ post-perovskite structure

- Post-perovskite (*Murakami et al., 2004*; *Oganov and Ono, 2004*). Exothermic transition around 120 GPa (and 2500 K), with large Clapeyron slope (8-10 Mpa/K).

⇨ *Lateral variations in the topography of pPv*

Equation of state modelling

- Thermo-elastic properties and density at high pressures and temperatures from thermo-elastic properties & density at $T = T_0$ and $P = 0$

- For each mineral of the aggregate:

- High temperature extrapolation:

$$\rho = \rho_0 \exp\left[-\int_{T_0}^{T_p} \alpha(T)dT\right]$$

$$K_S = K_{S0} \exp\left[\frac{\rho}{\rho_0}\right]^{\delta_S}$$

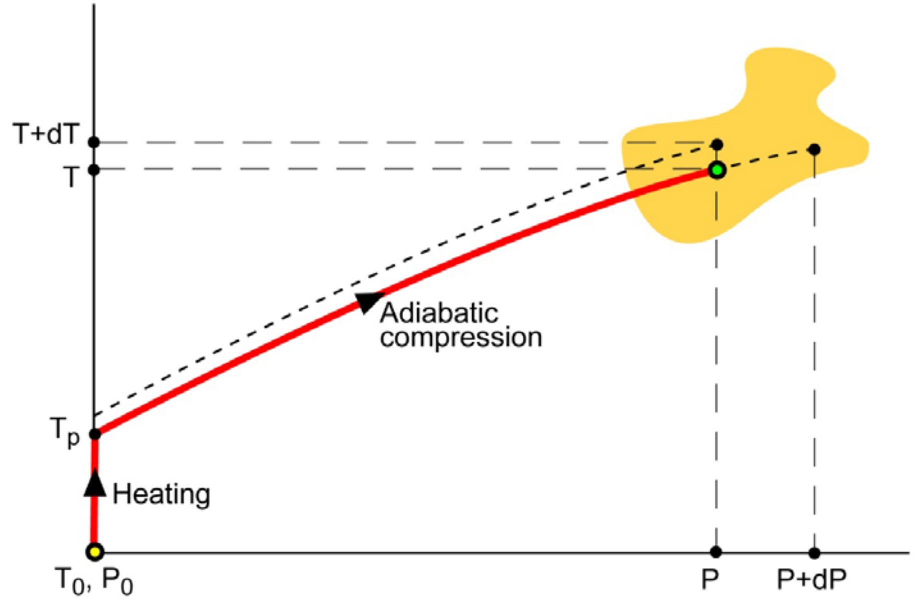

- High pressure extrapolation (Birch-Murnaghan to 3rd order):

$$P = -3K_{S0}(1-2\varepsilon)^{5/2}\left[\varepsilon + \frac{3}{2}\left(4 - K'_{S0}\right)\varepsilon^2\right]$$

$$\rho = \rho_0 (1-2\varepsilon)^{3/2}$$

$$K_S = K_{S0}(1-2\varepsilon)^{5/2}\left[1 + \frac{3}{2}\left(5 - 3K'_{S0}\right)\varepsilon - \frac{27}{2}\left(4 - K'_{S0}\right)\varepsilon^2\right]$$

- Uncertainties from error bars at $T = T_0$ and $P = 0$, and a Monte-Carlo Search.

- Thermo-elastic properties of the aggregate from Voigt-Reuss-Hill average.

Seismic sensitivities to MORB

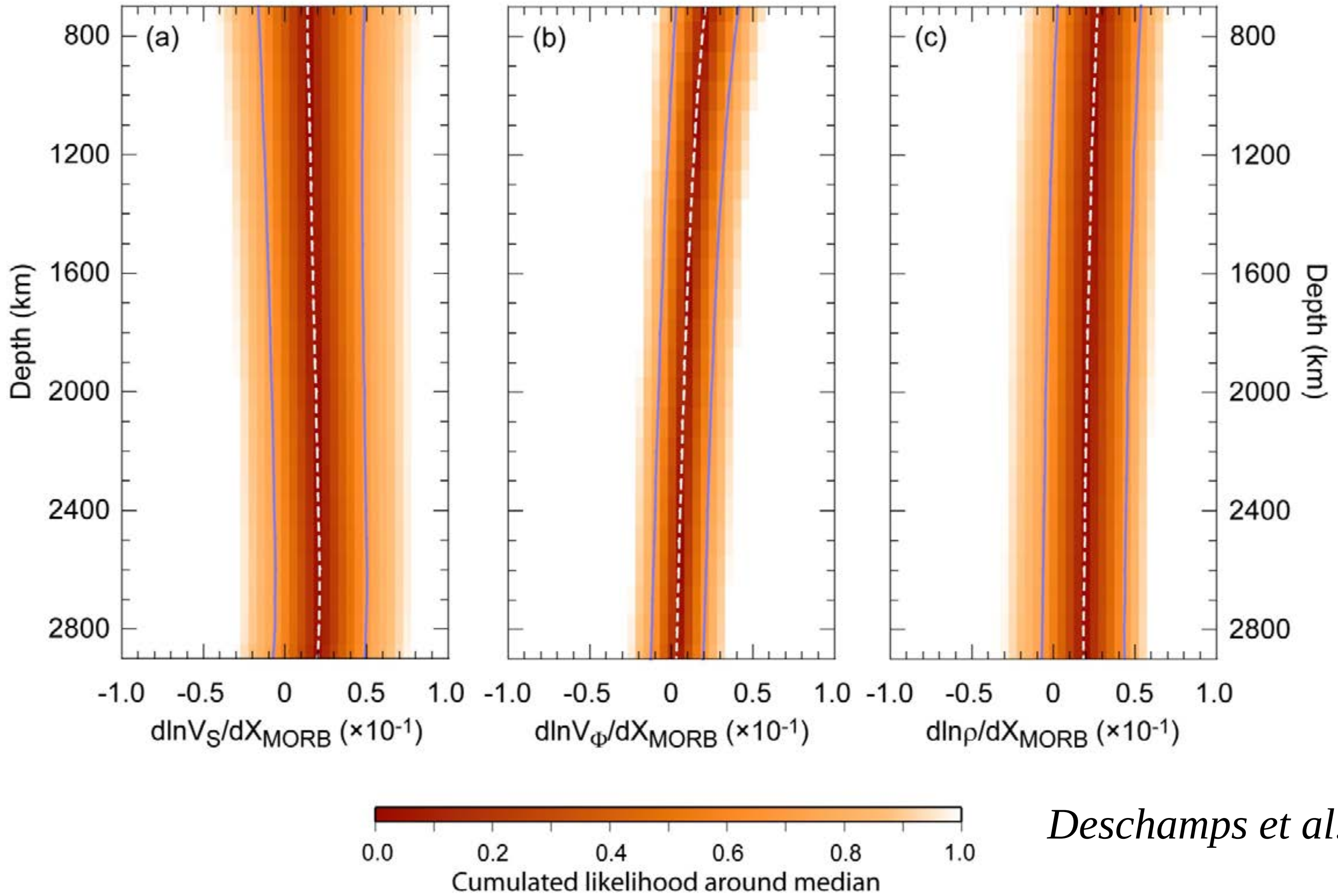

Deschamps et al. (2012)

- Sensitivity of V_S to MORB is mostly positive, *i.e.* MORB excess result in positive dlnV_S.
- Sensitivity of V_Φ to MORB is small, *i.e.* MORB has small influence on dlnV_Φ.

Seismic sensitivities to post-perovskite (pPv)

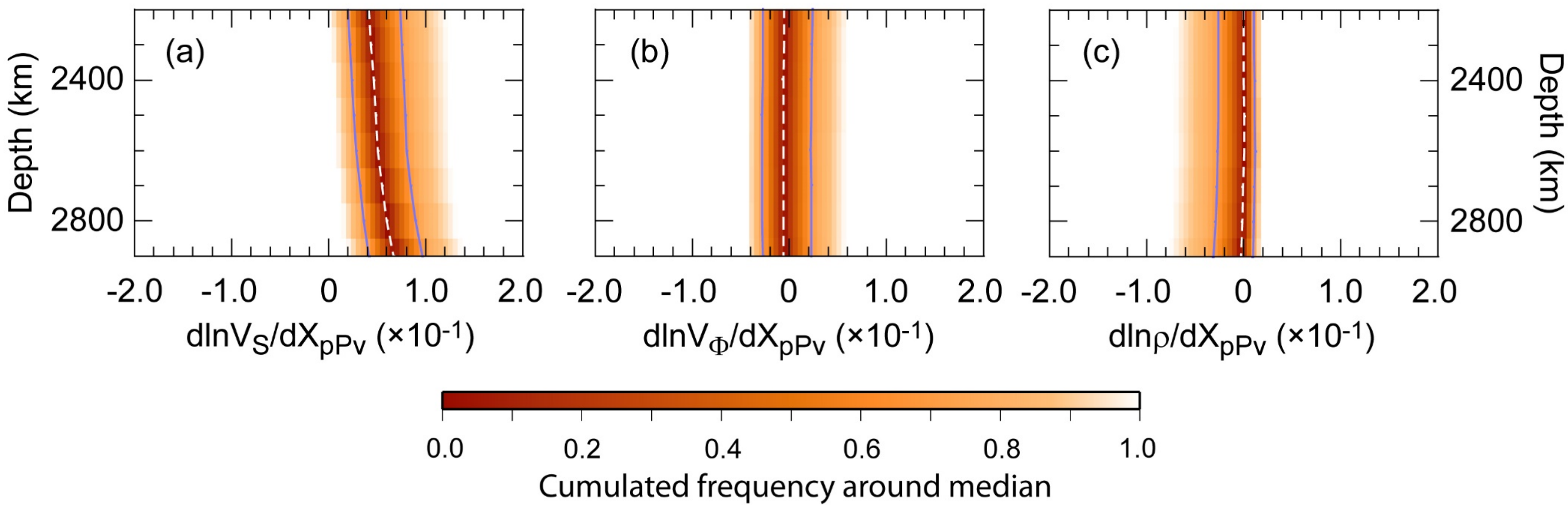

- Sensitivity of V_S to pPv is mostly positive, *i.e.* pPv excess result in positive dlnV_S. If LLSVPs are surrounded by pPv
- Sensitivity of V_Φ to pPv is very small, *i.e.* pPv leaves dlnV_Φ mostly unchanged.

Effects temperature and composition

- Shear-wave velocity:

- Decreases with increasing temperature and iron content.
- Post-perovskite: faster than bridgmanite by ~ 2.0-4.0 %.
- MORB: V_S slightly increases with temperature, but depends on exact MORB composition.

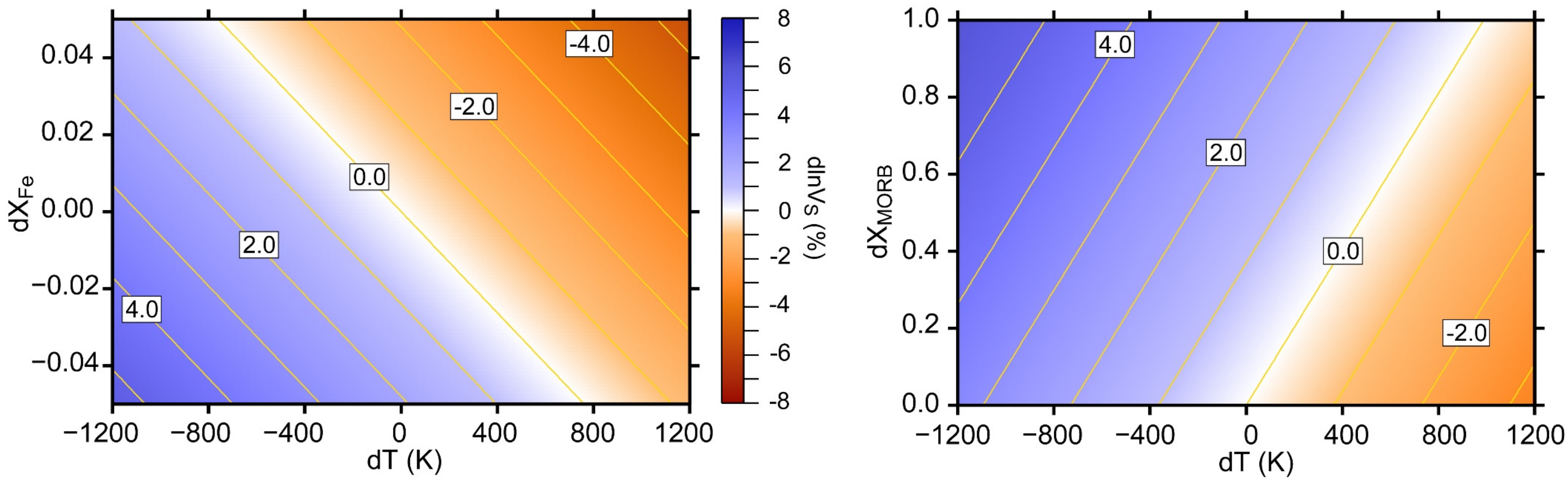

- Bulk-sound velocity and density:

- Decreases with increasing temperature but increases with and iron content.
- Post-perovskite: slighlty denser than bridgmanite ~ 1.0-2.0 %.
- MORB: denser than pyrolite; leaves V_Φ unchanged.

Seismic velocity anomalies: frequency histograms

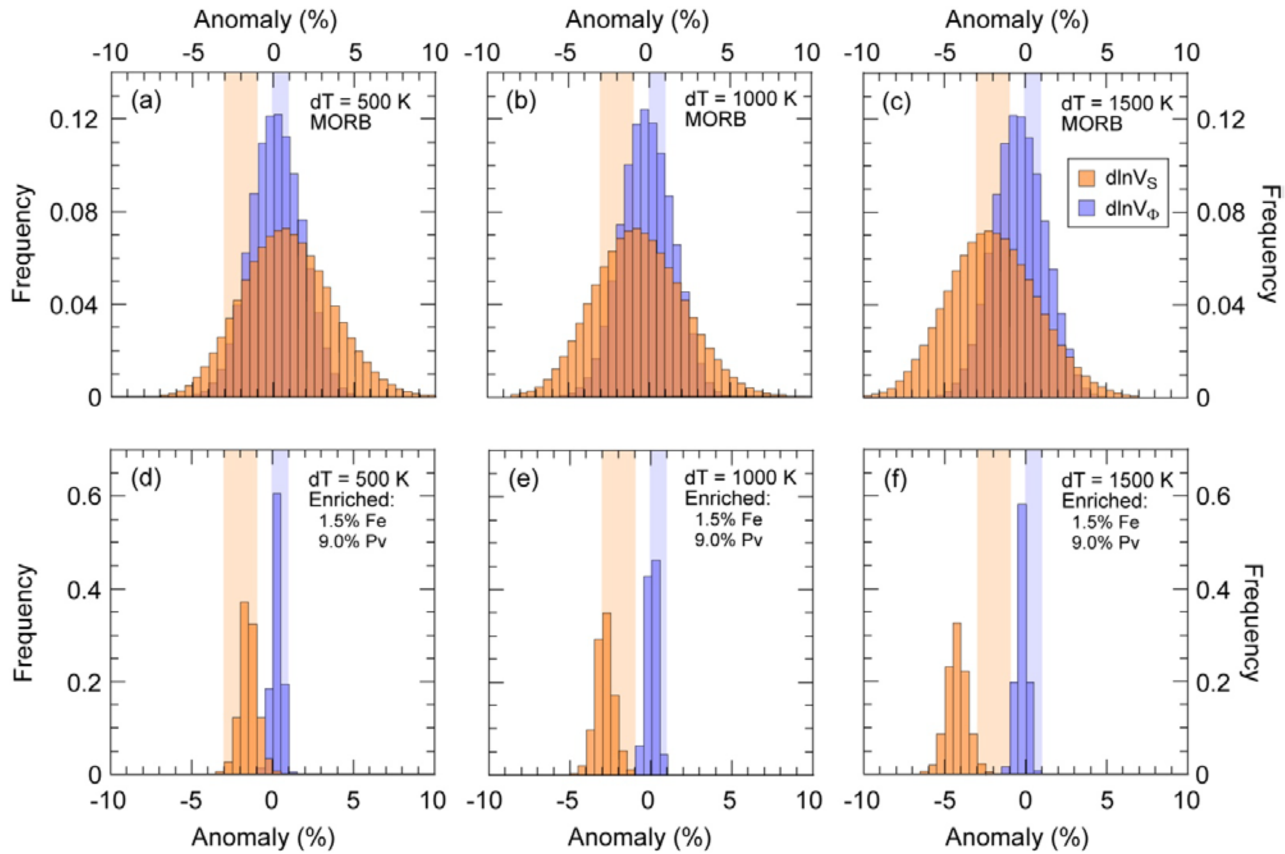

Deschamps et al. (2012)

- MORB: strong dispersion and need high temperature anomalies to explain seismic anomalies observed in the deep mantle.

- Material enriched in Iron + perovskite: fit seismic anomalies for temperature anomalies in the range 400-800 K.

Temperature anomalies: likelyhoods

- Probability that seismic velocity is within a prescribed range of value, given composition and a temperature anomalies.

Typical values of velocity anomalies in LLSVP:

$-3.0 < d\ln V_S < -1.0$ % and $0.0 < d\ln V_\Phi < 1.0$%

- Iron + silicate rich material: explain well velocity anomalies in values observed in LLSVP for temperature anomalies in the range 400-800 K.

- MORB: poor fit to LLSVP values and need high (> 1000 K) temperature anomalies.

- Presence of pPv leads to similar conclusions.

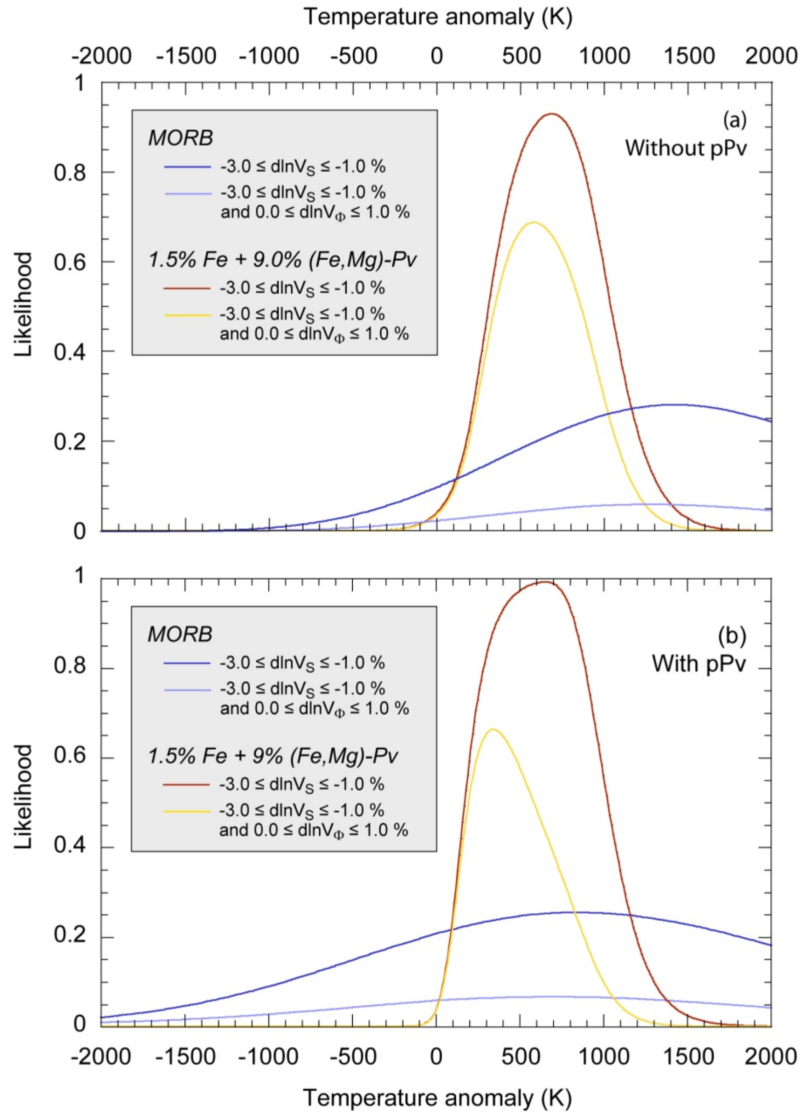

Deschamps et al. (2012)

Stoneley modes

- Stoneley modes are sensitive to lowermost mantle, … but also to top of outer core.

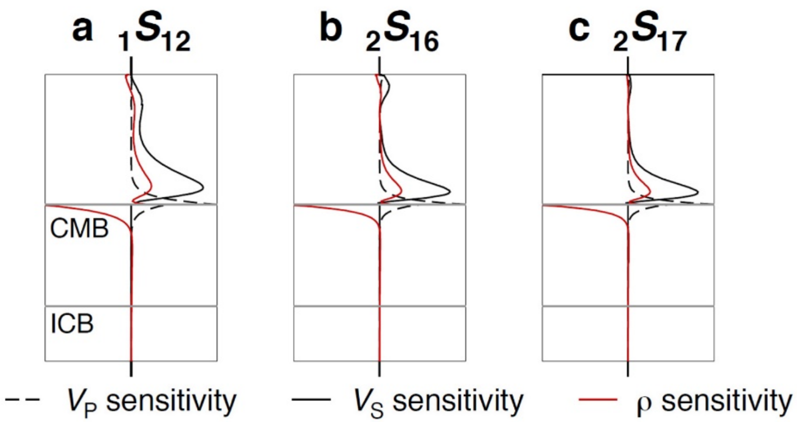

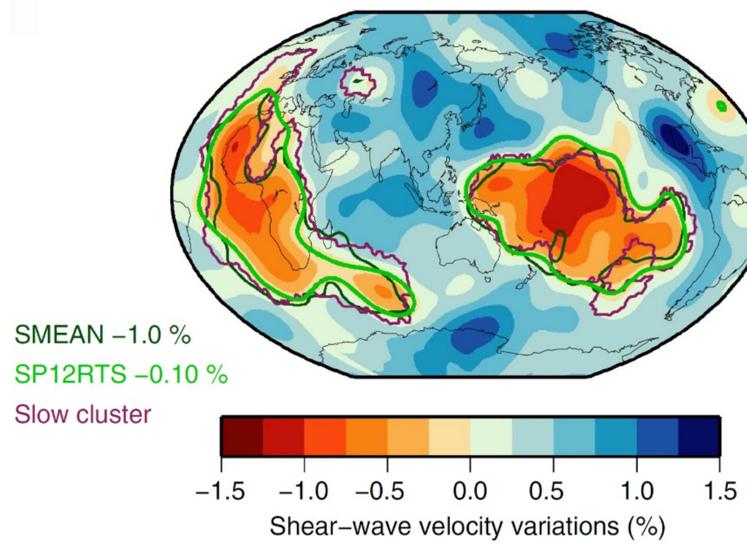

- Koelemeijer et al. (2017):

- Test possible density models against Stoneley mode splitting measurements.

- Define different density LLSVP (LL) and surrounding regions (SR) …

- … and impose different values for $R = d\ln\rho/d\ln V_S$:

$R_{LL} < 0$: dense LLSVP; $R_{LL} > 0$ light LLSVP.

- Account for CMB topography with scaling $H = d\ln h_{CMB}/d\ln\rho$.

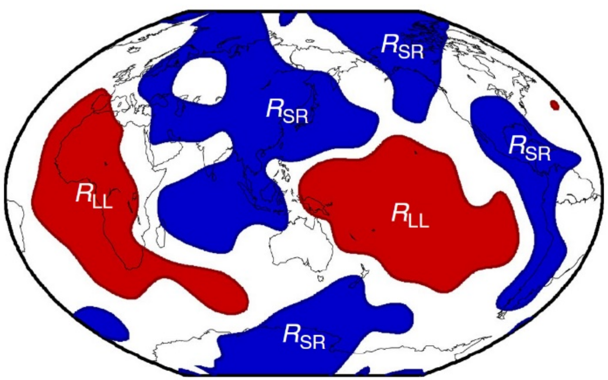

Stoneley modes prefer light LLSVP

- Stoneley modes are better explained by light LLSVPs:

- Best fit ~ 0.57 for degree 2 models.

- Preference less pronounced if modes up to degree 8 are accounted for.

- No preference if other modes are added to Stoneley mode.

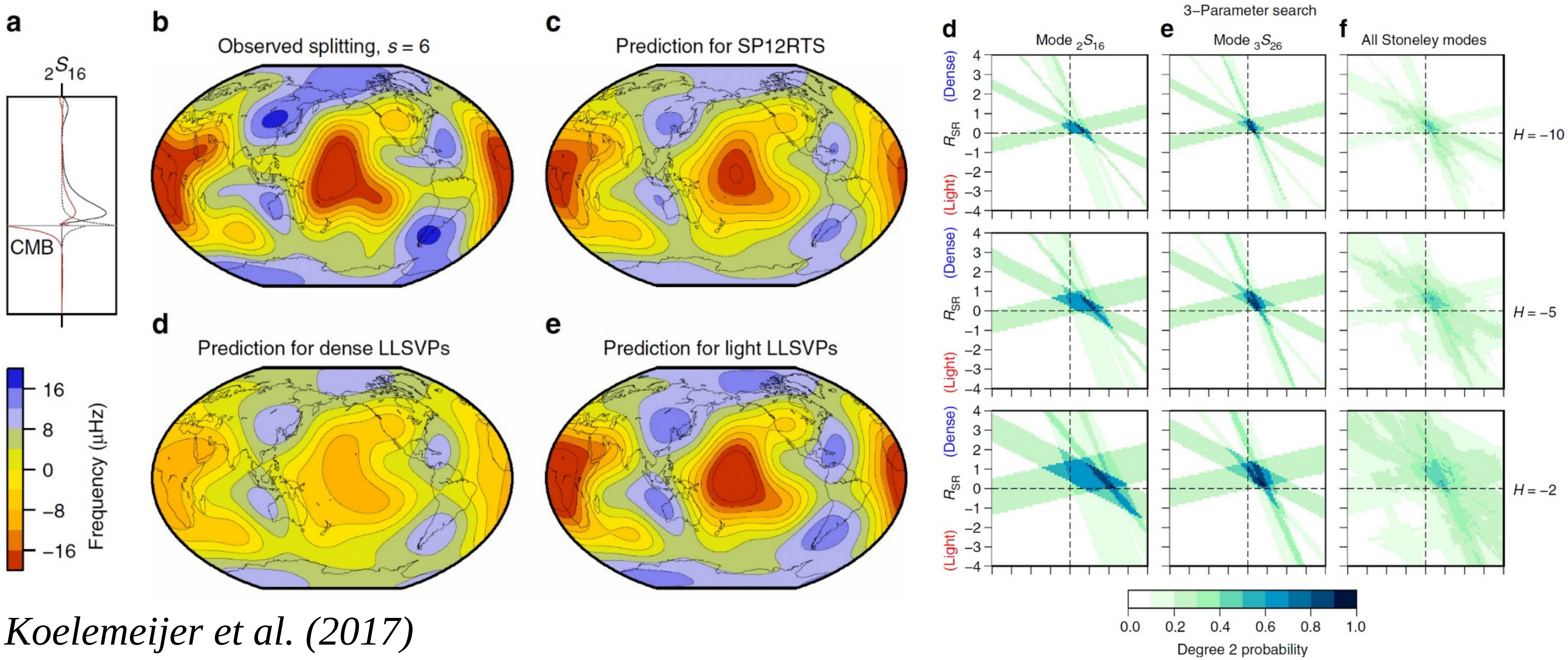

Koelemeijer et al. (2017)

Unconstrained density/shear-velocity scalings

Moulik and Ekström (2016): LLSVPs appear denser than surrounding mantle (ρ/V_S is larger than average)

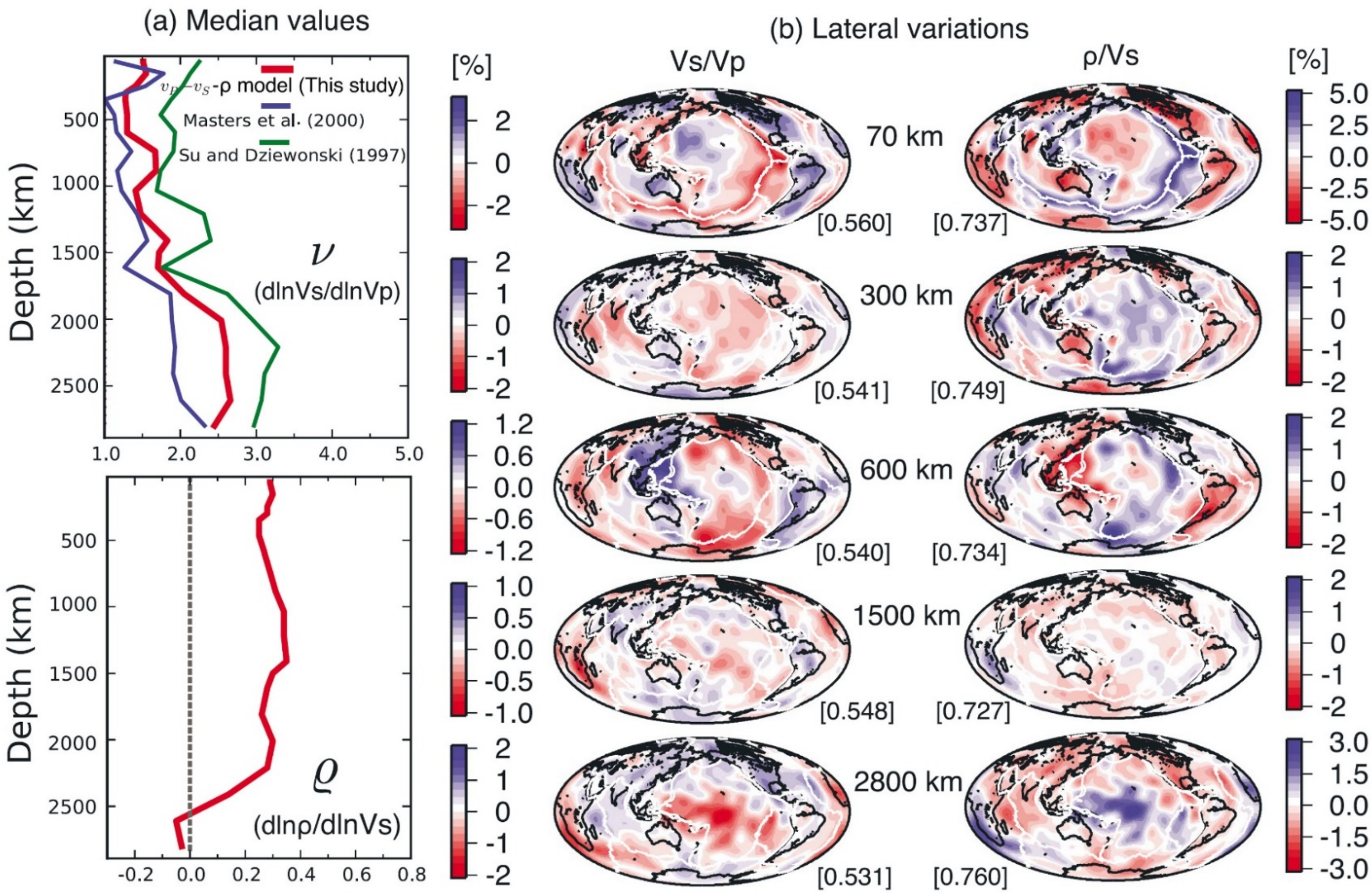

Moulik and Ekström (2016)

Thermo-chemical structure from seismic observables

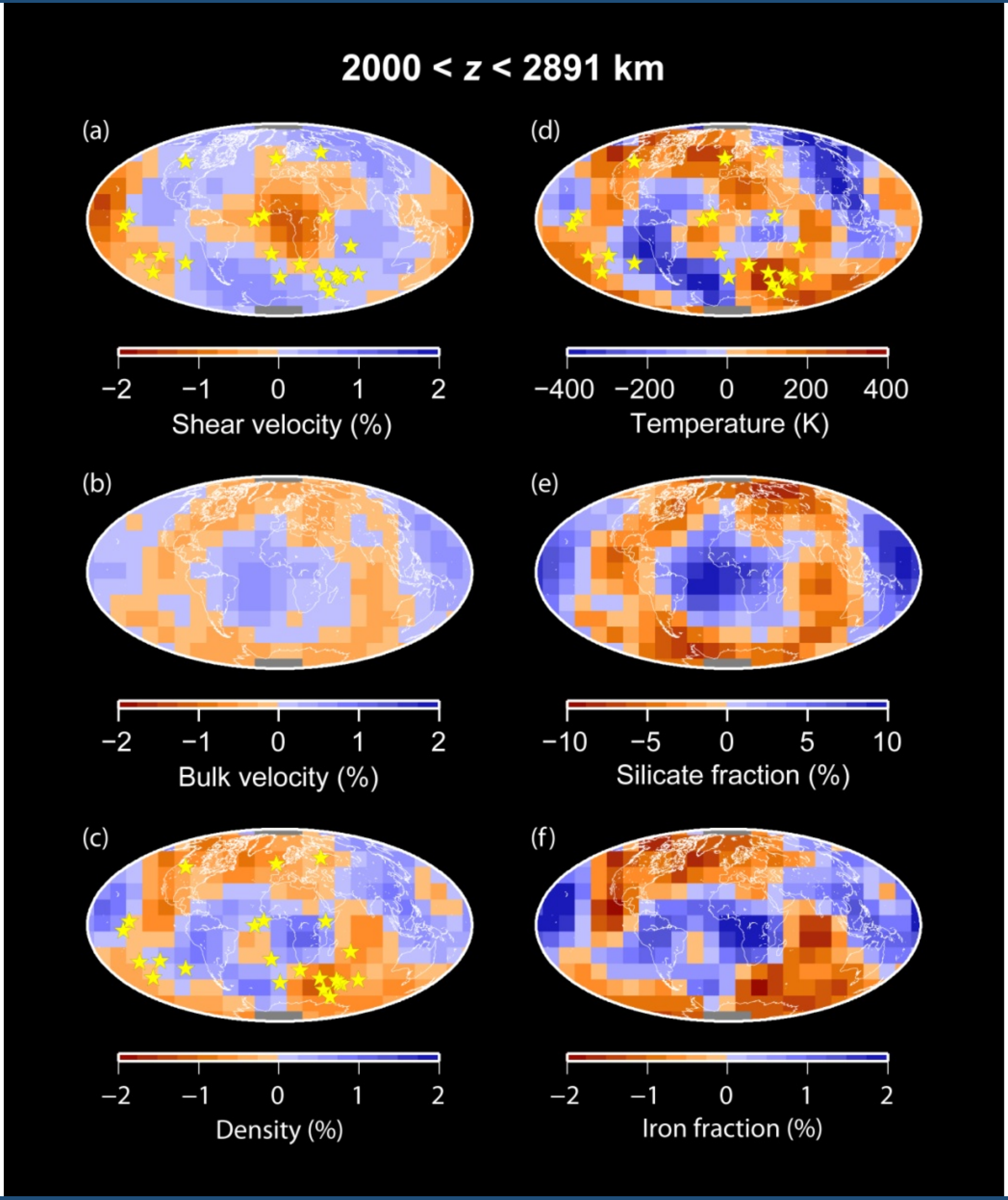

Plumes: recent global seismic observations

- **SEMUCB-WM1 (French and Romanowicz, 2015):**

- Inversion of long-period body and surface waveform + wavefield modelling (spectral method).

- Image broad plumes (500-800 km in diameter) connecting CMB and surface.

- 11 well resolved plumes (consistent with primary plumes in Courtillot et al.)

- 3 rooted at or near known ULVZ (Iceland, Samoa, Hawaï).

- Broad plumes: indication of thermo-chemical plumes (*e.g.*, Lin and van Keken, 2006).

- Shear-velocity anomalies is plume ~ 1.5 %, lead to temperature excess ~ 500 K: large compared to petrological and geochemical estimates, ~200-300 K (Schilling, 1990)

- Absence of thin plumes: due to resolution of data and method ?

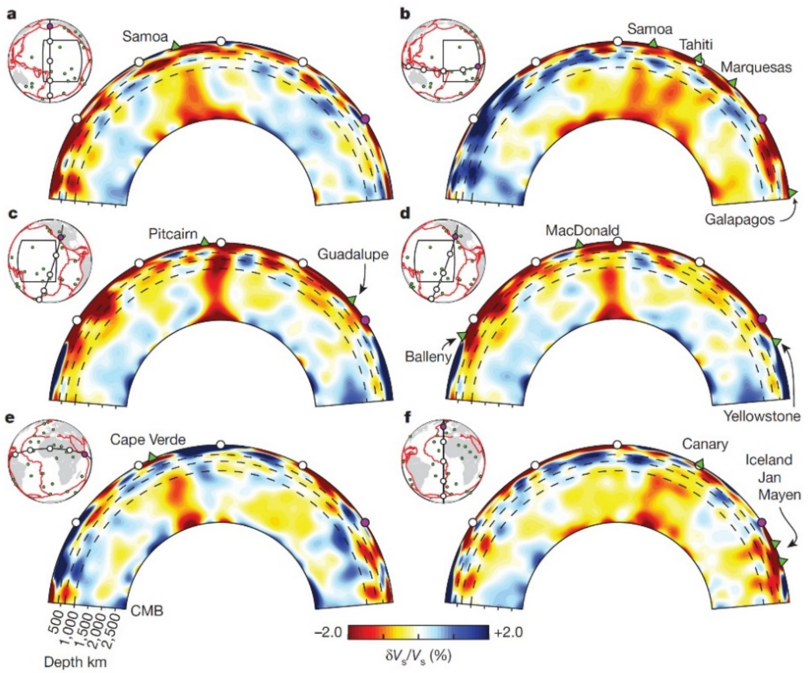

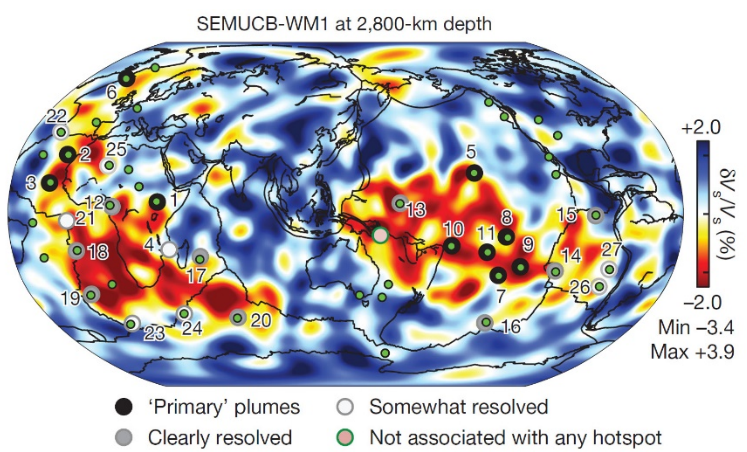

Stable LLSVPs: LLSVPs and LIPs positions

- Paleomagnetic reconstructions of LIP locations (*e.g.*, Torsvik et al., 2010): most (but not all) plumes originating from the dense reservoirs are generated at the edges of these reservoirs.

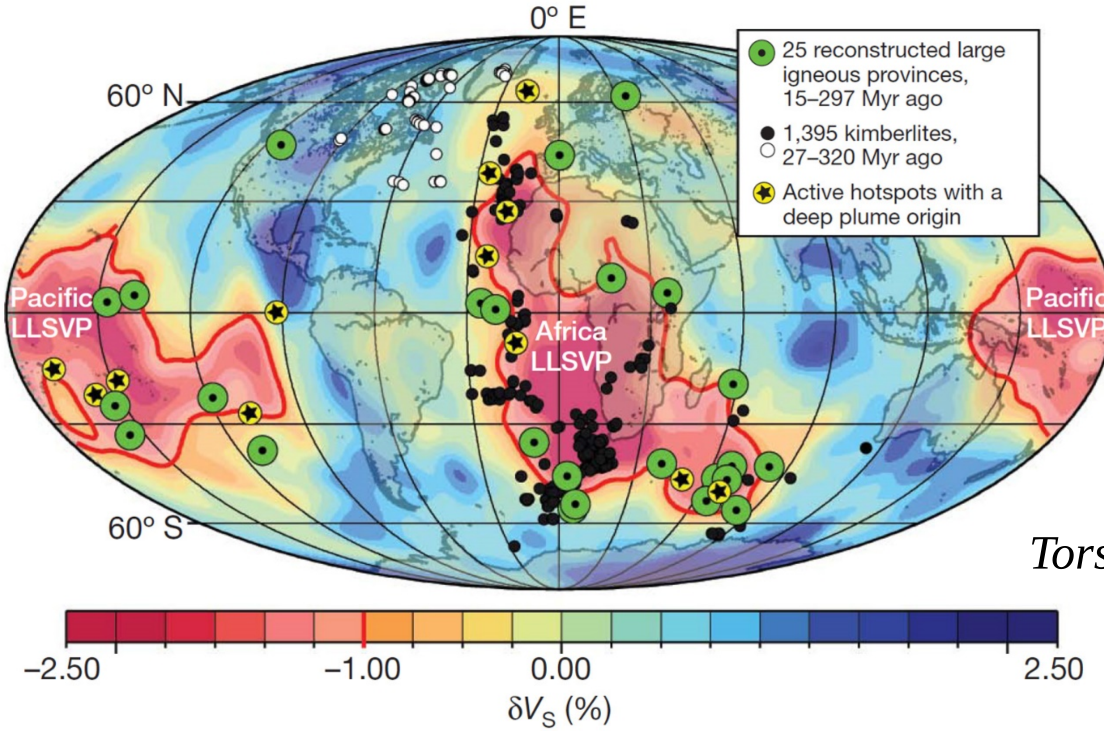

Torsvik et al.(2010)

- Austerman et al. (2014): correlation between LIP and LLSVP margins not significant. Observations also consistant with plumes originating from LLSVP interiors.

- If LIP plumes are generated in LLSVPs, these structures remained stable for at least 200-300 Myr (Torsvik et al., 2008).

Stable LLSVPs: implication on thermo-chemical structure

- Plumes remain stable (same position) for few 10s on Myr:

Difficult to maintain plume clusters around same geographical region for 300 Myr and more.

- Piles/reservoirs of dense material can remain stable on Gyr:

Plumes change location with time, but remain rooted at the top of reservoirs, maintaining plumes around same geographical region for long periods of time.

CMB topography: influence from various parameters

- Dynamic topography calculated from the normal stress at the CMB, and accounts for self-gravitational effects:

$$h_{\mathrm{CMB}} = \frac{\sigma_{zz} + \Phi_{\mathrm{CMB}} \Delta\rho_{\mathrm{CMB}}}{\Delta\rho_{\mathrm{CMB}}\, g}$$

- Chemical density contrast ($\Delta\rho_C$): topography beneath piles is flat for low $\Delta\rho_C$, and depression increases with increasing $\Delta\rho_C$ (Lassak et al., 2010; Deschamps et al. 2018): *normal stress increases with $\Delta\rho_C$, and density contrast between core and mantle decreases*.

- Thermal viscosity contrast ($\Delta\eta_T$): amplitude of topography decreases with increasing $\Delta\eta_T$ (Lassak et al., 2010; Deschamps et al. 2018): *plumes/piles are hotter, thus less viscous, which reduces the normal stress at CMB beneath plumes*.

- Chemical viscosity contrast ($\Delta\eta_C$): amplitude of topography beneath piles decreases with decreasing $\Delta\eta_C$ (Deschamps et al. 2018).

- Presence of post-perovskite: does not substantially modify the topographic pattern and amplitude, as long as pPv and bridgmanite have similar viscosity (Deschamps et al. 2018).

CMB topography from numerical simulations

- Topography from purely thermal and thermo-chemical ($\Delta\rho_C$ = 60 kg/m^3) models (Lassak et al., 2010):

- Purely thermal: upwellings induce ridges

- Thermo-chemical piles induce flat topography surrounded by ridges.

- Long-wavelengths (l = 0-4) filter:

- Thermal and thermo-chemical cases almost similar: positive topography.

- Tomography and V_S anti-correlated

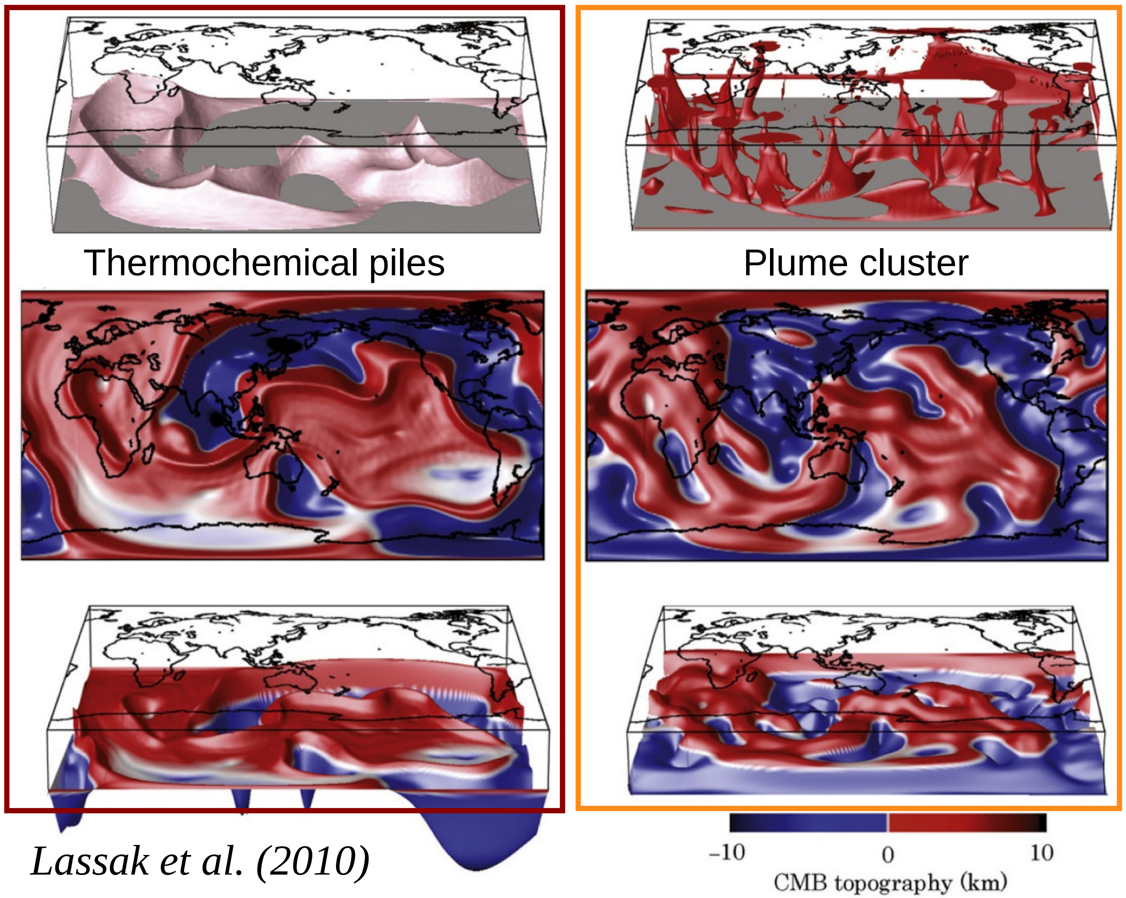

Lassak et al. (2010)

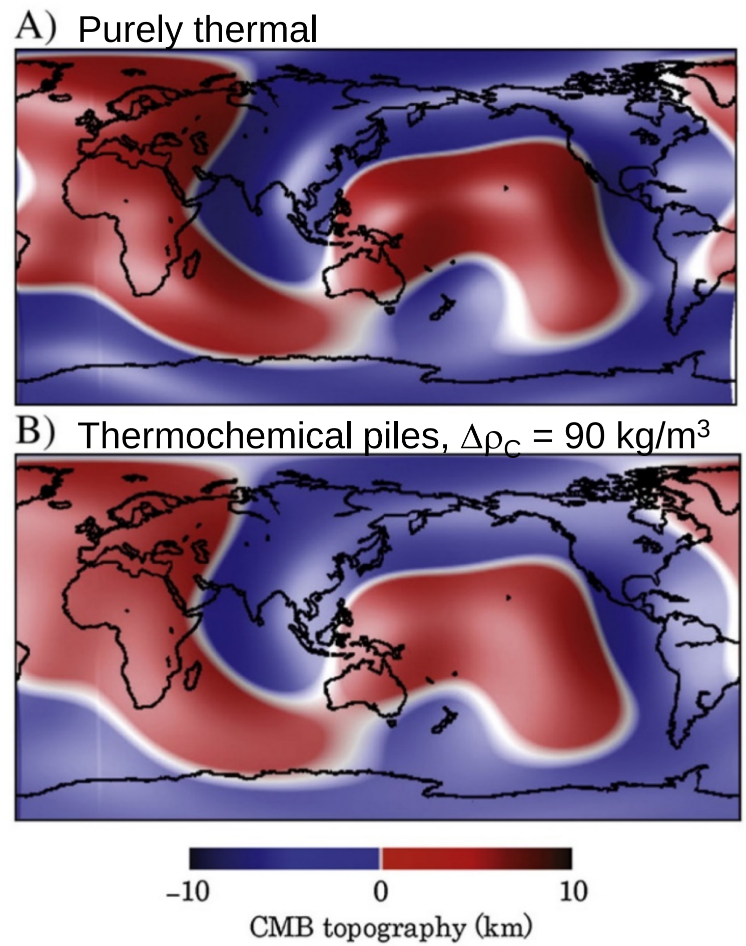

Influence of chemical density and viscosity contrasts

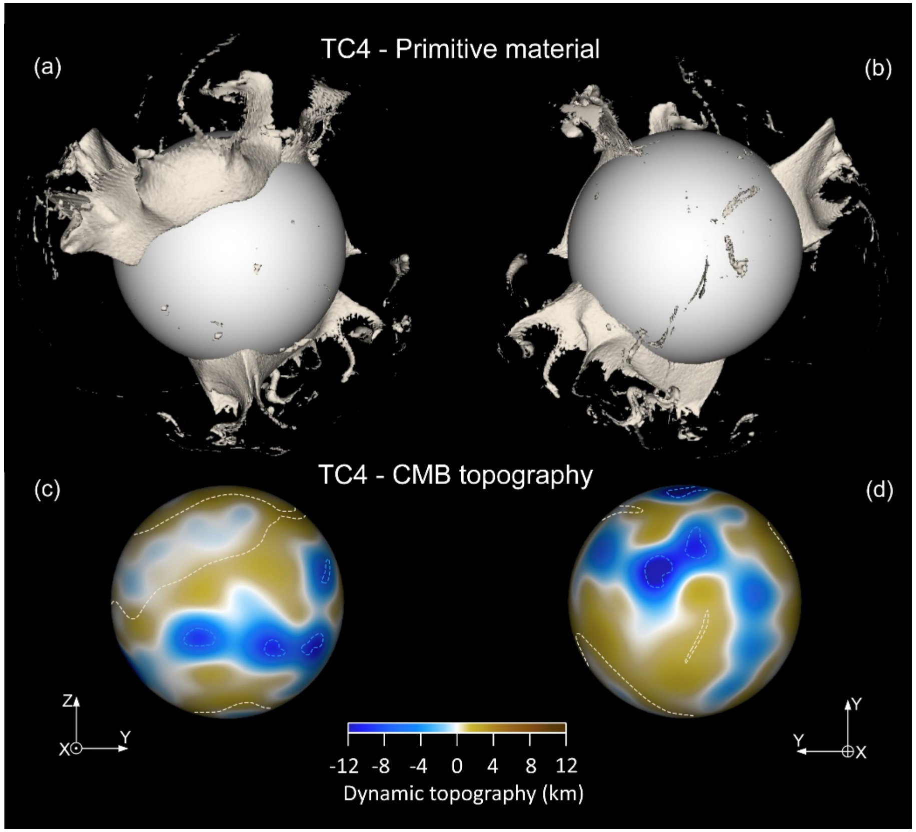

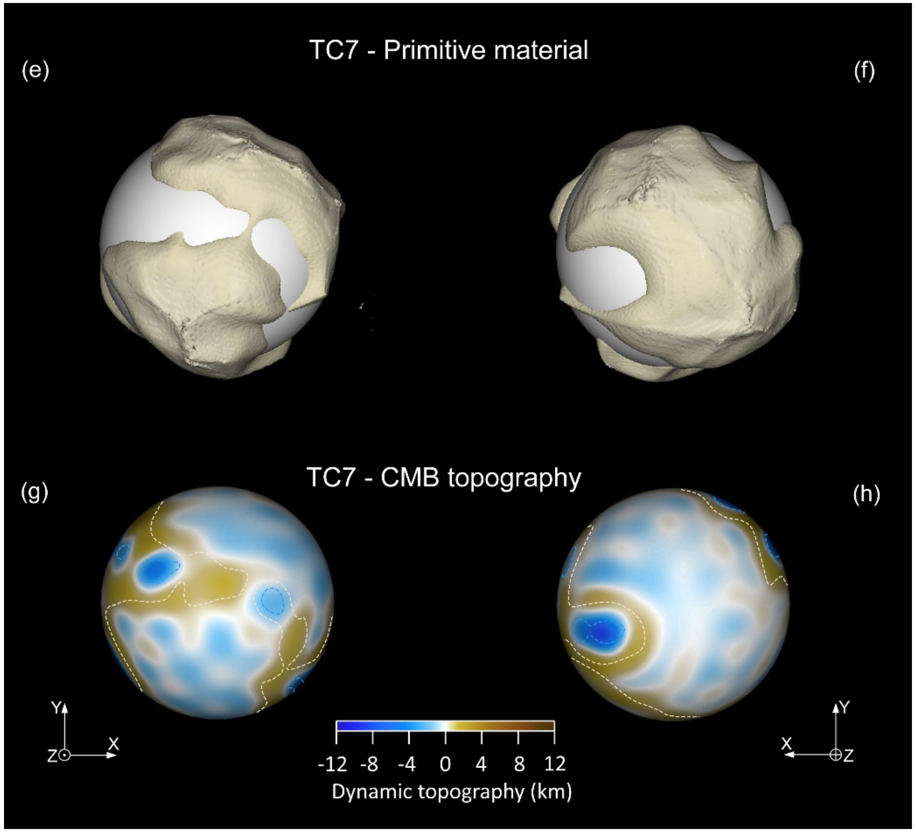

- Chemical density contrast (buoyancy ratio)

Amplitude of topography beneath piles decreases with decreasing density contrast.

For with B = 0.15 ($\Delta\rho_C$ = 90 kg/m^3), piles of dense material induce depression ~ 0.6 km.

- Chemical viscosity contrast ($\Delta\eta_C$)

Amplitude of topography beneath reservoirs decreases with decreasing $\Delta\eta_C$.

For $\Delta\eta_C$ = 1, reservoirs of dense material induce ~ 0.7 km deep.

Hints from geochemistry

- Helium isotope ratio $^4He/^3He$ shows large dispersion (15000-200000) in Ocean Island Basalts (OIB).

- Small values sample primitive (undegassed) reservoir.

- Large values sample recycled oceanic crust.

- Incompatible elements:

- OIB are globally richer in incompatible elements, but also show a large dispersion.

- Sr, Nd, and Hf: OIB may partly result from recycled early crust.

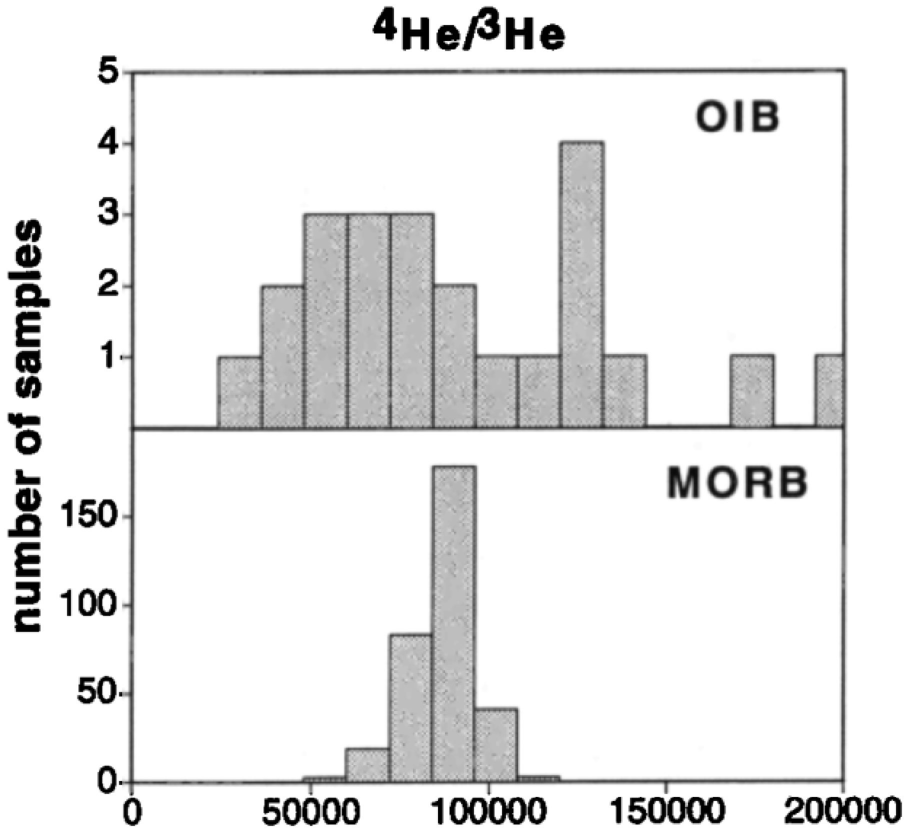

Allègre et al. (1995)

Ocean Island basalts sample several reservoirs including undegassed reservoir(s) and recycled crust

Fraction of entrained material: constraint from He ratio

- values of the helium ratio give a constraint on the fraction of primitive material entrained by plumes (x_{PM}) :

– $^4He/^3He$ in primitive reservoir should be smaller than the smallest value observed in plumes (~ 14000).

– Mass balance calculation:

$$\left[\frac{^4\mathrm{He}}{^3\mathrm{He}}\right]_{\mathrm{plumes}} = \alpha \left[\frac{^4\mathrm{He}}{^3\mathrm{He}}\right]_{\mathrm{PM}} + (1-\alpha)\left[\frac{^4\mathrm{He}}{^3\mathrm{He}}\right]_{\mathrm{RM}}$$

$$\alpha = \frac{x_{\mathrm{PM}} R_{\mathrm{He}}}{1 + x_{\mathrm{PM}}(R_{\mathrm{He}} - 1)}$$

$$R_{\mathrm{He}} = \frac{[^3\mathrm{He}]_{\mathrm{PM}}}{[^3\mathrm{He}]_{\mathrm{RM}}}$$

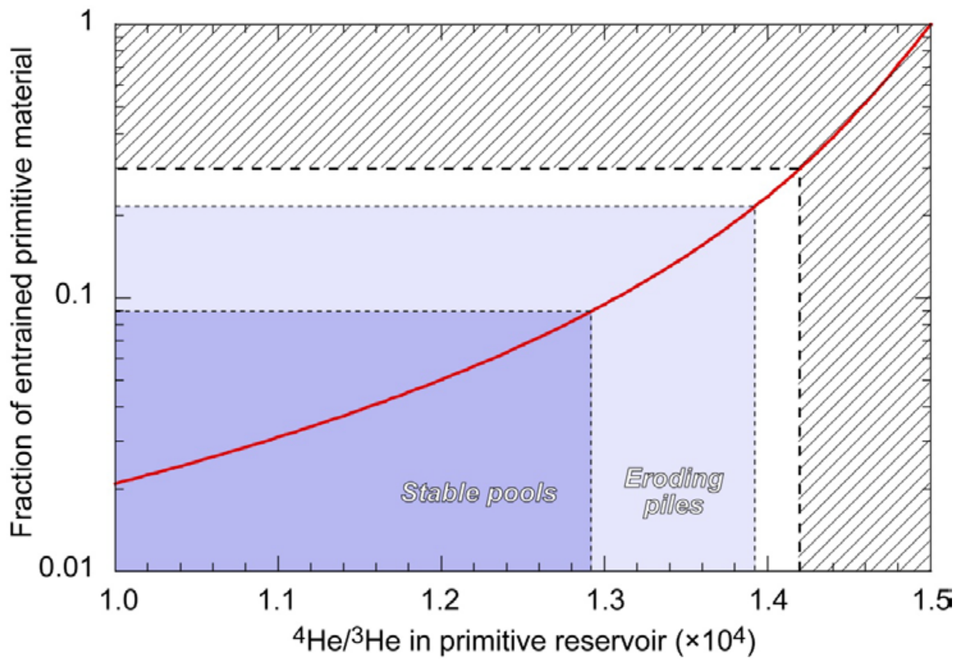

Fraction of primitive material entrained in plumes (x_{PM}) should be around 10% or less.

Fraction of entrained primitive material: models

- Plumes are generated at the top of thermo-chemical piles and entrain small fractions of dense material.
- For (meta-)stable piles entrainment is less than 10%.

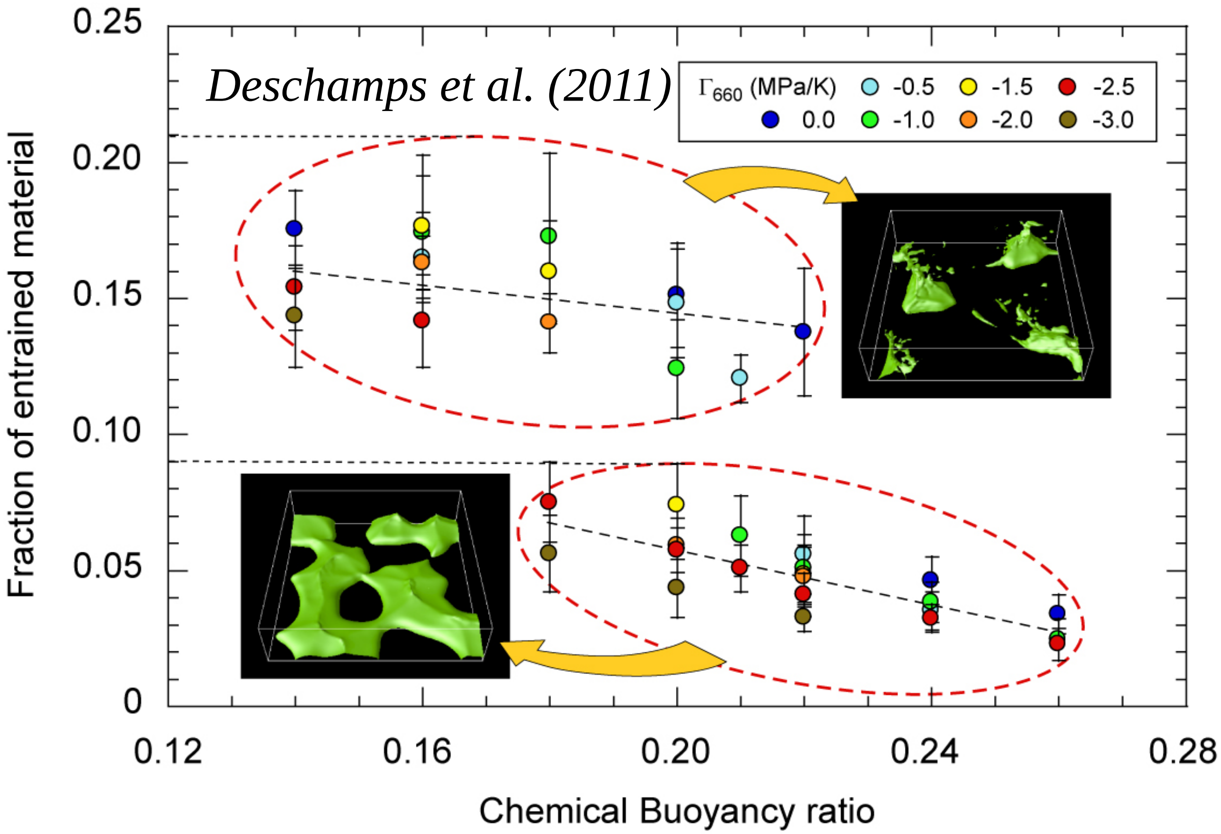

Consistent with geochemical estimates of entrainment in OIB

Entrainment of recycled and primitive materials

- Li et al. (2014) : models of thermo-chemical convection with both recycled (MORB) and primordial material :

- Recycled material is partially incorporated in primordial reservoirs, and partially re-entrained upwards.

- Plumes at top of primordial reservoirs entrain both primordial and recycled material.

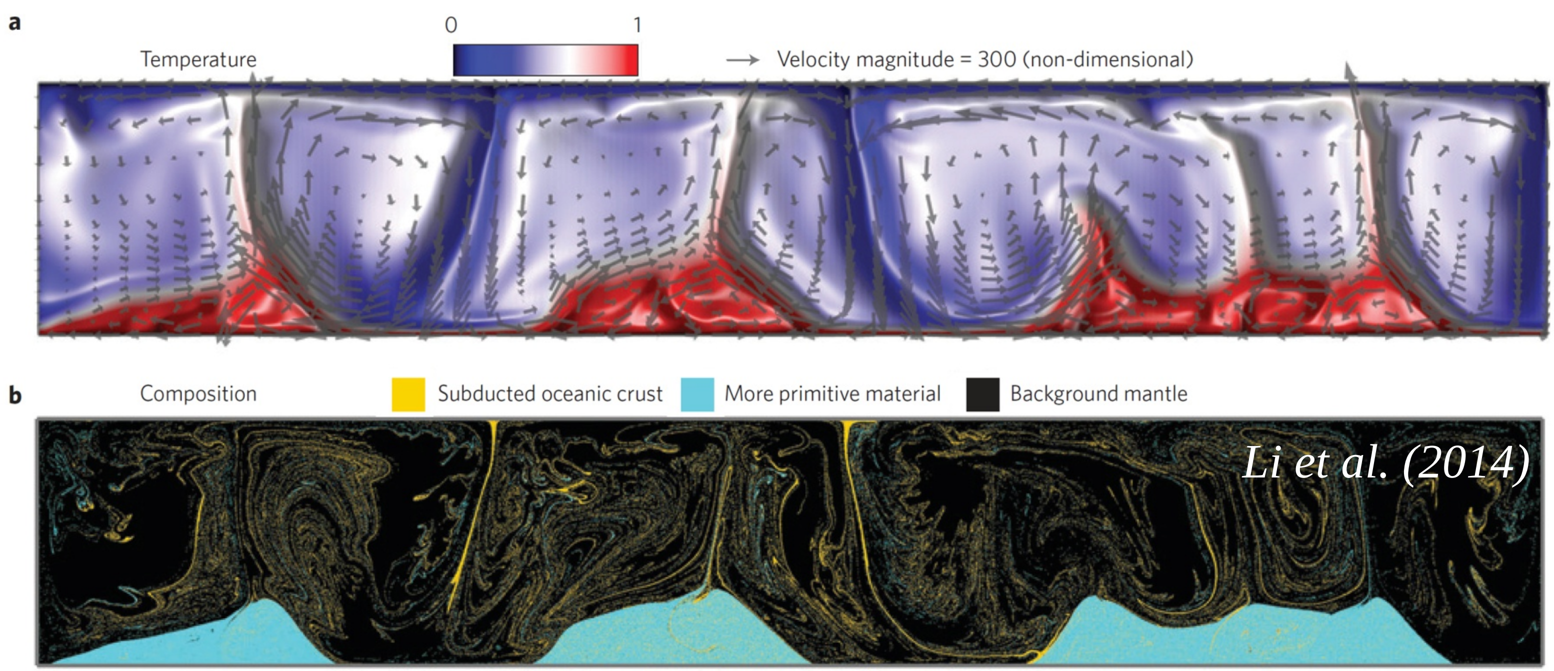

Qualitatively explain the large dispersion of helium isotopic ratio in OIB

Electrical conductivity

- Can be inferred from long-period variations of the geomagnetic field.

- Mineral physics data available (but sparse) for lower mantle minerals.

- Electrical conductivity of mantle materials depends on pressure, temperature, and composition (iron and silicate content, water content).

Increases with pressure, iron content, and temperature (unlike other properties, *e.g.* density and seismic velocities).

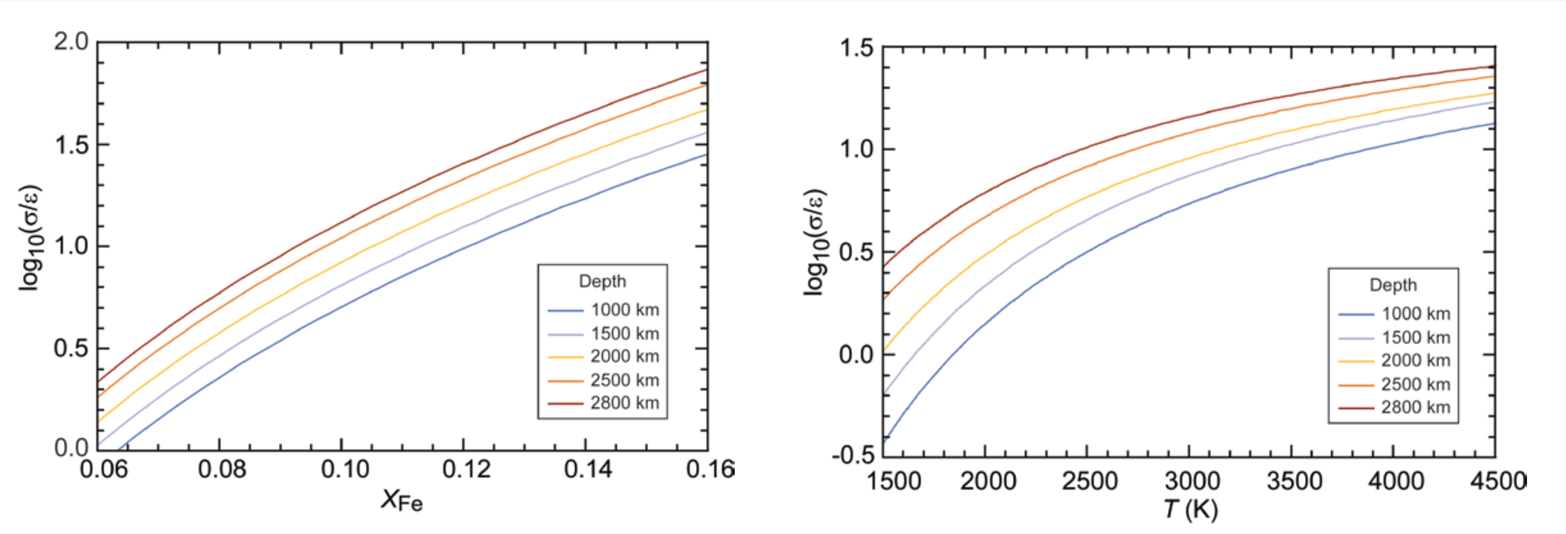

Potentially give constraints on lower mantle thermo-chemical structure

Electrical conductivity modelling

- For each mineral (here bridgmanite and ferro-pericalse), conductivity may be calculated as a function of pressure, temperature, and iron content :

$$\sigma_i = \sigma_0^i \left(\frac{x_{Fe}^i}{x_{ref}^i}\right)^{\alpha} \exp\left[-\frac{E_a^i+\beta\left(x_{Fe}^i - x_{ref}^i\right)+PV_a^i}{kT}\right]$$

- Mantle aggregate conductivity : prescribe Bm fraction (X_{Bm}) and chose average scheme :

- Conductivity for the mineral assemblage should fit with Hashin-Shtrikman bounds :

$$\sigma_{HS-} = \sigma_{Bm}\left[1+\frac{(1-X_{Bm})(\sigma_{Fp}-\sigma_{Bm})}{\sigma_{Bm}+X_{Bm}(\sigma_{Fp}-\sigma_{Bm})/3}\right] \quad \textit{and} \quad \sigma_{HS+} = \sigma_{Fp}\left[1-\frac{X_{Bm}(\sigma_{Fp}-\sigma_{Bm})}{\sigma_{Fp}-(1-X_{Bm})(\sigma_{Fp}-\sigma_{Bm})/3}\right]$$

- Average schemes : geometric, Voigt-Reuss-Hill, effective medium theory (Landauer, 1952), geometric average of HS bounds.

- Prescribe iron partitioning between Bm and Fp (K_D) and global iron fraction (X_{Fe}) :

$$K_D = \frac{x_{Fe}^{Bm}/(1-x_{Fe}^{Bm})}{x_{Fe}^{Fp}/\left(1-x_{Fe}^{Fp}\right)} \qquad \textit{and} \qquad X_{Fe} = X_{Bm}x_{Fe}^{Bm} + (1-X_{Bm})x_{Fe}^{Fp}$$

Application to transition zone

- Grayver et al. (2017): inversion of Swarm and CHAMP data for radial profiles of conductivity: compatible with conductivity for hydrated pyrolitic material in transition zone.

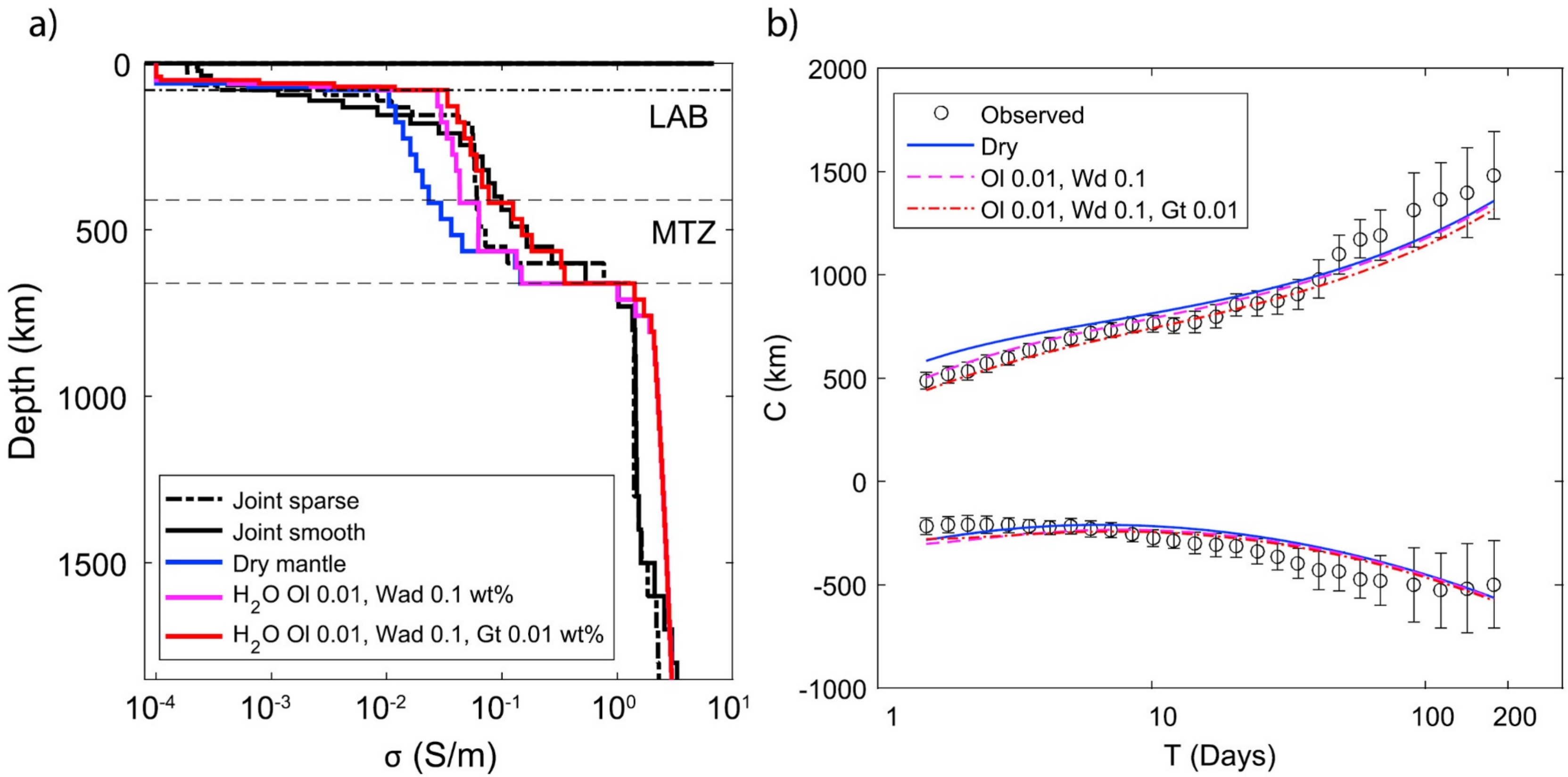

Grayver et al. (2017)

Electrical conductivity modelling: data set

- Data set from the compilation of *Vacher and Verhoeven* (2007) :

Deduced from experiments experimental data on bridgmanite (Shankland et al., 1993; Poirier and Peyronneau, 1992) and magnesio-wüstite (Dobson and Brodholt, 2000)

Parameter	Bridgmanite	Ferro-periclase
$\log(\sigma_0)$	1.28 ± 0.18	2.56 ± 0.10
E_a (eV/K)	0.68 ± 0.04	0.88 ± 0.03
V_a (cm^3/mol)	-0.26 ± 0.03	-0.26 ± 0.07
α	3.56 ± 1.32	3.14 ± 0.07
β	-1.72 ± 0.38	0
x_{ref}	0.1	0.1

$$\sigma_i = \sigma_0^i \left(\frac{x_{Fe}^i}{x_{ref}^i}\right)^{\alpha} \exp\left[-\frac{E_a^i + \beta\left(x_{Fe}^i - x_{ref}^i\right) + PV_a^i}{kT}\right]$$

Influence of temperature and composition

● Data set from the compilation of Vacher and Verhoeven (2007)

● Influence of temperature :

- Electrical conductivity increases with temperature. Opposite trend to thermal effects on density and seismic velocities.

- A 500 K temperature anomaly in the deep mantle results in a 20 to 30 % change in conductivity.

● Influence of global iron content :

- Conductivity increases with global iron fraction (X_{Fe}), whatever the depth.

- A 3% increase of X_{Fe} (typical of enrichment in LLSVPs) induces an increase in conductivity by a factor 3.

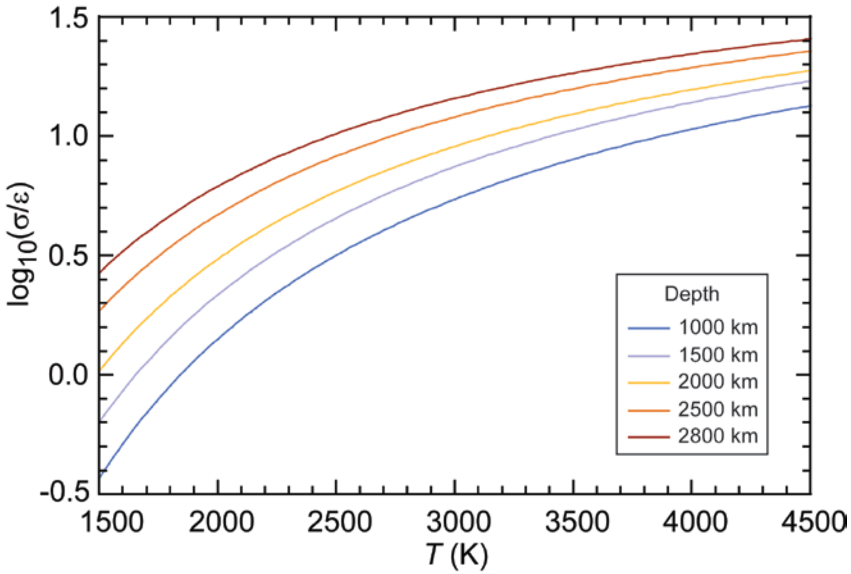

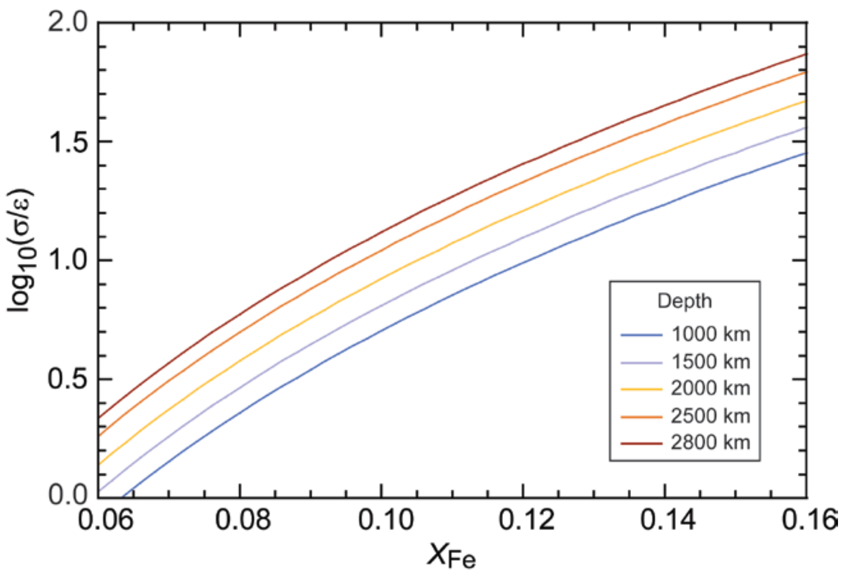

Lower mantle electrical conductivity: radial profiles

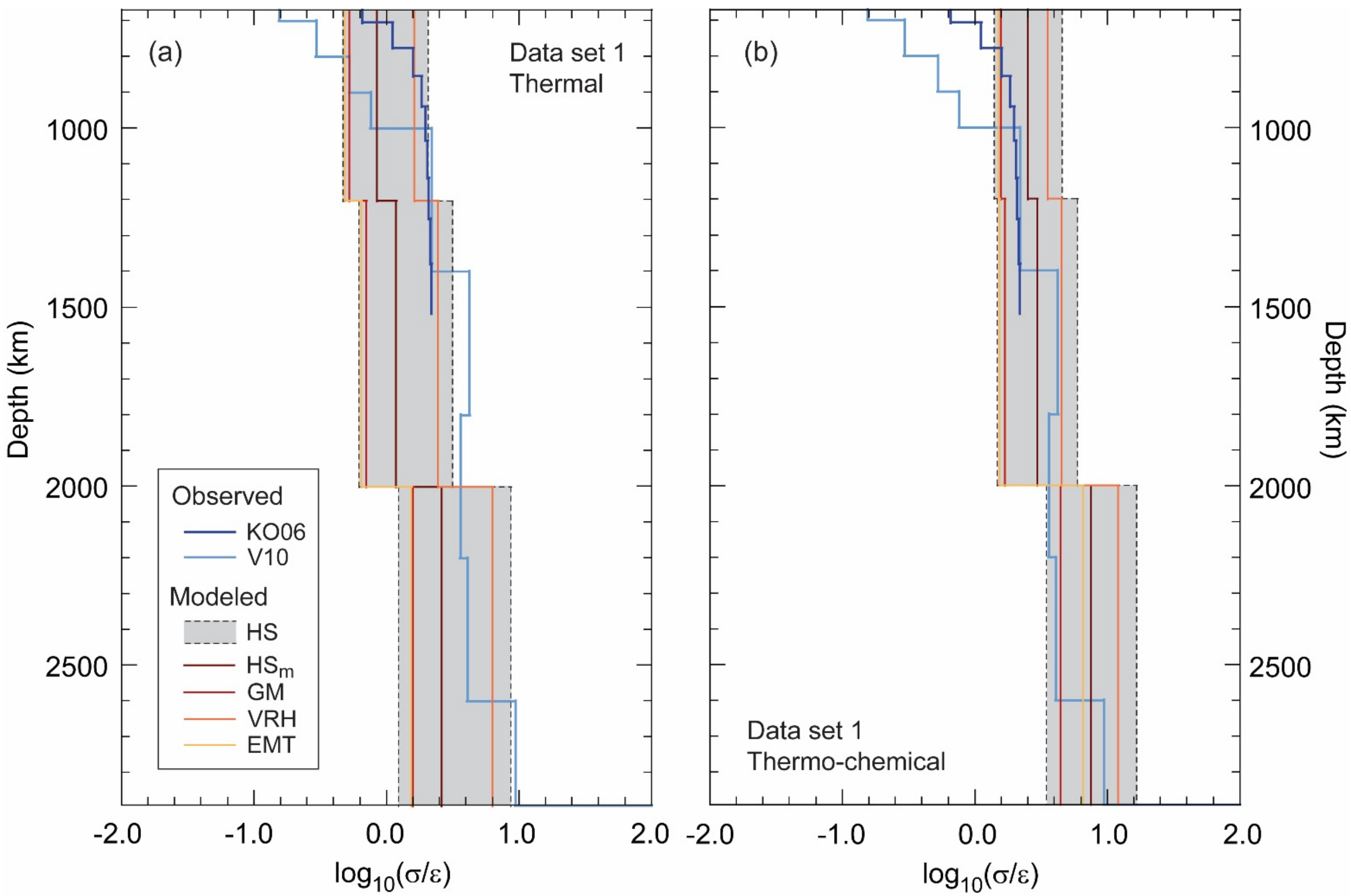

Deschamps & Khan (2016)

- Purely thermal model: conductivity around 1 S/m in the mid mantle, and 3 S/m in the lowermost mantle, smaller than observed model.
- Thermo-chemical model: conductivity around 3 S/m in the mid mantle, and 10 S/m in the lowermost mantle, consistent with available observed 1D radial models (Velímský, 2010).

Electrical conductivity: observed radial models

- Obtained from satellite data (e.g., CHAMP, and more recently SWARM).

- Globally increases with depth.

At lowermost mantle (< 2000 km): from 2.5 S/m (Puethe et al., 2015) to 10 S/m (Velímsky, 2010; Civet et al., 2015).

- Reconstructed profiles for pyrolitic composition (X_{Bm}=0.8; X_{Fe}=0.1) and potential temperature 2000 K agrees well with observed profiles, but large HS bounds.

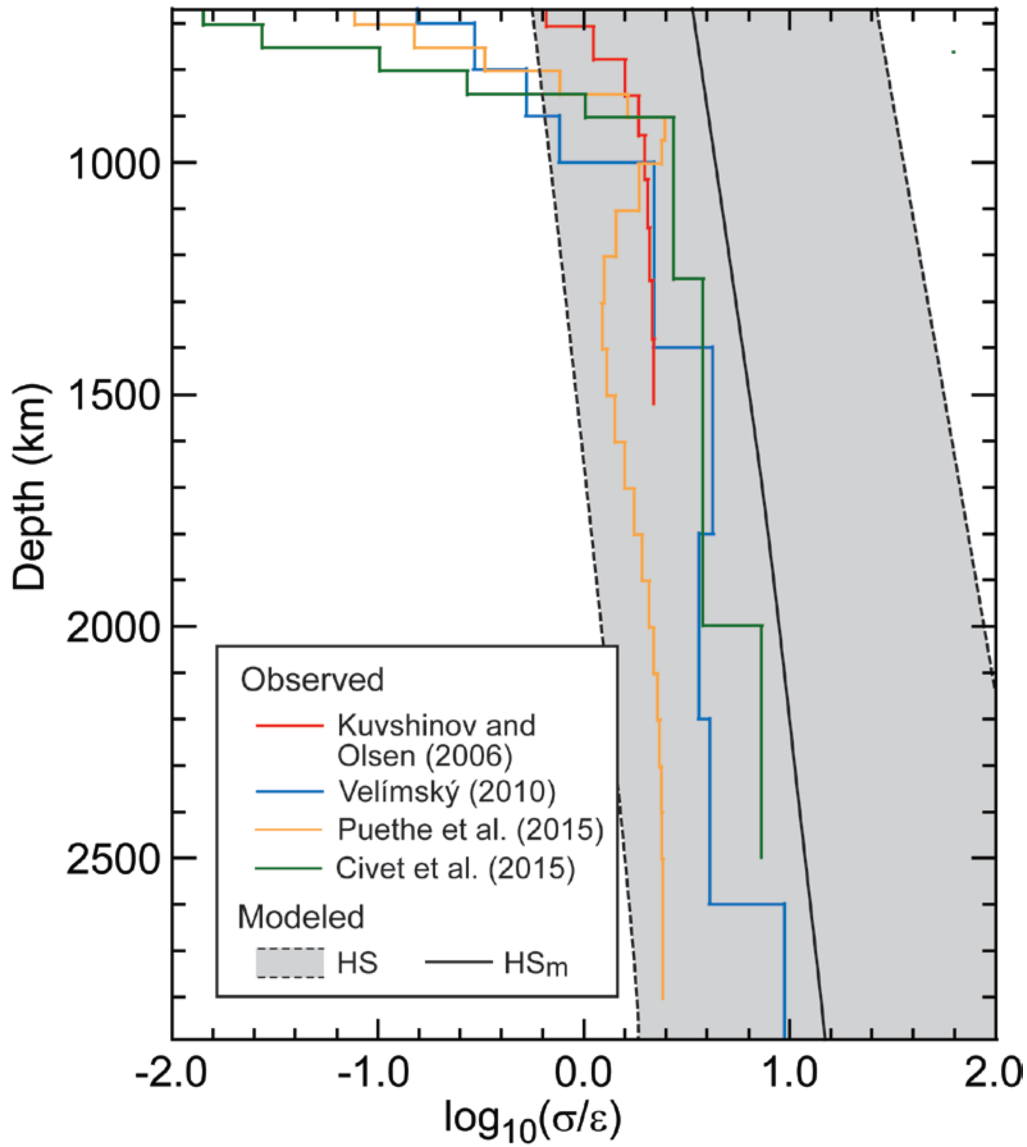

Electrical conductivity tomography

- 3D electrical conductivity maps

Built from long period (few days to months) variations in surface magnetic field recorded at different locations.

- Two global models: Kelbert et al. (2009) (KSE09), and Semenov and Kuvshinov (2012) (SK12)

- Strong discrepancies both in amplitude and pattern, due to differences in methods, data, and corrections (*e.g.*, ocean signal).

- A common feature in transition zone: low conductivity beneath South Europe/North Africa; high conductivity beneath Eastern China.

- Strong anomalies in transition zone: signature of lateral variations in water content? (KSE09).

- Uncorrelated with seismic tomography: compositional effects?

- Maps up to depths of 1600 km. Probing deeper regions requires long periods (> 1 year) variations with high accuracy.

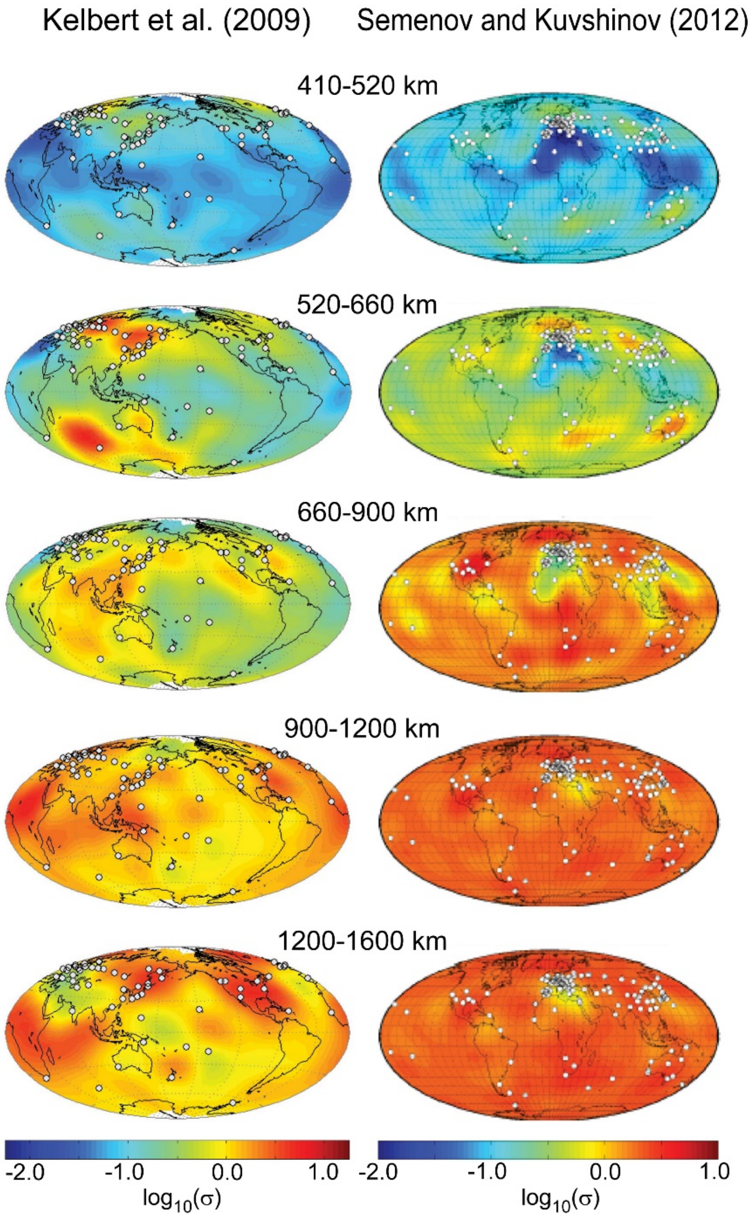

Forward modelling

- Use 3D thermo-chemical model (*e.g*, Trampert et al., 2004) and mineral physics data to reconstruct deep mantle thermal conductivity:

- Purely thermal and thermo-chemical models differ both in amplitude and in pattern.

- Purely thermal models are less conductive and amplitude of anomalies are smaller.

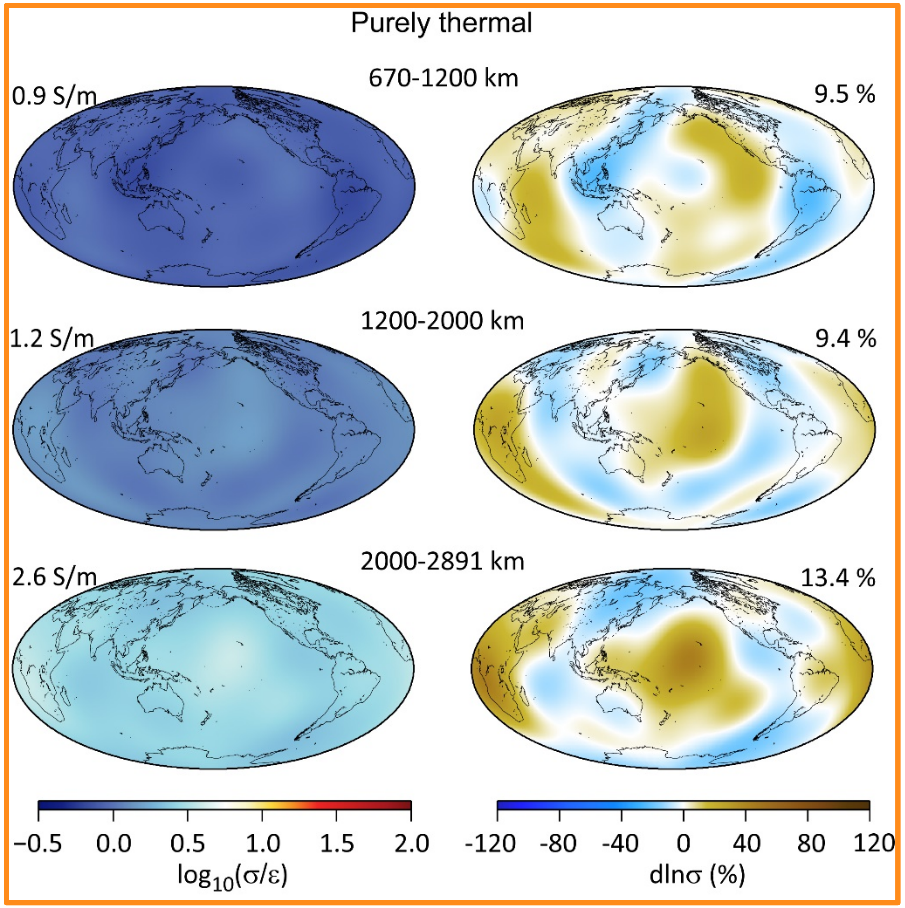

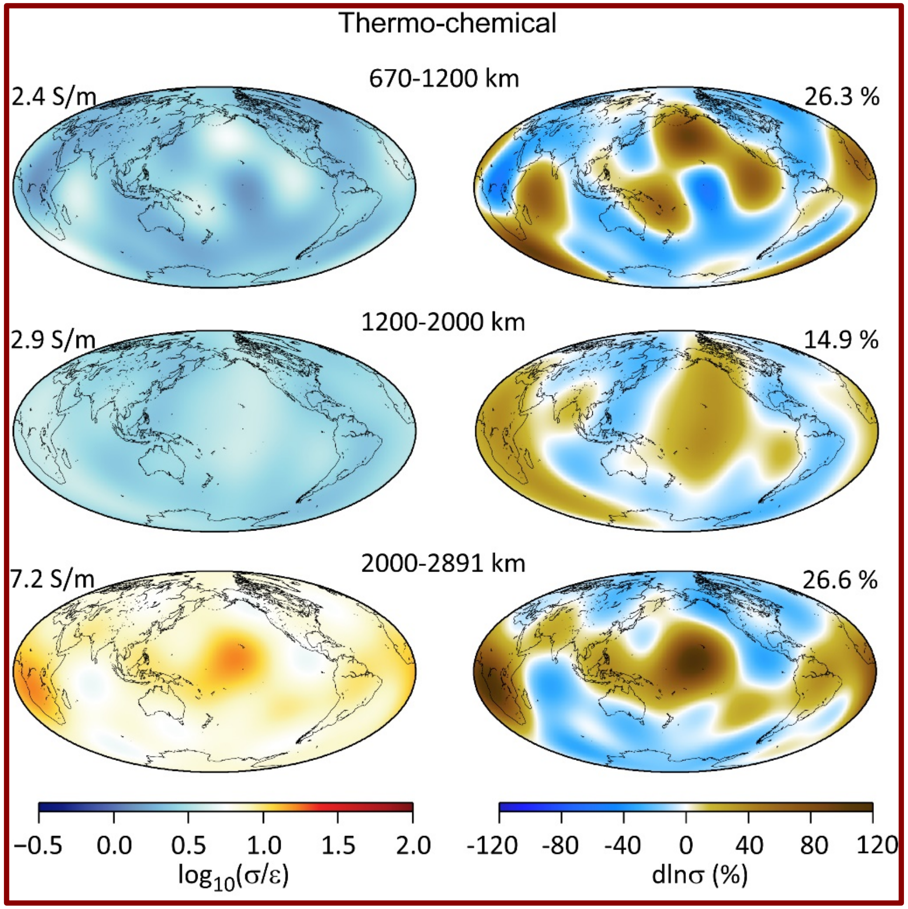

Deschamps & Khan (2016)

Estimator : geometric average of upper and lower HS bounds

C-responses: thermal *vs* thermo-chemical models

- Synthetic C-response (Re and Im parts) from models of electrical conductivity for horizontally averaged (1D) and full 3D models.

- C-response for thermal and thermo-chemical models are clearly different at large period (1 year and more), but cannot be discriminated with current data (symbols on plots).

- C-response for radial and 3D models : very similar for thermal model, but significant 3D-variations for thermo-chemical models.

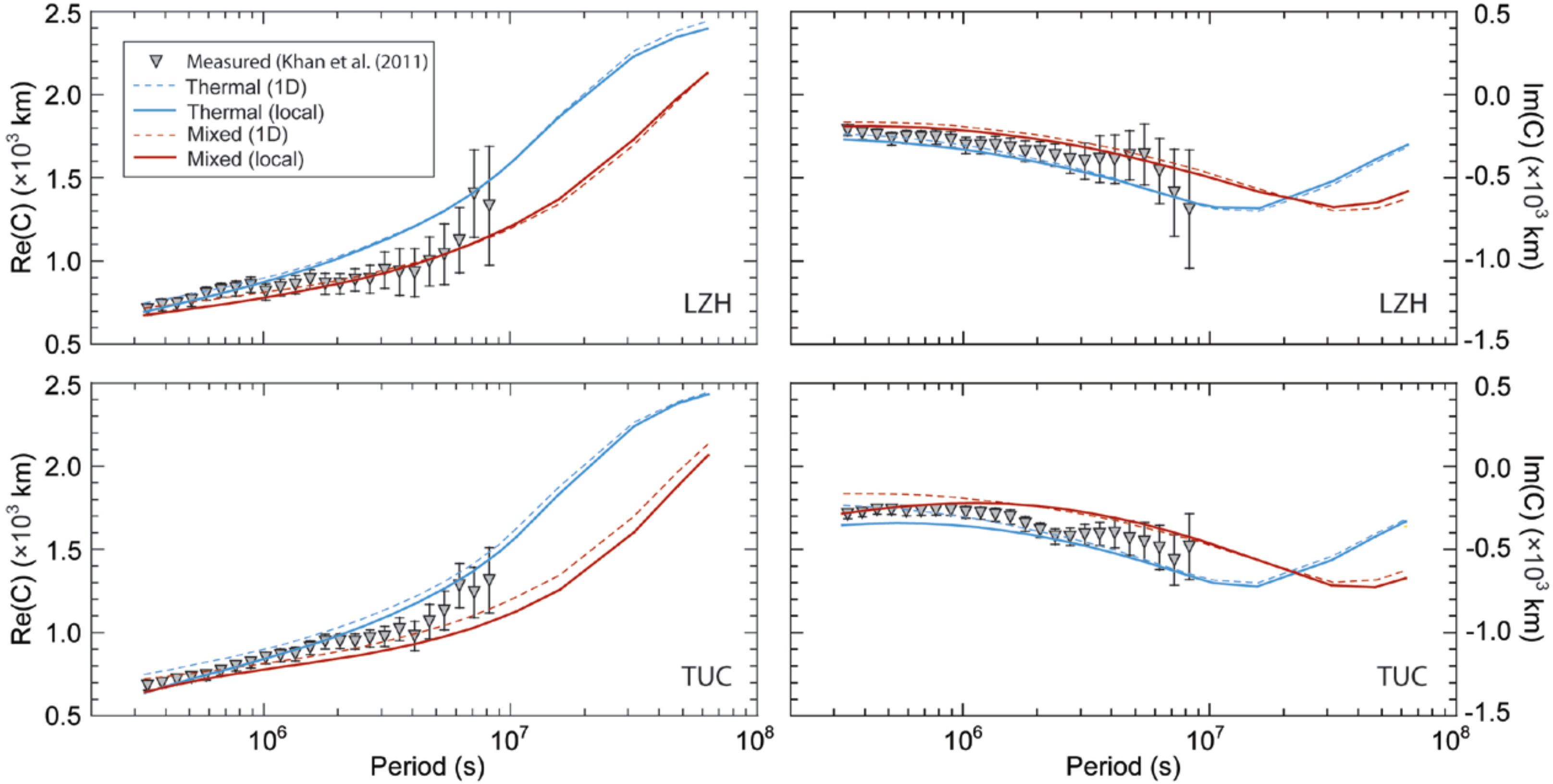

C-responses

- Variations of external (e.g., ionospheric) magnetic field induce electric current within the Earth, and an additional induced magnetic field whose variations add up to those observed at the surface.

  - Induced variations depend on the electric conductivity structure.

  - Mantle response, based on separation between external (source) and internal (induced) magnetic field variations, *e.g.*, C-response (Banks, 1969).

- C-response built from observed vertical and horizontal components of the magnetic field :

$$C(\omega) = -\frac{a \tan\vartheta}{2} \frac{Z(\omega)}{H(\omega)}$$

- Synthetic C-responses, reconstructed from given electrical conductivity 3D-model and input external current (e.g., ring current) by solving Maxwell's equations :

Radial component is more affected than horizontal components by induced current

$$\nabla \times \mathbf{H} = \sigma \mathbf{E} + \mathbf{j}^{\text{ext}}$$

$$\nabla \times \mathbf{E} = i\omega\mu_0 \mathbf{H}$$

C-responses: thermal *vs* thermo-chemical models

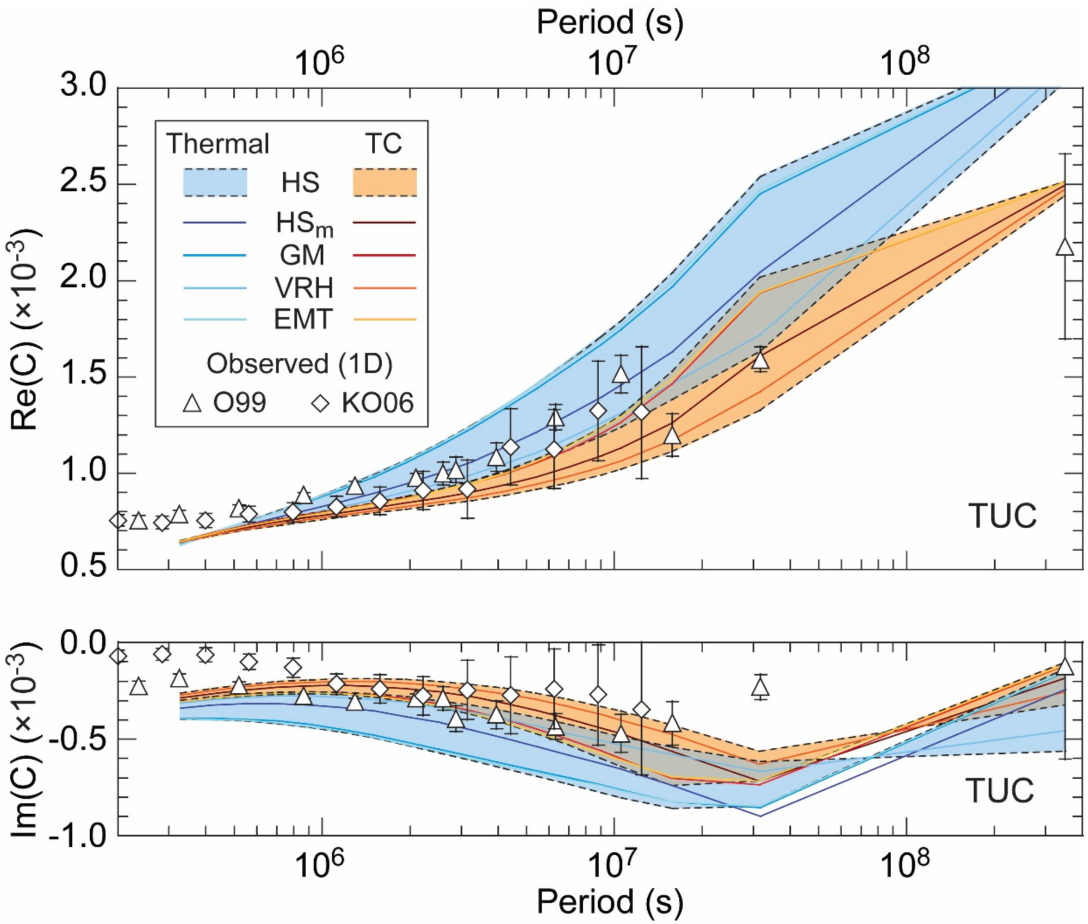

Long period (> 1 year) variations of the magnetic field may discriminate between thermal and thermo-chemical models, and may distinguish 3D thermo-chemical structure.

Global radial models of shear-wave quality factor (Q_μ)

- Measured from free oscillation and surface waves.

- Depth variations: main trends:

- Low attenuation in lithosphere.

- High attenuation in low velocity-zone (100-200 km).

- Q_μ increases in transition zone.

- Q_μ around 250-350 in lower mantle

- Resovsky et al. (2005) (Qtr):

- Surface-wave + spheroidal modes; probabilistic inversion (Neighborhood algorithm).

- Three layer in lower mantle, with more attenuation in lowermost (> 2000 km mantle).

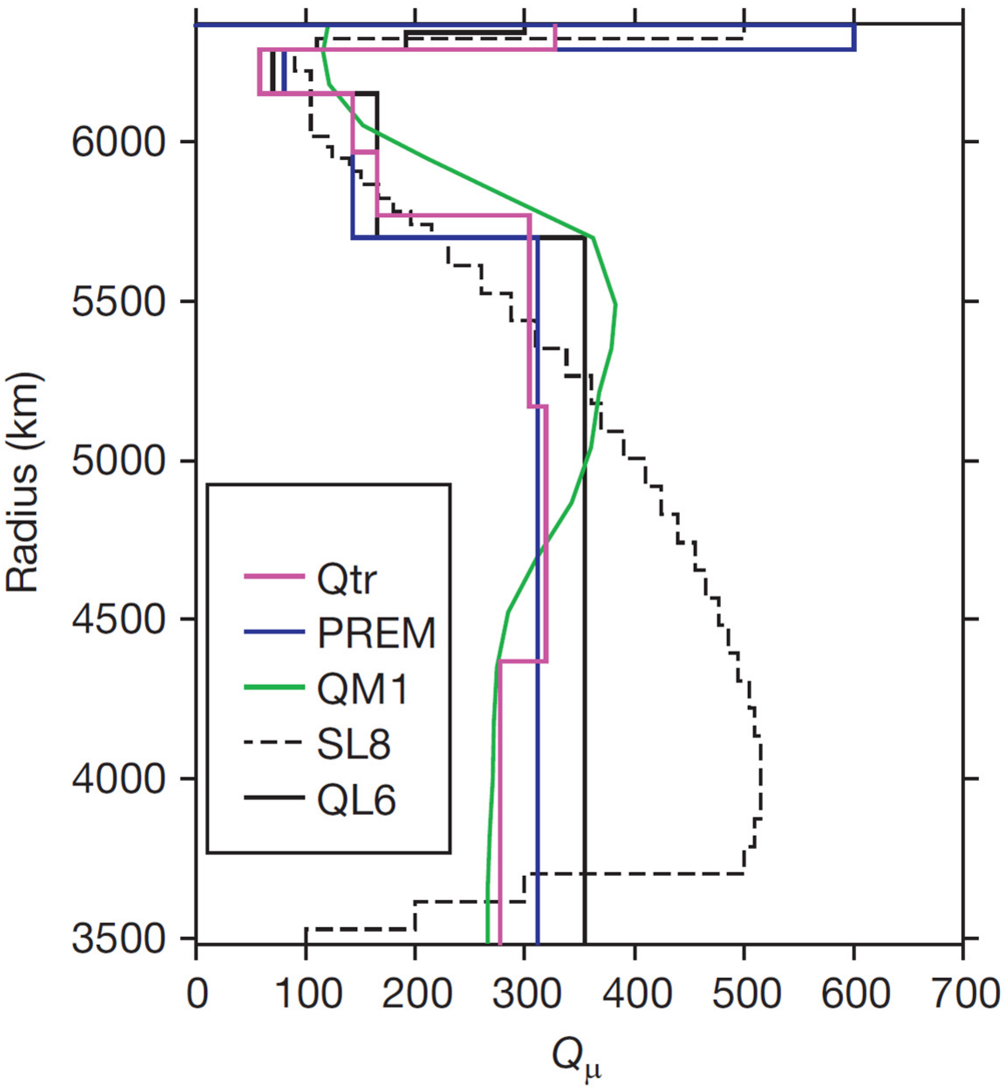

Romanowicz and Mitchell (2015)

Q_μ in LLSVPs

- Konishi et al. (2017): inversion of seismic waveform data for models of *Q* and dlnV_S in Western Pacific (sampling western tip of LLSVP), and Northern Pacific.

- Three distinct profiles. Central profile, sampling Caroline plume, has lower Q_μ and V_S.

- Q_μ and V_S increase from ~ 2500 down to CMB.

- In lowermost layer: Q_μ ~ 215 in central region, and 260 in side regions.

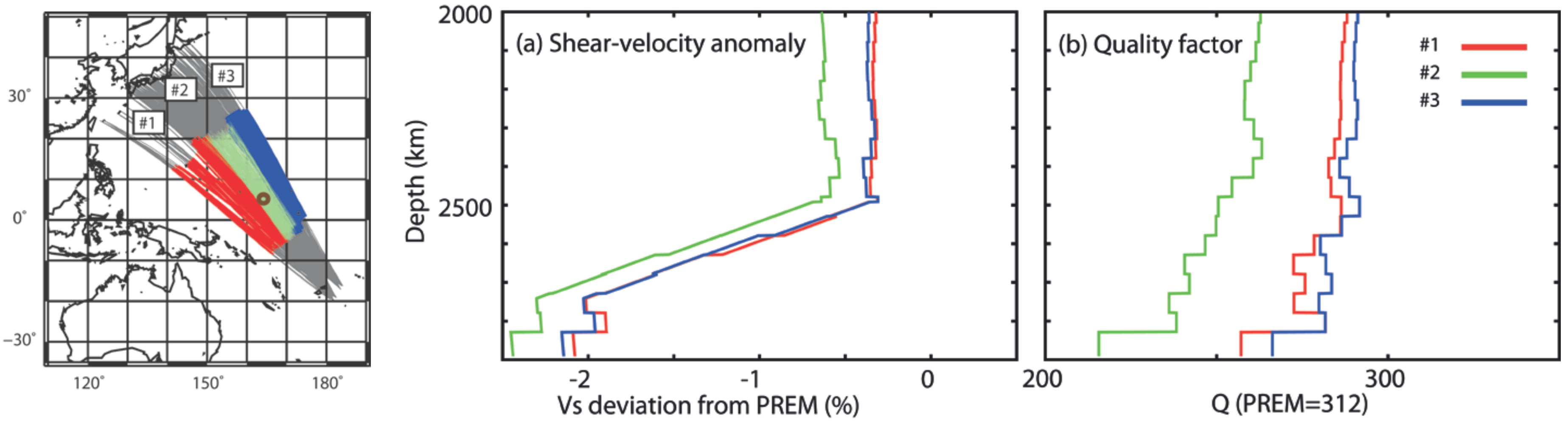

Konishi et al. (2017)

- Liu and Grand (2018): PcS t* measurements beneath African LLSVPs; Q_μ ~ 110.

Q: limitations

- Focussing/defocussing effects: regions with large seismic velocity anomalies (e.g., ULVZs) alter raypaths leading to under- or over estimation of attenuation.

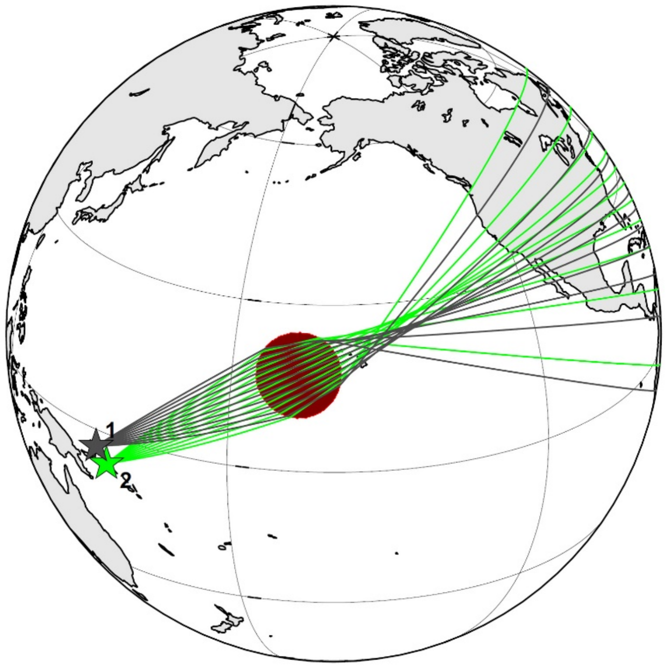

Cottaar and Romanowicz (2012)

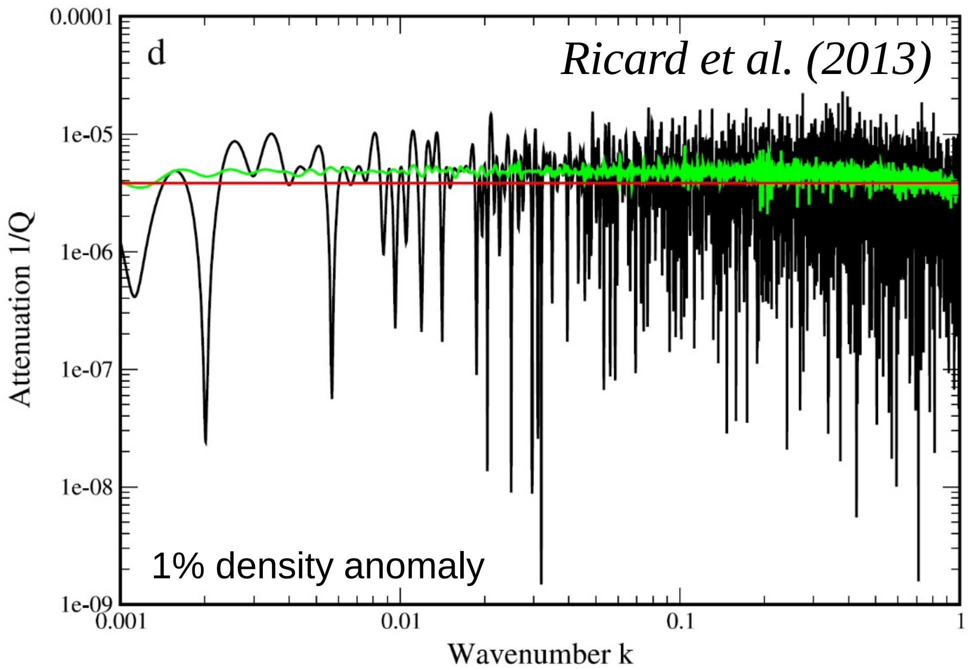

- Small-scale structure may generate attenuation due to scattering of seismic waves.

For layered medium, attenuation depends on wave-number of heterogeneities and density and velocity induced by these heterogeneities (Ricard et al., 2013): added contribution of 6-9% density and velocity anomalies and anisotropy induce energy reduction equivalent to mantle values of Q.

Comparing temperature anomaly from Q_μ and V_S

- Konishi et al. (2017): calculates dT independently from variations in V_S (dT_{VS}, horizontal bands) and in Q_μ (dT_Q, curves).

- At 2850 km: differences between three profiles denote temperature changes ~ 100 K within the Pacific LLSVP.

- At z < 2500 km : purely thermal anomalies imply low activation volume (H). Differences between central and side profiles denote a temperature change ~ 60 K between centre and edges of Caroline plume, and possibly entrainment of dense LLSVP material.

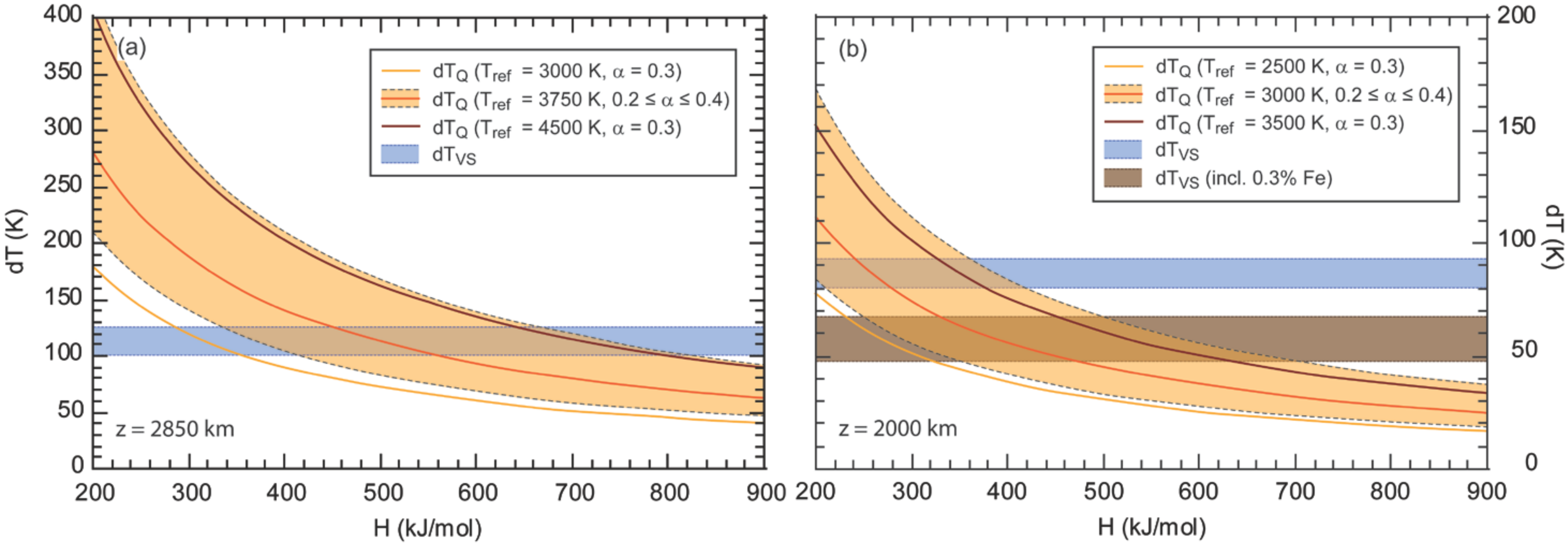

Konishi et al. (2017)